

Industrial

Electronics

Biomedical

Civil

Aerospace

Computer

Electrical

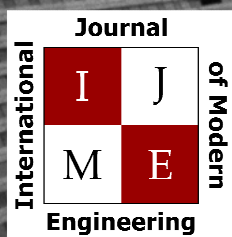
Chemical

Mechanical



ENGINEERING





[www.ijme.us](http://www.ijme.us)

Print ISSN: 2157-8052  
Online ISSN: 1930-6628



[www.iajc.org](http://www.iajc.org)

## INTERNATIONAL JOURNAL OF MODERN ENGINEERING

### ABOUT IJME:

- IJME was established in 2000 and is the first and official flagship journal of the International Association of Journal and Conferences (IAJC).
- IJME is a high-quality, independent journal steered by a distinguished board of directors and supported by an international review board representing many well-known universities, colleges and corporations in the U.S. and abroad.
- IJME has an impact factor of **3.00**, placing it among the top 100 engineering journals worldwide, and is the #1 visited engineering journal website (according to the National Science Digital Library).

### OTHER IAJC JOURNALS:

- The International Journal of Engineering Research and Innovation (IJERI)  
For more information visit [www.ijeri.org](http://www.ijeri.org)
- The Technology Interface International Journal (TIIJ).  
For more information visit [www.tiij.org](http://www.tiij.org)

### IJME SUBMISSIONS:

- Manuscripts should be sent electronically to the manuscript editor, Dr. Philip Weinsier, at [philipw@bgsu.edu](mailto:philipw@bgsu.edu).

For submission guidelines visit  
[www.ijme.us/submissions](http://www.ijme.us/submissions)

### TO JOIN THE REVIEW BOARD:

- Contact the chair of the International Review Board, Dr. Philip Weinsier, at [philipw@bgsu.edu](mailto:philipw@bgsu.edu).

For more information visit  
[www.ijme.us/ijme\\_editorial.htm](http://www.ijme.us/ijme_editorial.htm)

### INDEXING ORGANIZATIONS:

- IJME is currently indexed by 22 agencies.  
For a complete listing, please visit us at [www.ijme.us](http://www.ijme.us).

### Contact us:

**Mark Rajai, Ph.D.**

Editor-in-Chief  
California State University-Northridge  
College of Engineering and Computer Science  
Room: JD 4510  
Northridge, CA 91330  
Office: (818) 677-5003  
Email: [mrajai@csun.edu](mailto:mrajai@csun.edu)



[www.tiij.org](http://www.tiij.org)



[www.ijeri.org](http://www.ijeri.org)

---

# INTERNATIONAL JOURNAL OF MODERN ENGINEERING

The INTERNATIONAL JOURNAL OF MODERN ENGINEERING (IJME) is an independent, not-for-profit publication, which aims to provide the engineering community with a resource and forum for scholarly expression and reflection.

IJME is published twice annually (fall and spring issues) and includes peer-reviewed articles, book and software reviews, editorials, and commentary that contribute to our understanding of the issues, problems, and research associated with engineering and related fields. The journal encourages the submission of manuscripts from private, public, and academic sectors. The views expressed are those of the authors and do not necessarily reflect the opinions of the IJME editors.

## EDITORIAL OFFICE:

Mark Rajai, Ph.D.  
Editor-in-Chief  
Office: (818) 677-2167  
Email: [ijmeeditor@iajc.org](mailto:ijmeeditor@iajc.org)  
Dept. of Manufacturing Systems  
Engineering & Management  
California State University-  
Northridge  
18111 Nordhoff Street  
Northridge, CA 91330-8332

## THE INTERNATIONAL JOURNAL OF MODERN ENGINEERING EDITORS

### *Editor-in-Chief:*

**Mark Rajai**

California State University-Northridge

### *Associate Editor:*

**Li Tan**

Purdue University North Central

### *Production Editor:*

**Philip Weinsier**

Bowling Green State University-Firelands

### *Subscription Editor:*

**Morteza Sadat-Hossieny**

Northern Kentucky University

### *Executive Editor:*

**Paul Wilder**

Vincennes University

### *Publisher:*

**Bowling Green State University-Firelands**

### *Manuscript Editor:*

**Philip Weinsier**

Bowling Green State University-Firelands

### *Copy Editor:*

**Li Tan**

Purdue University North Central

### *Technical Editors:*

**Michelle Brodke**

Bowling Green State University-Firelands

**Paul Akangah**

North Carolina A&T State University

**Marilyn Dyrud**

Oregon Institute of Technology

### *Web Administrator:*

**Saeed Namyar**

Advanced Information Systems

---

# TABLE OF CONTENTS

<i>Editor's Note: A Look Ahead to the 2018 IAJC Conference in Orlando, Florida</i> .....	3
Philip Weinsier, IJME Manuscript Editor	
<i>IoT Instrument for Heart Monitoring: Interfacing Humans and Robots</i> .....	5
Antonio Morales, University of Hartford; Hassan S. Salehi, California State University; Kiwon Sohn, University of Hartford	
<i>Design and Implementation of an Alternative, Low-Cost Water Chlorination System in El Cercado, Dominican Republic</i> .....	13
Truc T. Ngo, University of San Diego; Jeremiah Medina, University of San Diego; David White, University of San Diego; Danford Jooste, University of San Diego; Karly Jerman, University of San Diego; Jeremy Hagen, University of San Diego; Joanne Peterson, El Cercado, San Juan, Dominican Republic	
<i>Implementation of a Ball-and-Beam Control System Using PD Bode Design</i> .....	21
Jordan K. Ford, United States Coast Guard Academy; Tooran Emami, United States Coast Guard Academy	
<i>Optimization of the Quick and Automatic Segmentation of Medical Images by Using a Fuzzy Combined Method</i> .....	28
Shahin Karimi	
<i>Hydration and Setting Behavior of Cement Pastes Modified with Swine-Waste Biochar</i> .....	33
Andrea Nana Ofori-Boadu, North Carolina Agricultural and Technical State University; Frederick Aryeetey, North Carolina Agricultural and Technical State University; Zerihun Assefa, North Carolina Agricultural and Technical State University; Elham Fini, North Carolina Agricultural and Technical State University	
<i>Design and Fabrication of a Samarium Selective Potentiometric Sensor Using Kryptofix 22DD in a Polymer Matrix Membrane</i> .....	44
Neshat Majd, Islamic Azad University, Iran; Arezoo Ghaemi, Ferdowsi University of Mashhad, Iran	
<i>Instructions for Authors: Manuscript Submission Guidelines and Requirements</i> .....	52





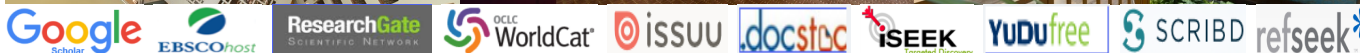
# 6<sup>TH</sup> IAJC INTERNATIONAL CONFERENCE

COMING FALL, 2018 – ORLANDO, FLORIDA

The leading indexed high-impact-factor conference on engineering and related technologies.



## Our Hotel—Embassy Suites



## Editorial Review Board Members

Mohammed Abdallah	State University of New York (NY)	Gengchen Liu	University of California-Davis (CA)
Nasser Alaraje	Michigan Tech (MI)	Guoxiang Liu	University of North Dakota (ND)
Ammar Al-Farga	University of Jiangnan (CHINA)	Louis Liu	University of New Orleans (LA)
Aly Mousaad Aly	Louisiana State University (LA)	Peng Liu	Washington State University (WA)
Paul Akangah	North Carolina A&T State University (NC)	Mani Manivannan	ARUP Corporation
Lawal Anka	Zamfara AC Development (NIGERIA)	G.H. Massiha	University of Louisiana (LA)
Jahangir Ansari	Virginia State University (VA)	Jim Mayrose	Buffalo State College (NY)
Kevin Berisso	Ohio University (OH)	Thomas McDonald	University of Southern Indiana (IN)
Pankaj Bhambri	Guru Nanak Dev Engineering (INDIA)	David Melton	Eastern Illinois University (IL)
Water Buchanan	Texas A&M University (TX)	Shokoufeh Mirzaei	Cal State Poly Pomona (CA)
John Burningham	Clayton State University (GA)	Bashir Morshed	University of Memphis (TN)
Shaobiao Cai	Penn State University (PA)	Sam Mryyan	Excelsior College (NY)
Vigyana Chandra	Eastern Kentucky University (KY)	Jessica Murphy	Jackson State University (MS)
Isaac Chang	Illinois State University (IL)	Wilson Naik	University of Hyderabad (INDIA)
Shu-Hui (Susan) Chang	Iowa State University (IA)	Arun Nambiar	California State University Fresno (CA)
Bin Chen	Purdue University Northwest (IN)	Ramesh Narang	Indiana University-Purdue University (IN)
Wei-Yin Chen	University of Mississippi (MS)	Anand Nayyar	Institute Management and Tech (INDIA)
Rigoberto Chinchilla	Eastern Illinois University (IL)	Aurenice Oliveira	Michigan Tech (MI)
Phil Cochrane	Indiana State University (IN)	Reynaldo Pablo	Indiana University-Purdue University (IN)
Emily Crawford	Southern Wesleyan University (SC)	Basile Panoutsopoulos	Community College of Rhode Island (RI)
Brad Deken	Southeast Missouri State University (MO)	Shahera Patel	Sardar Patel University (INDIA)
Z.T. Deng	Alabama A&M University (AL)	Jose Pena	Purdue University Calumet (IN)
Sagar Deshpande	Ferris State University (MI)	Karl Perusich	Purdue University (IN)
David Domermuth	Appalachian State University (NC)	Thongchai Phairoh	Virginia State University (VA)
Dongliang Duan	University of Wyoming (WY)	Huyu Qu	Honeywell Corporation
Marilyn Dyrud	Oregon Institute of Technology (OR)	John Rajadas	Arizona State University (AZ)
Mehran Elahi	Elizabeth City State University (NC)	Vijaya Ramnath	Sri Sairam Engineering College (CHENNAI)
Ahmed Elsayy	Tennessee Technological University (TN)	Desire Rasolomampionona	Warsaw University of Tech (POLAND)
Rasoul Esfahani	DeVry University (OH)	Mohammad Razani	New York City College of Tech (NY)
Dominick Fazarro	Sam Houston State University (TX)	Sangram Redkar	Arizona State University-Poly (AZ)
Ignatius Fomunung	University of Tennessee Chattanooga (TN)	Michael Reynolds	University of Arkansas Fort Smith (AR)
Ahmed Gawad	Zagazig University EGYPT	Nina Robson	California State University-Fullerton (CA)
Daba Gedafa	University of North Dakota (ND)	Marla Rogers	Wireless Systems Engineer
Mohsen Hamidi	Utah Valley University (UT)	Dale Rowe	Brigham Young University (UT)
Mamoon Hammad	Abu Dhabi University (UAE)	Karen Ruggles	DeSales University (PA)
Gene Harding	Purdue Polytechnic (IN)	Anca Sala	Baker College (MI)
Youcef Himri	Safety Engineer in Sonelgaz (ALGERIA)	Alex Sergeev	Michigan Technological University (MI)
Xiaobing Hou	Central Connecticut State University (CT)	Hiral Shah	St. Cloud State University (MN)
Shelton Houston	University of Louisiana Lafayette (LA)	Siles Singh	St. Joseph University Tanzania (AFRICA)
Kun Hua	Lawrence Technological University (MI)	Ahmad Sleiti	University of North Carolina Charlotte (NC)
Ying Huang	North Dakota State University (ND)	Jiahui Song	Wentworth Institute of Technology (MA)
Dave Hunter	Western Illinois University (IL)	Yuyang Song	Toyota Corporation
Christian Hyeng	North Carolina A&T University (NC)	Carl Spezia	Southern Illinois University (IL)
Pete Hylton	Indiana University Purdue (IN)	Michelle Surerus	Ohio University (OH)
Ghassan Ibrahim	Bloomsburg University (PA)	Jalal Taheri	Bostan Abad Islamic Azad University (IRAN)
John Irwin	Michigan Tech (MI)	Li Tan	Purdue University Northwest (IN)
Toqeer Israr	Eastern Illinois University (IL)	Harold Terano	Camarines Sur Polytechnic (NABUA)
Sudershan Jetley	Bowling Green State University (OH)	Sanjay Tewari	Louisiana Tech University (LA)
Rex Kanu	Ball State University (IN)	Vassilios Tzouanas	University of Houston Downtown (TX)
Tolga Kaya	Central Michigan University (MI)	Jeff Ulmer	University of Central Missouri (MO)
Satish Ketkar	Wayne State University (MI)	Mihaela Vorvoreanu	Purdue University (IN)
Manish Kewalramani	Abu Dhabi University (UAE)	Phillip Waldrop	Georgia Southern University (GA)
Tae-Hoon Kim	Purdue University Northwest (IN)	Abraham Walton	Purdue University (IN)
Chris Kluse	Bowling Green State University (OH)	Haoyu Wang	Central Connecticut State University (CT)
Doug Koch	Southeast Missouri State University (MO)	Liangmo Wang	Nanjing University of Science/Tech (CHINA)
Ognjen Kuljaca	Brodarski Institute (CROATIA)	Boonsap Witchayangkoon	Thammasat University (THAILAND)
Chakresh Kumar	Uttar Pradesh Tech University (INDIA)	Alex Wong	Digilent Inc.
Zaki Kuruppallil	Ohio University (OH)	Shuju Wu	Central Connecticut State University (CT)
Edward Land	Johns Hopkins Medical Institute	Baijian "Justin" Yang	Ball State University (IN)
Jane LeClair	Excelsior College (NY)	Eunice Yang	University of Pittsburgh Johnstown (PA)
Shiyong Lee	Penn State University Berks (PA)	Mijia Yang	North Dakota State University (ND)
Soo-Yen Lee	Central Michigan University (MI)	Xiaoli (Lucy) Yang	Purdue University Northwest (IN)
Solomon Leung	Idaho State University (ID)	Faruk Yildiz	Sam Houston State University (TX)
Chao Li	Florida A&M University (FL)	Yuqui You	Morehead State University (KY)
Jimmy Linn	Eastern Carolina University (NC)	Pao-Chiang Yuan	Jackson State University (MS)
Dale Litwhiler	Penn State University (PA)	Jinwen Zhu	Missouri Western State University (MO)

# IoT INSTRUMENT FOR HEART MONITORING: INTERFACING HUMANS AND ROBOTS

---

Antonio Morales, University of Hartford; Hassan S. Salehi, California State University; Kiwon Sohn, University of Hartford

## Abstract

The pre-screening process during a doctor's visit is the cornerstone of medical appointments in which body temperature, heartbeat, respiration, and blood pressure are always checked. In this study, the authors developed a novel system that combines custom-made acoustic sensors, IoT devices, and a robotic system to perform heartbeat monitoring automatically. In the hardware design part of this system, an electronic stethoscope was designed, implemented, and tested. This piece of hardware allowed the analog signals of a heartbeat to be digitized for robotic and networking uses. The stethoscope was designed for easy use by both robots and humans. The robot used in this study was the Baxter (Rethink Robotics). Baxter, as well as many other robotic arms or humanoid robots, has an end gripper or "hands." This, the device should also be able to be used by other generic robot arms or humanoid robots. The prototype web server was implemented on a Raspberry Pi 3. The software portion of this system contained implementation of database design, hardware coding, and network coding. The database employed the standard structured query language (SQL) with a specialized subsystem called PostgreSQL. The hardware coding was done using C++ on the particle photon micro-controller. The network coding used one of the industry standard web programming languages, JavaScript. More specifically, node.js was utilized for transferring data from one source to another over Wi-Fi. This would allow a web interface to display a patient's heart data on a web page.

## Introduction

Taking a person's vitals during a doctor's visit in which body temperature, pulse rate, respiration (breathing rate), and blood pressure are always checked. Hospitals see hundreds of people a day, and humans can only act so fast when taking vitals, given the amount of staff support. The development of a method to record human vitals (mainly the human heartbeat) with the help of robotics and the Internet of Things (IoT) could help solve this problem. The design objective of this research study was to allow a humanoid robot to take the vitals of a patient/volunteer instead of a doctor or nurse. Since humanoid robots are quite useful for many general tasks, if the vital recording tool is a good enough fit, the robot should be able to use this tool just like a human would. However, in some circumstances for this to be possi-

ble, some custom hardware and network coding must be implemented.

## Related Works

Robots are starting to become more frequent as technology evolves; and as they become ubiquitous so, too, does the overall price drop. Multiple companies and universities have been trying to create robots to solve specific problems. Since the medical industry is one of the largest industries out there, there have been quite a few attempts to create robots to solve these in hospitals. Most of these problems are caused by humans having to perform menial tasks that divert their attention away from the patients. The company Diligent Robotics is trying to alleviate this problem with the help of mobile robots. Over the past year, Diligent Robotics has been testing their robot, named Poli, in several hospitals in Austin, Texas, where it is learning how to help nurses with simple fetching tasks [1]. Since hospitals are virtually always active with patients, this could help both the doctors and nurses save time, which could be used for seeing more patients.

Another task that is being tackled with the help of robots is drawing blood. The company Veebot has created a robot that accurately takes a patient's blood [2]. It can do this very accurately and quickly using image processing. The process starts when the patient inserts his/her arm into a sleeve-like hole. The device then restricts blood flow to make the veins easier to see. This is quite a novel solution for hospitals, since blood is taken hundreds of times a day. And, if the process works to find a vein, it could also be used for IVs, also considered a menial task. Another problem is stress, which can take place in and out of hospitals. The company behind PARO has created an animatronic robot to help combat this. The robot is modeled after a baby harp seal [3]. The robot is designed with an AI to move and make sounds when someone interacts with it. The AI tends to learn what personality the user likes the best and adapts to it. Many users just cannot seem to resist this robot's charm, which seems to do an excellent job of calming down patients, which, compared to medical sedation, is an amazing humane advancement.

The Internet of Things (IoT) technology has been utilized in health monitoring such as a smart interior environmental analyzer that links the particle firmware to the iOS applica-

tion with Amazon Web Services (AWS) [4]. In this current research project, the authors utilized IoT technology for monitoring the human heartbeat. The prototype web server was implemented on a Raspberry Pi 3, and the network coding used one of the industry standard web programming languages, JavaScript, for transferring data from one source to another over Wi-Fi.

## Problem Statement

The overall goal of this project is to be able to take patients' heartbeats. Each person that goes to a hospital usually has to have this done and it can take a good amount of time, depending on the situation of the facility. So the idea is that this project could help take some of the weight off of hospitals by eliminating this menial task. Hundreds of people go the doctor every day, and virtually all of them need a pre-screening before they can see their physician. The pre-screening process involves taking multiple types of human vitals: heartbeat, blood pressure, temperature, etc. If a hospital is under-staffed then this process can take much longer than expected; time that the patient will spend waiting, which is time that could be better used for both the patient and the hospital staff. Another problem is how all of the data are shared. While yes, most of the data go into a database, the process still usually involves a human. This is a menial task that could be done by implementing an IoT network.

The heartbeat produces a sound, and this sound can be broken up into multiple specific frequencies, and a Fourier transform can be applied to find these frequencies [5, 6]. Once found, a system could be designed to zero in on these frequencies. Such a system would take in the analog signal, isolate the wanted frequencies, and then digitize them for later use. With the heartbeat signal in a digital format, it can now be sent over the web, which also allows it be stored for later use, displayed on-screen for on-demand viewing, and sent to a robot. With this process now being automated, a couple of menial tasks are eliminated; for example, entering data into the database and the simple pre-screening process. In such a scenario, the staff can have more time to interact with the patients. And now with an IoT network, the entire hospital would be more connected and have easier viewing of a specific patient's vitals [7].

## Methodology

Figure 1 show the structure of this project in the form of a flowchart. This chart can be broken up into three main features: the heartbeat sensor, the website, and implementation of a robot.

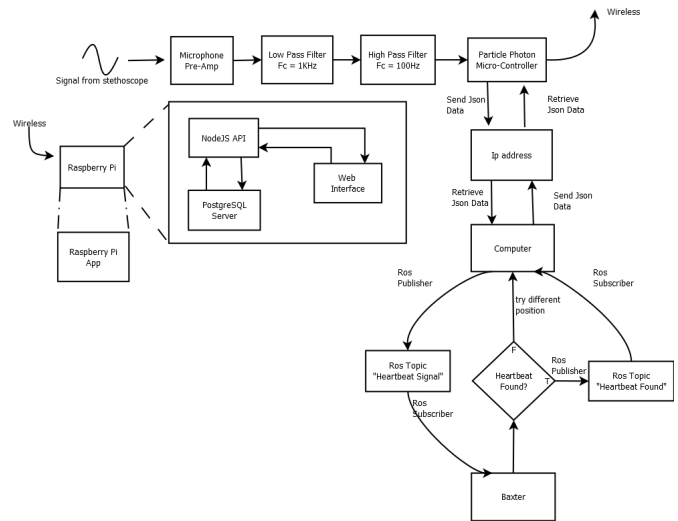


Figure 1. System Flowchart

## Heartbeat Sensor

In order to retrieve heartbeat data that can be sent over the web, a custom sensor was designed. The sensor uses a microphone pre-amplifier, bandpass filter, and Wi-Fi-compatible micro-controller.

## Microphone Pre-Amplifier

The human heartbeat is an analog signal, which must be digitized with a transducer. The choice to use a microphone as the transducer is heavily based on the principle of how stethoscopes work. A stethoscope is a very sensitive pressure sensor made of several components. The most important being the bell diaphragm, which, when pressure is applied, transfers air through the tube to the ear pieces [8]. Since the bell is outputting air, this allows the signal to be picked up by a microphone. The type of microphone chosen for this project was an electret microphone, due to its accuracy in "hearing" the heart. This microphone needed to be inserted into the stethoscope tube at the closest possible position next to the exit hole of the bell diaphragm, as well as be very sensitive, since there would be very little air coming out of the bell. Electret microphones fit both of these criteria, and the one used had a diameter of 6 mm and a sensitivity of -44 dB.

The signal output from this microphone is very small and, thus, needs to be amplified. The amplifier designed for this study was calculated to 68 db. Since electret microphones have an internal JFET, the circuit design must consider how to properly bias this JFET, because without this the signal output would be null. Figure 2 shows the base circuit diagram for an electret microphone amplifier [9].



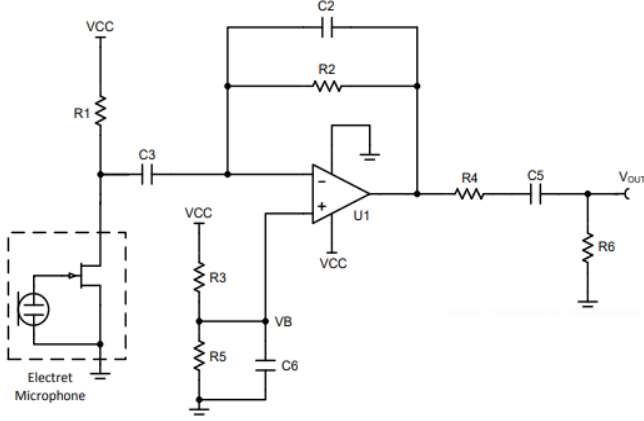


**Figure 2. Pre-Amp Circuit**

Choosing the components for the above circuit was the most important part and needed to be calculated for the exact microphone specs (see Table 1).

**Table 1. Electret Microphone Specs**

Sensitivity	-44 ±3 dB
V <sub>s</sub>	2V
I <sub>max</sub>	500 nA
Z	2.2 KΩ
S/N	60 dB

To start this calculation and find out how many millivolts would be generated per pascal of pressure, Equation (1) was used:

$$\frac{mV}{Pa} = \frac{10^{\frac{sensdB}{20}}}{20} \quad (1)$$

Next, the current generated by the pressure was calculated using Equation (2):

$$\frac{\mu A}{Pa} = \frac{mV / Pa}{Z} \quad (2)$$

The maximum current generated by the pressure was calculated using Equation (3):

$$\mu A = \frac{\mu A}{Pa} \cdot 2 \quad (3)$$

The value of resistor R2 can be found using Equation (4)—the maximum current. The authors used 1.228V for 100 dB, or the maximum pressure expected.

$$R2 = \frac{1.228V}{U_{max}} \quad (4)$$

Assuming  $f$  equals 133 KHz, as the desired pole for the filter, the value of C2 can now be found using Equation (5). This is a feedback resistor that will keep the system stable from the parasitic capacitance of the op-amp.

$$C2 = \frac{1}{2\pi \cdot f \cdot R2} \quad (5)$$

R1 can be found by using node analysis from Equation (6), where  $V_{mic}$  is the required voltage that the JFET needs to be biased, and  $I_s$  the required current.

$$R1 = \frac{V_{cc} - V_{mic}}{I_s} \quad (6)$$

C3 can be found using the same method as finding C2 [see Equation (5)], but substituting R2 for R1, and  $f$  for the chosen corner frequency [see Equation (7)]:

$$C3 = \frac{1}{2\pi \cdot f \cdot R1} \quad (7)$$

Applying the same steps to the other components yields similar results and helps to choose the correct values. Once this has been done, the circuit should have a properly biased electret microphone feeding a signal into an op-amp, which is then amplified to a useful level. However, since this microphone is picking up all of the noise and then amplifying it, the resultant output is going to be quite noisy. Thus, filtering must be added.

## Band-Pass Filter

The filter design is a second-order Butterworth with a quality factor of 0.85. The specific type is a multiple-feedback low-pass filter cascaded with a multiple-feedback high-pass filter. This is done in order to create a flat plateau in the frequency response from 100 Hz to 1 KHz. Figure 3 shows a picture of this bandpass filter using PSpice.

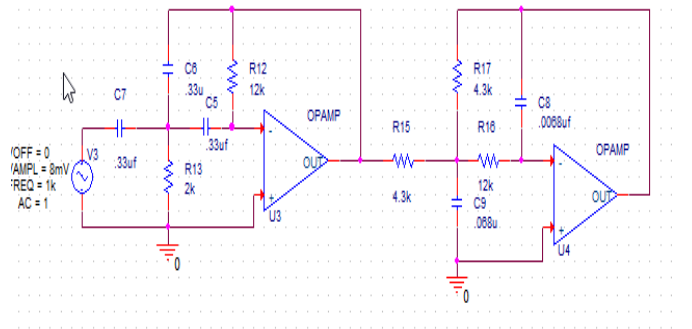


**Figure 3. Bandpass Filter Circuit**

## Voltage Supply and Analog-to-Digital Conversion

The supply voltage for this circuit was 5V, and a charge pump voltage inverter TPS60403 was used to create a -5V supply (see Figure 4). This was needed to properly bias the op-amps for the filtering sub-circuit.

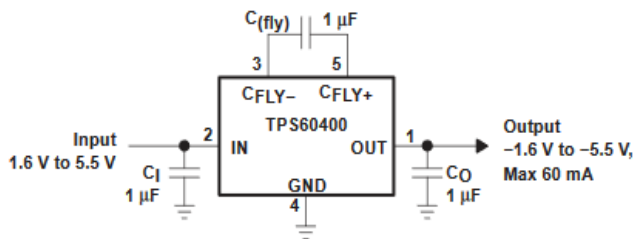


Figure 4. Negative Five-Volt Supply

The analog-to-digital converter (ADC) in the particle photon micro-controller cannot accommodate negative voltages. This is needed to correctly view a full heartbeat signal. In order to alleviate this issue, a voltage divider from VCC to GND was created at the output, and capacitor was added to filter and stabilize it.

## Particle Photon Code

First, the sensor has to determine if the input signal has passed a threshold. This indicates that the sensor has been placed in the correct position. This is done in conjunction with the robotic system. To start the sensor and have it be able to store a reading into a temporary array, a 1-second heart reading is needed. Once that array is full, it will iterate through it until a global maximum is found. This is then stored to a variable, turned into a JSON string, and sent to the robot over UDP/TCP to determine if the threshold has been reached. If the threshold has been reached, a full 3-to-5-second reading is taken and stored in the main array. The array is iterated through to find the global maximum, which then is used to normalize the array. Once this has been found, a tolerance level/range will be created. The array will then once again be iterated through, but this time starting at the global maximum. This continues until a value in the tolerance range is found. Both points will then be used to take the difference in time, and then divide by a minute to find the BPM, as shown in Equation (8):

$$BPM = \frac{\Delta Max \cdot SampleRate}{60seconds} \quad (8)$$

If this BPM is within a reasonable range then the heart data array is turned into a binary string and added into a JSON string. This JSON string also includes the calculated BPM. Then using UDP/TCP, this string is sent to the IP of the Raspberry Pi for it to add into the PostgreSQL database.

## Web Programming: Backend

SQL is the main language for databases to insert, select, or even delete records. There are many different types of frameworks that help implement SQL databases. The one used in this current project was called PostgreSQL. Postgres is an object relational database management system (ORDBMS) and its main focus is helping users create database servers. These database servers are particularly useful for web interfacing, as it can handle many users at once, and connecting to PostgREST, which is a REST API that can be generated from a PostgreSQL database schema. This is good for prototyping and designing a structure for web queries. Node.js is a runtime framework of JavaScript. This specific framework is used to run JavaScript code on a server. This framework is becoming one the most used in web programming, being used by Microsoft, PayPal, etc. This framework allows the creation of web servers, which are known as nodes. These nodes are then allowed to run the core function of the network, whether that is file reading, I/O over the network, or just database queries. However, Node.js can only run on a server, thus making it difficult for use on the client side (i.e., a web page). So another web framework for node.js was created by the name of Express.js to solve this particular problem. Express.js is a Node.js web application framework. It works by creating server-side routes, which are URL handling codes. These codes are then declared as a function in another JS file. So when these codes are executed client-side, it can access the server-side Node.js scripts.

## Web Programming: Front End

React.js or React is another JavaScript library. This library is used for creating user interfaces over the web. The framework is component-based, meaning that changing the element states of the web page can be done dynamically and quickly. The scripts can also be written in a Document object Model (DOM), similar to how HTML and XML work. This is great for displaying and changing database records from a web page. In order to have access to the server-side code, specifically being the database, XMLHttpRequests needs to be implemented. An XMLHttpRequest (XHR) is part of the JavaScript API that allows programmers to send data back and forth between the front and back end of the web server, similar to how curl works in CLI.

---

## Robot Operating System (ROS)

ROS, or robot operating system, is used in robots around the world. ROS can only be used on Linux platforms, but can be used to simulate or control a real robot. ROS is built on the foundation of networking. This works off of the premise of publishers and subscribers. Publishers are a way to send data out to the public; the public in this case being an ROS topic. An ROS topic can be seen as a specific topic that is set up in the code or, in a real sense, a post office. The next portion is the subscriber; a subscriber can be seen as the townspeople. The townspeople will get a message that their mail has arrived, and then will go to the post office. In short, ROS works off of messages being posted to a topic by publishers. The subscribers, then, who are looking for the messages on that topic, will be “pinged” that there is a new message on that topic. The subscriber then takes that message and runs its callback function with that data/message.

## OpenCV

OpenCV is currently the best library out there for computer vision. OpenCV is an open source library for implementing computer vision. Computer vision is the method for helping a computer “see.” Computers are able to see using cameras. Taking the input from these cameras and running functions on them allows us to tell the computer/robots what is around them and what they should do in that environment. OpenCV has many functions to help with this, including face detection, finding contours, and even face recognition. It is also fully compatible with ROS.

## Point Cloud

A point cloud (PCL) is a method for viewing a set of 3D data points. These data points are usually found or are taken from a 3D camera. While OpenCV is great at finding requested objects, it can only do this in (X, Y) cords. However, if the OpenCV data were used in conjunction with a PCL, the full X, Y, Z cords of a desired object could be found. For this current project, this full cord was implemented in order to find the position of the human heart.

## Results

The sensor should be able to take in a small analog signal and amplify it. After amplification, though, there needs to be filtering to clean up the signal and remove unwanted noises such as breathing. The amplifier needs to amplify the small signal to a usable voltage of, at most, 10 volts. Though if the voltage is ever too high, the filters should

have their own de-amplification factor to correct this. The website needs to be run on a local server and allow full access to the majority of the staff. The website allows the users to choose and view patient data from a large table. After choosing the full record, the viewer will be shown past heart data graphs.

Finally the robot must know when a human is in front of it, and then pick up and place the sensor onto the patient’s heart. The pre-amplifier circuit worked quite well with the values of components that were chosen. The JFET was properly biased, thus allowing output from the microphone. This output was quite small, around 3-5 mV, and was then amplified to a maximum of 10V. This value of amplification would vary with the input frequency, as indicated by the graph of Figure 5, which shows the frequency response of the amplifier.

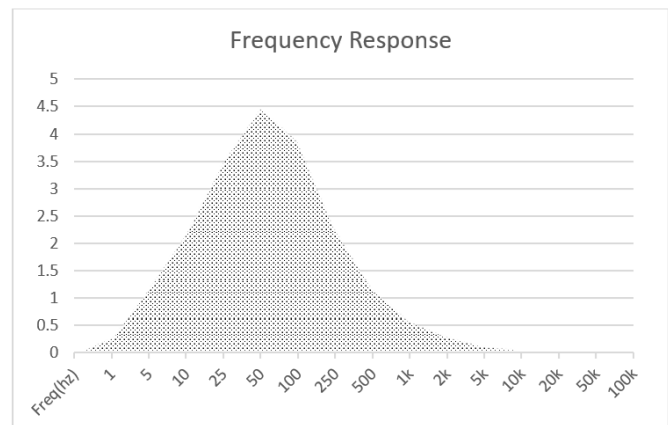


**Figure 5. Frequency Response of Pre-Amplifier**

The multiple band-pass filter was created by cascading an LPF and an HPF. The first design used a 0.7 quality factor. However, since it did not have a steep enough roll off, it was changed to 0.85. This design was implemented using a Butterworth filter and an order of two. The chosen center frequencies were based on the sounds of the heart. Taking an FFT of these signals allowed the researchers to accurately design the filter to fit this range [5, 6]. Figure 6 shows the four main sounds of the heart: S1, S2, S3, and S4, which occur when both sides of the heart’s muscles open and close. S1 is, obviously, the loudest, and takes place when the muscles close on the right side of the heart. This part of the heartbeat, much like the others, has multiple frequencies that must be designed for, rather than creating many BPF for each one. Thus, a single wide-bandwidth BPF was created.

After the signal is filtered, a step that lowers the voltage to around 3-4 volts, it needs to be regulated in order to avoid accidentally blowing up a micro-controller analog input.



This regulation was done with a 3V Zener diode in parallel with a 1KΩ resistor. The final step was to compensate for how the ADC works in the particle photon code. These inputs do have an internal ADC, however the inputs do not work with negative voltage values. In order to alleviate this, the circuit described next was implemented. The particle photon code was implemented and able to find a BPM using the method discussed earlier. Using Putty, a serial monitor was able to print out the sensor data. Figure 7 shows this plot, the digital output of the heartbeat sensor, which is a more visual way to view the array's elements.

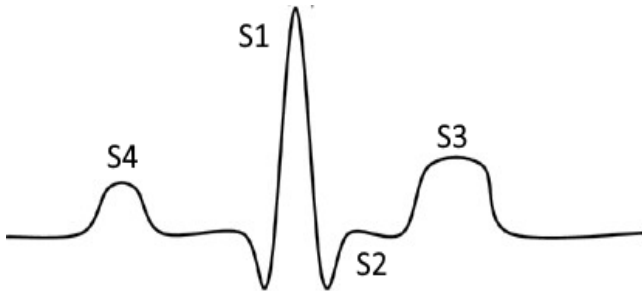


Figure 6. Heart Sounds

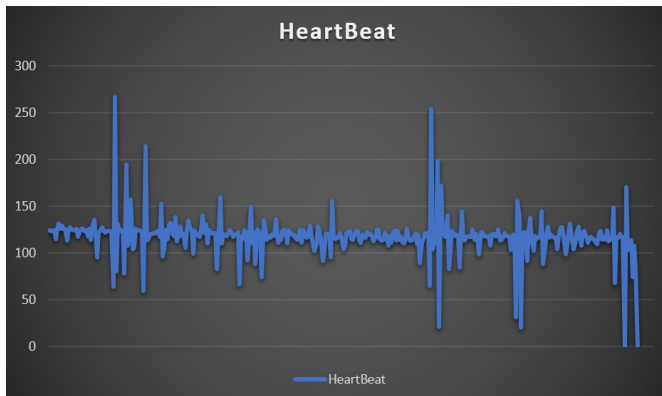


Figure 7. Graphed output from the heartbeat Sensor

PostgreSQL was implemented for this project as the SQL framework of choice. The database schema was created using Knex.JS, which allows us to dynamically change a database's schema as it evolves. This is done using migrations. Migrations are called from the CLI when the schema needs to be changed. The prototype web server was implemented on a Raspberry Pi 3. This server has multiple sections to it. The React JS web page is its own server. Express routing is another server. With both of these servers running, crosstalk between the front end and back end is allowed. Each of these processes needs to be executed in order for the system's servers to talk to one another. Figure 8 shows the back end and the front end of the web page running in a CLI.

```

antonio@Marie: ~/Desktop/ReactAndPG/node-postgres-promises
POST /api/puppies/200 7.506 ms - 59
GET /api/puppies/200 1.081 ms - 1922
GET /api/puppies/200 1.045 ms - 1922
GET / 200 679.315 ms - 170
GET /stylesheets/style.css 200 9.147 ms - 111
GET /favicon.ico 100 0.550 ms - 52
GET /users 200 1.060 ms - 64
^C
antonio@Marie: ~/Desktop/ReactAndPG/node-postgres-promises$ PORT=3001 bin/www
GET /api/puppies/5 200 63.636 ms - 120
GET /api/puppies/200 4.522 ms - 1922
GET /users 304 3.009 ms - -
GET /api/puppies/5 200 6.328 ms - 120
GET /api/puppies/5 304 0.097 ms - -
GET /api/puppies/5 304 4.001 ms - -
^C

antonio@Marie: ~/Desktop/ReactAndPG/node-postgres-promises/web_client
Compiled successfully!
You can now view web_client in the browser.
Local: http://localhost:3000/
On Your Network: http://10.0.2.15:3000/
Note that the development build is not optimized.
To create a production build, use npm run build.
^C

```

Figure 8. Web Server Running in CLI

As can be seen in the figures shown above, the requests that the react server makes are shown on the express server. If the code before the desired command is 200 or 304, the request is valid and will be executed. This allows the express server to take the URL code from the XMLHttpRequest and run the coinciding Node.js script. Figure 9 shows the Node.js scripts for accessing the database stored in queries.js, which is also where all of the declared routes are defined. This process starts by creating a connection string to the database and a query using that connection. For security purposes, the connection string allows the user to login to an existing account.

```

req.body.age = parseInt(req.body.age);
//set up the sql query
db.result('insert into pups(name, breed, age, sex)' +
  'values(${name}, ${breed}, ${age}, ${sex}) returning id', req.body)
  //tt= t.rows[0].id
  .then(function(data) {
    res.status(200)
    .json({
      status: 'success',
      message: 'Inserted One puppy',
      id: data.rows[0].id
    });
  })
  .catch(function(err){
    return next(err);
  });

```

Figure 9. Database Query

The robot of choice, Baxter, runs using ROS. Baxter needs to be able to find the patient in front of him and then that person's heart position in X,Y,Z cords by using a face-detection node along with the radius of the face. Then a ratio of how far the heart is from the face origin can be found. This is done using OpenCV libraries after which the cords are published to an ROS topic, "heartxy." Now that the X,Y cords have been found, they can be used to find the Z cord. And since the camera that Baxter is using to see is a Kinect, this allows the use of 3D camera data and the point

---

cloud library. The X,Y cords were found by subscribing to “heartxy” then they were sent to a function that takes in X,Y, a point cloud, and returns a Z cord. This is then sent out on a new ROS topic, “heartxyz.”

Baxter’s main computer subscribed to this topic and used these cords in conjunction with a python library of forward kinematics to place the sensor on the patient. Once this sensor was placed, a message was sent to the sensor over UDP/TCP. This message tells the sensor to run the threshold test. The threshold test took a short reading to find a maximum value, which was then sent back to the robot, where Baxter would decide if the reading had reached a threshold or not. If so, Baxter would send another message to the sensor to indicate that the full reading could be taken. However, if the reading did not reach the threshold, Baxter would move the sensor up or down and then repeat the test. This was done until a suitable reading was found. Baxter also used previous test iterations to tune in to the correct direction of the heart.

## Future Work

In the future, improving the bandpass filter to work on a smaller bandwidth would help eliminate the unwanted spikes from the sensor output. This system is already variable and expandable, since a humanoid robot is the robot of choice. Meaning, if more sensors were created to find other vitals, such as blood pressure, the pre-screening process could be shortened even further.

## Conclusions

The individual components and the choice in technology worked well. The same can be said for having all of the individual components talk to one another. Creating a sensor to talk to robots confirms the idea that a robotic doctor/nurse could be a possible future piece of technology. The results are promising as well, since both humans and robots can use the custom sensor to take their vitals. The use of IoT and robotics allowed the system to work on its own and, on the demand of humans, the data could be shown on any device.

## References

- [1] Ackerman, E. (n.d.). Diligent Robotics Bringing Autonomous Mobile Manipulation to Hospitals - IEEE Spectrum. Retrieved from <https://spectrum.ieee.org/automaton/robotics/industrial-robots/diligent-robotics-bringing-autonomous-mobile-manipulation-to-hospitals>
- [2] Perry, T. S. (2013). Profile: Veebot - IEEE Spectrum. Retrieved from <https://spectrum.ieee.org/robotics/medical-robots/profile-veeboot>
- [3] PARO Therapeutic Robot. (n.d.). Retrieved from <http://www.parorobots.com/>
- [4] Day, R. J., & Salehi, H. S. (2018). Development of Smart Interior Mobile App for Health Monitoring. *Proceedings of IEEE GreenTech*, Austin, TX.
- [5] Debbal, S. M., & Bereksi-Reguig, F. (2007). Time-frequency analysis of the first and the second heart-beat sounds. *Elsevier Applied Mathematics and Computation*, 184(2), 1041-1052.
- [6] Pichon, A., Roulaud, M., Antoine-Jonville, S., de Bisschop, C., & Denjean, A. (2006). Spectral analysis of heart rate variability: interchangeability between autoregressive analysis and fast Fourier transform. *Elsevier Journal of Electrocardiology*, 39(1), 31-37.
- [7] BBC.com. (2016). Pepper robot to work in Belgian hospitals. Retrieved from <http://www.bbc.com/news/technology-36528253>
- [8] How Do Stethoscopes Work? Here’s An Easy Explanation. (2016). Retrieved from <http://dmelibrary.com/how-do-stethoscopes-work>
- [9] Texas Instruments. (2015). Single-Supply, Electret Microphone Pre-Amplifier Reference Design. Retrieved from <http://www.ti.com/lit/ug/tidu765/tidu765.pdf>

## Biographies

**ANTONIO MORALES** is a student at the University of Hartford in the Electrical and Computer Engineering Department working on a BS in Electrical Engineering degree with a double major in Computer Science. Mr. Morales helped run multiple clubs (IEEE, Computing Club, and Game Development), and received second place in the University of Hartford’s CETA design expo in 2018. He has also published a paper in the proceedings of ASEE. His research interests include AI and creating a robot doctor/nurse to diagnosis patients. Mr. Morales may be reached at [antmorale@hartford.edu](mailto:antmorale@hartford.edu)

**HASSAN S. SALEHI** received his PhD—entirely funded by the National Institutes of Health (NIH)—in electrical engineering from the University of Connecticut. Dr. Salehi is an assistant professor of electrical and computer engineering at California State University, Chico. Previously, he was a faculty member in the Department of Electrical and Computer Engineering at the University of Hartford. He is the recipient of several teaching and research awards, including 2016-2017 Professor of the Year Award from the University of Hartford, College of Engineering, and two Pre-doctoral

---

Research Fellowship Awards from UConn. His research interests include development of novel biomedical imaging and sensing systems, bioinstrumentation, signal and image processing, as well as machine learning and pattern recognition for healthcare and medical applications. He also conducts research on Internet of Things (IoT) devices and sensors with a focus on health monitoring and analytics. Dr. Salehi has published over 20 peer-reviewed journal and conference articles in the field, and has given talks at several international conferences. One of his research papers was featured on the cover of the Journal of Oral Radiology. Dr. Salehi is a member of the Institute of Electrical and Electronics Engineers (IEEE), Optical Society of America (OSA), and International Society for Optics and Photonics (SPIE). Dr. Salehi may be reached at [hsalehi@csuchico.edu](mailto:hsalehi@csuchico.edu)

**KIWON SOHN** received his BS and MS degrees in electrical engineering from Kyungpook National University, Daegu, South Korea, and the University of Pennsylvania in 2005 and 2007, respectively. He received his PhD in mechanical engineering from Drexel University in 2014. He served as Chief of Engineering in team DRC-HUBO@UNLV (the finalist of DARPA Robotics Challenge Finals) and DASL (Drones and Autonomous Systems Lab) at the University of Nevada, Las Vegas, between 2014 and 2016. He is an assistant professor at the University of Hartford. Professor Sohn is a member of ASME and IEEE Robotics and Automation society. Dr. Sohn may be reached at [sohn@hartford.edu](mailto:sohn@hartford.edu)



# DESIGN AND IMPLEMENTATION OF AN ALTERNATIVE, LOW-COST WATER CHLORINATION SYSTEM IN EL CERCADO, DOMINICAN REPUBLIC

---

Truc T. Ngo, University of San Diego; Jeremiah Medina, University of San Diego; David White, University of San Diego; Danford Jooste, University of San Diego; Karly Jerman, University of San Diego; Jeremy Hagen, University of San Diego; Joanne Peterson, El Cercado, San Juan, Dominican Republic

## Abstract

Cholera has affected millions of people around the world, especially those living in underdeveloped/unserved regions. Contaminated water and food sources are major causes of this highly contagious disease. In this study, an alternative, low-cost water chlorination system was designed, tested, and implemented in the rural town of El Cercado in the Dominican Republic. Data obtained from laboratory testing were used as guide points for field implementation. Working alongside local Dominicans, ten systems were successfully installed in El Cercado over a three-year period. Field data showed that the chlorination system was reliable, effective, affordable, and easy to operate and maintain. Community partnership played an important role in the success of the project.

## Introduction

Cholera is a diarrheal illness that has been around for centuries, dating back as far as the fifth century B.C. [1]. The causative agent of cholera is the bacterium *Vibrio cholerae*, which can kill within days or even hours if it goes untreated [2, 3]. Cholera has affected millions of people around the world, especially those living in underdeveloped/unserved regions. Based on 2013 data published by the World Health Organization (WHO), 1.4 to 4.3 million people have been affected by cholera with 28,000 to 142,000 deaths each year [4].

People are especially vulnerable to a cholera outbreak following a natural disaster event, such as an earthquake or hurricane, due to unsanitary living conditions and contaminated water and food sources [1, 5]. For example, the 2010 Haiti earthquake initiated a major cholera outbreak in the country and also spread around the world. This incidence alone resulted in 712,330 suspected cholera cases with 8,655 cholera-related deaths, reported by the government of Haiti between October 2010 and October 2014 [6]. This outbreak spread quickly to the neighboring Dominican Republic, with 20,000 reported cases and 371 deaths in 2011 [7].

The Dominican Republic has been affected by cholera for many years. The country has a population of approximately 10.5 million people as of 2015, with over 77% of the population living in urban areas [8]. Rural regions are most impacted, due to several factors. According to the U.S. Centers for Disease Control and Prevention (CDC), drinking untreated river water was considered to be the most likely source of cholera infection [9]. Many of the cholera-related cases in the Dominican Republic were also connected with travel to Haiti and the constant influx of Haitian immigrants into the country, particularly in rural areas. The effects worsened following the 2010 Haiti earthquakes.

Another factor that influenced the cholera vulnerability of the Dominicans is the rapid industrialization of the country over the past two decades. Fast economic growth (mainly in manufacturing and tourism) has led to rapid migration of people from rural to urban areas, leaving their traditional agricultural jobs in search of higher-paid manufacturing jobs in the cities [10]. The government has also cut back on social support, such as health and education, in order to invest more in industrial growth of the country. In addition, younger populations, who had opportunities to attend college in major cities, tended to stay in larger cities rather than coming back to help their rural towns. Consequently, the number of people living in poverty in rural regions of the country has increased with limited access to water and sanitation services. The rural population has become more isolated, less educated, and less skilled.

The aim of this study was to design, test, and implement an alternative, low-cost water chlorination system for the rural villages around El Cercado in the Dominican Republic. Green engineering principles were incorporated throughout the product/system design and implementation stages. A cost analysis was also performed to assess system affordability and long-term sustainability for local Dominicans. El Cercado is a rural town in the southwest region of the country, in San Juan province, and located approximately 22 km to the east of the border with Haiti. It has a population of approximately 25,000 people, including the city center and surrounding villages [11]. According to the official document provided by the Parroquia San Pedro, there were

---

17 water distribution systems for the villages around El Cercado in 2012. There are several others either recently built or currently under construction, sponsored by the government or the Parroquia San Pedro since 2012. Due to the lack of governmental support, these systems only route water from its source to a central location in a village, then distribute the water to local households or other downstream villages through underground PVC piping without treatment. Water from these sources is often found to be contaminated with E- coli and other bacteria and classified as unsafe to drink [12-14].

Although boiling water before drinking is a frequent recommendation of health promotion programs in the Dominican Republic, a very small percentage of people choose to do so, especially when their children become older than twelve months [15]. Other household water treatments that have been used in El Cercado include chlorination, biosand filters, ceramic filters, and activated carbon filters. Most of these treatments at point of use were discontinued after short trials. The reasons for halting the practices varied from unpleasant taste, frequent breakdown of equipment, high costs, and lack of knowledge on how to use and maintain the equipment, to simply dislike of the product, which is consistent with other previously reported survey results [12, 13, 16, 17]. Consequently, villagers living in the rural areas where governmental support is absent are subjected to a higher risk of cholera, due to direct consumption of untreated water.

## Methodology

This project was implemented in three main stages: 1) designing the water chlorination system; 2) testing system performance within a laboratory environment and defining its limitations; and, 3) field implementation of the system. El Cercado was selected for three main reasons. First, El Cercado has several rural villages around the town center that currently have limited or no social support from the government. Second, there have been several cholera outbreaks in some of these villages within recent years. Third, a majority of the households in these areas do not currently use any home water treatment method, and simply consume water directly from their taps.

## Design of the Water Chlorination System

Chlorination is an effective, chemical disinfection method that has been used in many developed and developing countries for decades [18]. Other commonly available water disinfection methods include boiling and ultraviolet (UV) radiation. Boiling of water is recommended by most health pro-

motion programs; however, it is only appropriate as a treatment method at point of use [16]. UV radiation treatment, from either the sun or an artificial UV source, requires favorable climate conditions or a power source. It is often expensive and only effective when treating relatively clear water [17]. Chlorine treatment at point of use (i.e., households) often gives an unpleasant taste to the water, especially when the end users do not apply the correct dosage to their water prior to consumption. Because of the unreliability at household treatment, the point of chlorination in this project was selected to be at the central water storage reservoirs (151,416 – 170,344 L capacity). The central reservoirs supply water to individual households within the village or to villages downstream. These large reservoirs serve as settling tanks for the water, and larger particles inside the water are removed through sedimentation.

The location of interception point for chlorine treatment was chosen to be before the water entered the settling tanks so that chlorine had some time to disinfect the water before it reached the end users. The location often depended on geography constraints of the implementation site. Also, chlorine tablets were selected over liquid chlorine, due to their local availability, cost, and ease of handling and maintenance. In addition to treatment effectiveness, the water chlorination system was designed according to green engineering principles developed by Anastas and Zimmerman [19]. Cost, ease of operation, and maintenance were also important factors influencing system design. The innovation of this project was the creative incorporation of environmental, economic, social, and cultural factors into the adaptation of a low-cost, commercially available chlorinator unit to disinfect the water at local distribution centers for the El Cercado community.

## Testing of the Water Chlorination System under Laboratory Settings

The current system can employ a variety of automatic inline chlorinators. Key selection criteria include cost, ease of operation and maintenance, convenient adjustment of chlorine dosage, and flexible adaptability to standard PVC pipe fittings. For laboratory testing, a WaterWay automatic inline chlorinator with clear walls was selected, due to convenient availability. More importantly, it is commercially available locally in the Dominican Republic. The chlorinator was loaded with 0.076-m chlorine tablets (Pool Time Plus, 94.05% trichloro-s-triazinetriene) and fitted to PVC pipes, which connected a water source to a collector. The water source was a standard faucet located inside the laboratory, supplied directly by the city of San Diego. Water characteristics, including temperature, total dissolved solids (TDS), pH, total hardness, iron contents, free and total chlo-

rine, were measured both at the source and after the chlorinator approximately 120 s after active chlorination. The chlorinated water was then stored up to 24h in a plastic container at room temperature after which water characteristics were re-measured to check for any property degradation.

## Field Implementation of the Water Chlorination System

After fundamental characterizations of the inline water chlorinator's performance and limitations, the system was implemented at ten different sites in El Cercado over a three-year time period. Automatic inline water chlorinators made from two different manufacturers were tested in the field (WaterWay and Ocean Blue), because of a relatively small inventory of supplies carried by local hardware stores and parts availability at the time of installation. These two types had similar operating principles, with minor differences in water inlet and outlet design. One WaterWay unit could hold up to eight, 0.076m chlorine tablets, whereas the Ocean Blue unit could hold up to twelve tablets.

The implementation sites were selected by El Cercado community leaders/organizers based on need, geographical feasibility, and level of commitment on the part of community members. Moreover, the selected communities already had existing water committees with dedicated members, who were willing to participate in the training of system installation and be responsible for system maintenance and repair. El Cercado communities varied in size, ranging from 50 to 200 household units each. Some were located in mountainous terrains. Water sources were mostly underground springs originating from nearby mountains. Water was gravity fed to the collection reservoirs without any additional pumps. Implementation point and system design had to be custom fitted to the geographical limitations at each site. Water samples were collected at the source and the point of installation. Pre- and post-installation chlorine contents were also checked at three households inside the village along the water distribution line: at the beginning of the line, one near the center, and one towards the end of the line. These water samples were retained for 24 hours and chlorine levels were re-measured for comparison.

## Results and Discussion

### Laboratory Testing

In order to characterize the fundamental behaviors and performance of the WaterWay chlorinator, a small system was designed and tested in the laboratory. Figure 1 shows a schematic of the lab-scaled water chlorination system. Two

1040-liter plastic tanks were used as a water source and a collection reservoir, respectively, and set at different elevations to promote gravity flow of the water. A flowmeter (GPI flowmeter, part number TM200-N) was installed along the PVC pipeline connecting the two tanks in order to measure water flow rate coming in to the chlorinator. A chlorinator (WaterWay automatic inline clear, model CLC012) was installed vertically along the horizontal PVC pipeline section of the system prior to the collection tank.

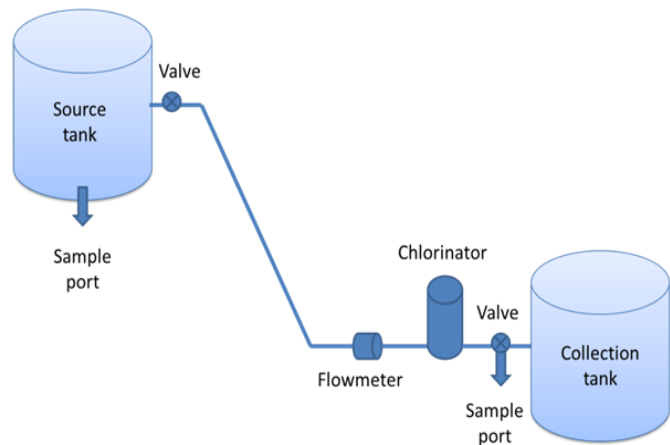


**Figure 1. Water Chlorination Setup under Laboratory Settings**

Initial testing without using chlorine tablets was performed to determine the minimum water flow rate required for the chlorinator to work. During these tests, a submersible pump was placed inside the collection tank to recycle the collected water back into the source tank to prevent water waste. The minimum required incoming water flow rate to the chlorinator was determined to be 3.79 L/s in order for the water to enter the body compartment of the chlorinator. The lab system was limited to a maximum flow rate of 4.92 L/s. Under this maximum flow rate, the water rose to 0.084m above the bottom grate level of the chlorinator, which completely covered three chlorine tablets stacked directly on one another inside the chlorinator (each tablet was 0.0305m thick). It was expected that the water level would rise higher for a higher flow rate, but this was not tested with the lab system.

Four separate runs of active chlorination were performed, with initial operational conditions and results shown in Table 1. For each run, three chlorine tablets were stacked inside the chlorinator, and water was passed through the system at a maximum flow rate of 4.92 L/s for a total of 150s to 180s before the source tank was depleted below the pump's minimum operating level. Water temperature, pH, TDS, total hardness, and free and total chlorine were measured at two locations: the source tank before chlorinator and the sample port directly after the chlorinator. A water sam-



**Table 1. Water Characteristics from Laboratory Testing**

Water characteristics	Measuring tool (manufacturer / model)	Source	Post chlorinator (after 120s of active chlorination)	After 24 hours of storage	
				Source	Post chlorinator
Temperature (°C)	Multi-Thermometer / - 50°C+300°C	23.5 ± 0.4	23.5 ± 0.5	24.6 ± 0.2	24.6 ± 0.2
pH	American Marine Inc. / Pinpoint	7.78 ± 0.24	7.89 ± 0.05	7.81 ± 0.06	7.88 ± 0.02
TDS (ppm)	HM Digital / TDS-EZ	444 ± 10	442 ± 19	446 ± 4	453 ± 7
Total hardness (ppm CaCO <sub>3</sub> )	CHEMetrics / K-4585	243 ± 13	235 ± 4	233 ± 5	245 ± 10
Free chlorine (ppm)	Oakton / C301	0.10 ± 0.02	0.21 ± 0.04	0.11 ± 0.06	0.11 ± 0.08
Total chlorine (ppm)	Oakton / C301	0.55 ± 0.30	1.07 ± 0.30	0.16 ± 0.04	0.25 ± 0.17

(reported as average ± one standard deviation, over 4 separate runs)

ple was only collected at the sample port post chlorinator after 120s of active chlorination. Each water sample was then stored (with a cover) at room temperature for 24 hours after which the same water characteristics were re-measured. Additionally, nitrate, nitrite, and iron contents were checked and found to be zero or negligible and, thus, not reported in Table 1. This was expected for the average city water supply in the U.S. per Environmental Protection Agency requirements.

Laboratory testing in San Diego, California, proved the feasibility of the automatic inline chlorination system for an incoming water flow rate of at least 4.92 L/s. With only 120s of active chlorination and three chlorine tablets present inside the chlorinator chamber, the chlorinator was able to double both free and total chlorine contents in the water (see Table 1). It was also noted that the original water source already contained a low level of free chlorine (0.10 ppm). This was expected, because the U.S. treats its water supply with chlorine before supplying it to customers. Additional chlorination by the inline chlorinator did not seem to affect pH, total dissolved solids, or hardness of the water. The U.S. CDC’s Safe Water System project recommends between 0.2 and 2.0 ppm as the target range for free chlorine in the water to ensure safe drinking [20]. Additionally, the U.S. Environmental Protection Agency (EPA) states that the maximum residual disinfectant level goal (i.e., the level below which there is no known or expected health risk) for free chlorine is 4.0 ppm [21].

A two-tail t-test was performed on laboratory data collected for chlorine levels. Free chlorine levels post treatment showed statistically significant improvement compared to

the free chlorine levels before treatment ( $t\text{-Stat} = -4.49 < -t$  Critical two-tail =  $-2.57$ ;  $p\text{-value} = 0.006 < 0.05$ ). The total post-treatment chlorine levels also showed an increase compared to pre-treatment levels, though were not statistically significant ( $p\text{-value} = 0.05$ ). Free chlorine was the most critical variable in this case, as it indicated the amount of active chlorine available to react and kill any bacteria present in the water. These results proved the feasibility of the tested chlorination system and provided a basis for advancing to the next phase of field implementation.

One concern over the laboratory data was that the free chlorine content in the water seemed to deteriorate below the CDC-recommended minimum level for safe drinking (0.2 ppm) after being stored at room temperature for 24 hours. However, if the system was to be operated longer (at least one hour of active chlorination) and more chlorine tablets were present inside the chlorinator, the initial active chlorine level could be improved.

## Field Implementation

Due to geographical limitations, the connections between the chlorinator and the existing water line had to be modified and custom-fit during site implementation. When the point of installation had ample open space on level ground, the chlorinator installation was less complicated and followed a linear configuration, as shown in Figure 2. On the other hand, if space is constrained, a more creative configuration with multiple 90° connections may be required for the system assembly. Regardless of geographical constraints, a reversible, threaded expansion coupling was used between

the upstream valve and the chlorinator. A second threaded union was also added immediately downstream of the chlorinator (see Figure 2). This threaded coupling and union were not needed during laboratory testing, given the small-scale system, the flexibility and mobility of PVC piping, and receiving tank location. For large-scale and fixed-field systems, threaded and reversible connections were necessary to allow convenient disassembly of the chlorinator unit during maintenance and repair. Depending on which type of water chlorinator or pipe size of the existing water line are being used, additional pipe adapters may be required to connect the chlorinator unit to the main water line, as illustrated in Figure 2.

Incoming water flow rates varied from one site to another, depending on the relative elevation of the water reservoir to the original water source. For faster water flow rates (at least 3.79 L/s), the WaterWay chlorinator had to receive incoming water and dispense chlorinated water in the same fashion as in prior lab tests. The WaterWay chlorinator was made out of PVC schedule 40 high-pressure-rated plastic, and was thus able to withstand higher pressure and flow rates. On the other hand, the Ocean Blue chlorinator worked better at slower flow rates (as low as 1.5 L/s), due to a simpler design of its water inlet mechanism. At a flow rate of 1.5 L/s, water readily entered the inner chamber of the Ocean Blue chlorinator within ten seconds of active flow. It was also noted that the Ocean Blue chlorinator was constructed out of low-pressure-rated plastic. As a result, a high water flow rate and pressure could physically damage the chlorinator.

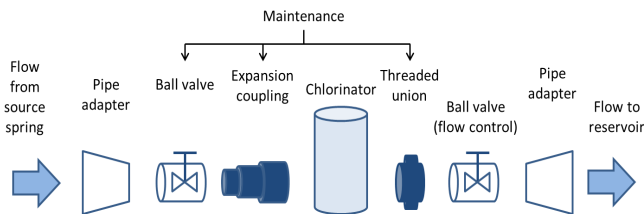


**Figure 2. Example of Water Chlorinator Installation in the Pinal de la Cana, Batista Site**

Water characteristics were measured at ten different implementation sites in El Cercado before and after installation of the chlorination system, using the same measuring tools as in laboratory testing. Spring source data was only available for one site, due to challenging terrains and weather conditions to access all of the sources in the mountains. Household water samples were collected at three locations within the serving community: House 1 (closest unit to the collection tank); House 2 (center unit); and, House 3 (last unit along the distribution line). Results shown in Table 2 were collected over a three-year period in both winter and

summer seasons. Due to a high level of geographical variation from one installation site to another, and its effect on chlorine treatment, water-characteristic data are shown as ranges of values in Table 2, taking into account both storage reservoir and household measurements at all ten sites. Free and total chlorine data, post chlorination, are reported for households and storage reservoirs (labeled as “Tank”) separately to show changes along the water distribution lines.

Water sources in El Cercado showed different characteristics compared to the tap water source in San Diego, California. Specifically, El Cercado water sources had significantly less dissolved solids and less  $\text{CaCO}_3$  contents, meaning that the water was much softer (see Table 2). This was most likely because the El Cercado water was not treated, whereas U.S. water often received a series of treatments before reaching the end users. Levy et al. [22] noted that some water characteristics could significantly influence effectiveness of the treatment, so system tuning was expected to be different in the field compared to laboratory tests. Similar to test results collected in the laboratory in the U.S., iron and nitrite were either absent or negligible in El Cercado’s water. A low but noticeable amount of chlorine was measured at both source and household collections (less than 0.1 ppm of free chlorine and less than 0.2 ppm of total chlorine). Chlorine trace could be associated with underground soil and old PVC piping from source to end users. A consistently small amount of nitrate was also present in all water samples before and after chlorinator installation (0.4 – 1.0 ppm). This was most likely linked to close-by farms and uncontrolled animal feces along the water sources/lines. Inline chlorination of the water slightly increased the pH and TDS levels, as expected. However, other water characteristics seemed to be unaffected.

Despite the differences in water characteristics, the inline chlorinators in the field were still able to increase active chlorine contents in the water by at least one order of magnitude, bringing free chlorine level from essentially 0 ppm to as high as 2.11 ppm at the central storage tank. Results were consistent for systems monitored over the three-year period. This level meets the safe limit for drinking water recommended by the CDC and EPA. However, in larger communities (> 50 households) chlorine content seemed to drop below the minimum 0.2 ppm level recommended by the CDC (2015) towards the end of the distribution line. Raising the chlorine level further would negatively affect the water taste for the first households along the water distribution line. A better solution to this problem would be to install additional chlorinators along the line after approximately every 50 household units. This proposal was communicated to local leaders and turned into a future project for the community to own and plan accordingly.

**Table 2. Water Characteristics in El Cercado, Dominican Republic**

Water characteristics	Spring source	Prior to chlorinator installation	After at least 24 hours of active chlorination			
			Tank	House 1	House 2	House 3
Temperature (°C)	22.1	21.9 – 29.7	21.9 – 32.4			
pH	7.13	6.8 – 8.0	7.6 – 8.1			
TDS (ppm)	165	143 – 177	148 – 186			
Total hardness (ppm CaCO <sub>3</sub> )	180	140 – 180	115 – 180			
Free chlorine (ppm)	0.05	0.00 – 0.12	0.62 – 1.89	0.39 – 1.00	0.32 – 0.70	0.11 – 0.51
Total chlorine (ppm)	0.09	0.00 – 0.12	0.62 – 2.11	0.61 – 1.10	0.36 – 0.80	0.11 – 0.57

The effect of water storage on chlorine degradation was also tested for six sites. Free chlorine content seemed to degrade significantly after 22 hours of storage in closed plastic containers at room temperature, as previously reported by Blair et al. [23]. To ensure that free chlorine levels would stay above the 0.2 ppm minimum recommendation by the CDC after long-term storage, initial chlorine content inside the water needed to be approximately 2.0 ppm. One negative side effect for this method is the unpleasant chlorine odor present in highly chlorinated water, which could turn the villagers away from drinking chlorinated water overall. Consequently, local villagers were advised to drink only fresh water and to use stored water for purposes other than drinking.

### Costs

Cost was one of the important considerations for designing and implementing of water chlorination system in this study. Total cost for the complete installation of one chlorinator unit was approximately \$150, depending on the type of inline chlorinator used. This estimate included materials used to construct a secured, protective housing unit around the chlorinator assembly. Parts were chosen to have sufficient strength and pressure rating to withstand water flow inside the chlorinator assembly, and were available for purchase at local hardware stores. Some components were threaded to allow convenient disassembly, whereas others had slip fits for permanent connections.

### Green Engineering Design

Besides performance effectiveness, a green engineering design was also an important factor for the water chlorination system. During laboratory tests, the water was recycled as much as possible, thus minimizing process wastes. Field

systems also produced zero waste during operation. This was a demonstration of the “prevention instead of treatment” green engineering principle [24]. “Design for separation” was another green engineering principle incorporated into the system design. The system consisted of several components that were assembled using appropriate adaptors and connectors. The chlorinator itself was connected to the remaining assembly through two reversible, threaded unions (see Figure 2). The threaded unions allowed convenient disassembly of the chlorinator unit during routine maintenance, repair, and part replacement. All connections and piping in the assembly were made out of thermoset polymers, mostly polyvinyl chloride (PVC). Material diversity was minimized to facilitate recycling and waste treatment processing at the components’ end of life. Although the system was expected to have relatively long lifetime, the chlorinator unit was not designed to last indefinitely. The typical lifetime of automatic inline chlorinators is five to ten years, depending on the quality of the water running through the system and the chlorinator’s manufacturer. The system was designed based on durability rather than immortality, taking into account the possibility of advancing to an even more efficient and lower-cost system in the future.

### Community Partnership

The success of this project was highly dependent on community partnerships between the implementation team, local government, not-for-profit organizations, and local Dominicans. The project utilized a community-owned cost model for which community members provided funds to purchase parts and materials for system installation, whereas chlorine tablets were supplied by local health clinics operated by the local government. Work was sometimes subsidized by local not-for-profit organizations for remote communities with fewer households to share the cost.

---

Local communities were actively involved throughout the duration of the project. Feedback was solicited from community leaders with respect to geographical constraints, locally available materials, hands-on skills, and system affordability. Dominican villagers were integrated into the installation team, assisting with installation site selection, excavating the ground, fitting pipes, constructing a housing unit for the chlorinator assembly, sourcing information about water flow and usage, and mapping water distribution lines. Three hands-on training sessions were conducted for the locals over three consecutive years and reinforced with field installations, maintenance, and repairs. In addition, a system manual, with instructions on installation and maintenance, was provided to local community leaders in both English and Spanish. By empowering the people with proper knowledge, training, and skills, full system ownership and responsibility were transferred to the local community, enabling them to expand project implementation across the town on their own.

## Conclusions

An alternative, low-cost, inline water chlorination system was designed, tested, and implemented in ten rural communities in El Cercado, San Juan, Dominican Republic. The design of the water treatment solution in this study was based on cultural, social, economic, and sustainability factors rather than simply technology or modern engineering operations. Over a three-year period, the implemented system was demonstrated to be effective, reliable, affordable, easy to operate and maintain, and meet the needs of local communities. It also provided opportunities for the locals to gain technical skills and knowledge about water chlorination, thus promoting sustainable development for the region governed by the local people.

## Acknowledgements

The project was funded by various sources from the University of San Diego, including the Shiley-Marcos School of Engineering, International Opportunity Grant, Changemaker HUB, Associated Students, and the Provost's Enhanced Student-Faculty Interaction Grant, as well as from Father Sylvester Kwiatkowski of the St. Patrick Parish in Grass Valley, California. The authors would also like to thank the El Cercado communities for working patiently with the San Diego team to implement the water chlorination systems, and all of the volunteers that participated in humanitarian trips to the Dominican Republic between 2014 and 2017.

## References

- [1] Ball, L. (2009). Cholera and the Pump on Broad Street: The Life and Legacy of John Snow. *History Teacher*, 43, 105-119.
- [2] Colwell, R. R. (2006). Cholera Outbreaks and Ocean Climates. *Social Research*, 73, 753-760.
- [3] World Health Organization. (2015). Cholera. Retrieved from <http://www.who.int/mediacentre/factsheets/fs107/en>
- [4] World Health Organization. (2015). WHO Global Health Observatory Data. Retrieved from [http://www.who.int/gho/epidemic\\_diseases/cholera/cases\\_text/en](http://www.who.int/gho/epidemic_diseases/cholera/cases_text/en)
- [5] Sigman, M., & Luchette, F. A. (2012). Cholera: Something Old, Something New. *Surgical Infections*, 13, 216-222.
- [6] United Nations. (2014). United Nations Fact Sheet: Combating Cholera in Haiti. Retrieved from [http://www.un.org/News/dh/infocus/haiti/Haiti\\_Cholera\\_Snapshot\\_October\\_2014.pdf](http://www.un.org/News/dh/infocus/haiti/Haiti_Cholera_Snapshot_October_2014.pdf)
- [7] Lund, A. J., Keys, H. M., Leventhal, S., Foster, J. W., & Freeman, M. C. (2015). Prevalence of Cholera Risk Factors between Migrant Haitians and Dominicans in the Dominican Republic. *Pan American Journal of Public Health*, 37, 125-131.
- [8] UNICEF. (2015). State of the World's Children Country Statistical Information. Retrieved from <http://www.data.unicef.org>
- [9] United States Centers for Disease Control and Prevention. (2010). Updated on Cholera: Haiti, Dominican Republic, and Florida. *Morbidity and Mortality Weekly Report*, 59, 1637-1641.
- [10] Pomeroy, C., & Jacob, S. (2004). From Mangos to Manufacturing: Uneven Development and Its Impact on Social Well-Being in the Dominican Republic. *Social Indicator Research*, 65, 73-107.
- [11] Oficina Nacional de Estadística. (2002). Censo de Población y Vivienda. Retrieved from <http://www.one.gob.do>
- [12] Stauber, C. E., Ortiz, G. M., Loomis, D. P., & Sobsey, M. D. (2009). A Randomized Controlled Trial of the Concrete Biosand Filter and Its Impact on Diarrheal Disease in Bonao, Dominican Republic. *The American Journal of Tropical Medicine and Hygiene*, 80, 286-293.
- [13] Aiken, B. A., Stauber, C. E., Ortiz, G. M., & Sobsey, M. D. (2011). An Assessment of Continued Use and Health Impact of the Concrete Biosand Filter in Bonao, Dominican Republic. *The American Journal of Tropical Medicine and Hygiene*, 85, 309-317.



- 
- [14] Baum, R., Kayser, G., Stauber, C. E., & Sobsey, M. D. (2014). Assessing the Microbial Quality of Improved Drinking Water Sources: Results from the Dominican Republic. *The American Journal of Tropical Medicine and Hygiene*, 90, 121-123.
- [15] McLennan, J. D. (2000). Prevention of Diarrhea in a Poor District of Santo Domingo, Dominican Republic: Practices, Knowledge, and Barriers. *Journal of Health, Population and Nutrition*, 18, 15-22.
- [16] McLennan, J. D. (2000). To Boil or Not: Drinking Water for Children in a Periurban Barrio. *Social Science and Medicine*, 51, 1211-1220.
- [17] Centre for Affordable Water and Sanitation Technology (CAWST). (2015). Water Treatment Implementation for Developing Countries. Retrieved from <http://www.cawst.org/en/resources/pubs/position-papers/category/8-position-papers>
- [18] Henderson, A. K., Sack, R. B., & Toledo, E. (2005). A Comparison of Two Systems for Chlorinating Water in Rural Honduras. *Journal of Health, Population and Nutrition*, 23, 275-281.
- [19] Anastas, P. T., & Zimmerman, J. B. (2003). Design Through the Twelve Principles of Green Engineering. *Environmental Science and Technology*, 37, 94A-101A.
- [20] United States Centers for Disease Control and Prevention. (2015). The Safe Water System: Free Chlorine Testing. Retrieved from <http://www.cdc.gov/safewater/chlorine-residual-testing.html>
- [21] United States Environmental Protection Agency. (2015). Drinking Water Contaminants: National Primary Drinking Water Regulations. Retrieved from <http://water.epa.gov/drink/contaminants/index.cfm#one>
- [22] Levy, K., Anderson, L., Robb, K. A., Cevallos, W., Trueba, G., & Eisenberg, J. N. S. (2014). Household Effectiveness vs. Laboratory Efficacy of Point-of-Use Chlorination. *Water Research*, 54, 69-77.
- [23] Blair, S., Jooste, D., Bryant, D., Ashkar, C., Burt, S., Kuwahara, K., et al. (2016). Humanitarian Engineering Opportunities and Challenges in Rural Dominican Republic: A Case Study of El Cercado. *IEEE 2016 Global Humanitarian Technology Conference Proceedings, Paper # 978-1-5090-2432-2/16/\$31.00 ©2016 IEEE*, (pp. 709-717). Seattle, WA.
- [24] Allen, D. T., & Shonnard, D. R. (2012). *Sustainable Engineering: Concepts, Design and Case Studies*. (1<sup>st</sup> ed.). Prentice Hall.

## Biographies

**TRUC NGO** is an associate professor in the Industrial and Systems Engineering Department at the University of San Diego. She earned her bachelor's and PhD degrees (chemical engineering, 1997 and 2001, respectively) from the Georgia Institute of Technology. She also worked as a Senior Process Engineer at Intel Corporation prior to joining academia. Dr. Ngo is currently teaching in the Shiley-Marcos School of Engineering at the University of San Diego. Her research interests include supercritical fluid processing, polymers and composites, and humanitarian engineering. Dr. Ngo may be reached at [tngo@sandiego.edu](mailto:tngo@sandiego.edu)

**JEREMIAH MEDINA, DAVID WHITE, DANFORD JOOSTE, KARLY JERMAN, JEREMY HAGEN** were undergraduate students in the Shiley-Marcos School of Engineering at the University of San Diego at the time of research and project implementation. They have graduated from the university and are currently pursuing various career paths. These co-authors may be reached at [jmedina202@gmail.com](mailto:jmedina202@gmail.com), [davidwhite@sandiego.edu](mailto:davidwhite@sandiego.edu), [danfordjooste@sandiego.edu](mailto:danfordjooste@sandiego.edu), [karlyjerman@gmail.com](mailto:karlyjerman@gmail.com), and [jhagen@sandiego.edu](mailto:jhagen@sandiego.edu), respectively.

**JOANNE PETERSON** is the community organizer for El Cercado, Dominican Republic. She earned her BS degrees (Social Work and Sociology, 1975) from Brockport State University, and master's degree (Social Work in Organization and Planning, 1976) from Syracuse University. Ms. Peterson is currently working as the Community Organizer in the Dominican Republic in the southwest area of the country with four Catholic parishes in Sabana Yegua, Banica, Hondo Valle, and El Cercado. She works with youth, farmers' and women's associations, and Christian-based communities in the region. Ms. Peterson may be reached at [joanapeterson@hotmail.com](mailto:joanapeterson@hotmail.com)

# IMPLEMENTATION OF A BALL-AND-BEAM CONTROL SYSTEM USING PD BODE DESIGN

Jordan K. Ford, United States Coast Guard Academy; Tooran Emami, United States Coast Guard Academy

## Abstract

When students are first introduced to the world of automatic control systems, they often have a lot of information to deal with at one time. It is common to see concepts such as root locus, Routh Hurwitz, Bode design, and state space modeling all introduced in a single semester. Bode design, as one of many practical methods, is the one that the authors of this paper sought to focus primarily on in order to design a controller for a ball-and-beam system. In this study, the authors looked at the open-loop frequency response of a ball-and-beam system, more specifically the magnitude and phase responses, and applied constraints such as a certain gain crossover frequency and phase margin to design a proportional-derivative (PD) compensator.

## Introduction

Many studies from around the world focused on the dynamics, modeling, and controls of a ball-and-beam balancing system. A ball-and-beam system is one that tries to balance a circular object rolling on a dynamic beam, which is attached to a motor. For many years, scholars have modeled these systems to explore diverse types of controllers. A wide range of experiments involve ultrasound distance sensors alongside proportional-derivative (PD) controllers. In this paper, the authors evaluate the design and performance of a controller acting on a real-time ball-and-beam system. The design of Bode PD controllers were implemented via simulation in MATLAB. These controllers were applied to a real-time ball-and-beam system provided by Quanser Innovate Educate Inc. (see Figure 1) [1]. The authors also compare the results of design and implementation of the system. The work of O'Brien and Watkin [2] aided in this project and was used as a guide in this project.



Figure 1. Quanser Ball-and-Beam System

## Problem Statement

### Ball-and-Beam System

Control systems are fundamental aspects of life that are often taken for granted. These systems automate basic tasks by using control loops and mathematical feedback portions to perform tasks with more accuracy [3]. Ball-and-beam control models are projects that students undertake in order to understand control systems in general. Designing a ball-and-beam model, as opposed to any other model, is exponentially more rewarding for students for a number of reasons. The first reason is that these models are relatively simple to build, so students, in fact, spend the majority of their time designing a feedback control loop. The second reason is that there are myriad ways that these systems can be created, allowing students to explore their creativity. Another reason is that, while many controllers may perform well, none are perfect and could always be improved upon through experimentation.

### United States Coast Guard Applicability

The U.S. Coast Guard uses control systems aboard every cutter on a daily basis. Examples of systems aboard ships that are automated include, but are not limited to: navigation systems, heating ventilation and air conditioning systems, wireless communication systems, as well as radar range finding systems. One huge problem that the Coast Guard, as well as other military services, faces is that of refueling at sea. When ships refuel at sea they often must rely on the ship-handling abilities of two people to match the speeds of their vessels. This makes this task extremely dangerous. A controller, much like the one used in a ball-and-beam system, could be applied in this case to have one ship match the speed of the other or vice versa to eliminate error [4].

### Maritime Industry Applicability

Control systems are also already a large part of the commercial fleet in the maritime industry. The International Maritime Organization is currently making a push to reduce exhaust stack emissions of greenhouse gases. This problem is already being tackled with the design of hybrid ships that are battery powered. These ships use controls to engage

---

diesel engines to charge the batteries when they get low. Another problem with the maritime industry is that of pirates taking members of different ships hostage. If ships can get to the point where they are fully autonomous, then there will essentially be no people on board to be taken hostage. Rolls Royce has already started the design process for autonomous ships and plans to use many control systems in the implementation of autonomous ships. More specifically, they plan to use drones to provide maintenance and oversight at sea [5].

## Educational Relevance

In this current paper, the authors focus on the use of Bode plots and PD mechanics for controller design. There are reasons for which this method of design was chosen. Members from Soochow University—Zhu Chenghai, Li Jianan, Wang Fudong, Yang Xinhao, Zhao Ying, and Shi Xiaoli—were able to design a ball-and-beam system based on iterative learning control tactics. The team modeled their system using LaGrange equations then used a D-type learning law to increase the performance of the system. These team members are extremely skilled and talented and were able to construct a system that was virtually flawless. While the method that they used to create their system was extremely complicated, it was obvious that it was constructed based on a PD controller [6].

Another team from the Department of Electrical Engineering at Lahore University—Muhammad Asif Rana, Zubir Usman, and Zeeshan Shareef—was able to create a ball-and-beam system using particle swarm optimization. This team tested its method against others, including Ziegler-Nichol, ITAE equations, SISO tool, and fuzzy logic. After testing, they found that the particle swarm optimization algorithm out-performed each of the others. Their controller was made up of two PID controllers contained within the same loop. The particle swarm algorithm was applied at the end to improve performance. The team members did an excellent job in documenting exactly how they implemented their algorithm to tune the gain, thus making it easily understandable by anyone wishing to do the same [7].

A group of scholars from Yangon Technological University—Hla Myo Tun, Myat Su New, and Zaw Min Naing—conducted an experiment in which they designed a compensator for a missile control system using MATLAB Bode plots. This team started with a set of constraints that included steady-state accuracy and phase margin. In this experiment, open-loop and closed-loop frequency responses were compared along with different gain margins, phase margins, bandwidths, and angles. Ultimately, different compensator gains (K) were calculated to achieve the desired results.

This project was also conducted using MATLAB, and the work of these scholars shows an alternate method for achieving similar results [8]. O'Brien and Watkins [2] from the Systems Engineering Department at the U.S. Naval Academy were engaged in a project to design an approach to teaching Bode compensator design. O'Brien and Watkins sought to propose a design approach that would work for a variety of compensators using both root locus and Bode design techniques. They were ultimately able to develop Bode procedures for lead, PI, and PID controllers after starting with just a PD design.

The method that was used by these scholars closely resembled the one used in this current study. The focus of the project was on the design of PD and PID controllers. Due to the fact that root locus compensator design techniques are similar to Bode design techniques, it made sense to teach root locus before Bode. In Bode design, the magnitude and phase of the open-loop frequency response determines how a student moves forward in the approach. By focusing on Bode, students can design for exactly what they want in the beginning and end up with those results. This not only saves time, but allows the student to instead focus on other design problems. These other design problems are tackled later in this paper. The current study is also an extension of the previous work by the authors [9], which also made use of MATLAB simulations. The contribution of this current study was to apply the controllers to a real ball-and-beam system and validate the results of modeling and MATLAB simulation.

## Modeling

Quanser is a company that designs and develops learning platforms for students wishing to learn about control systems [1, 10]. One of the platforms is a ball-and-beam system. This system is comprised of a rotating servo motor along with a ball-and-beam apparatus. The ball-and-beam apparatus consists of a linear position sensor, a beam, and a lever that connects the servo to the beam. A more complete description of the variables can be found in the appendix. When modeling this system, the main objective is finding the transfer function that includes dynamics for all elements in the system. The complete transfer function is equal to the transfer function of the servo motor multiplied by the transfer function of the ball-and-beam system, which is showed in Equation (1):

$$Q(s) = Q_s(s)Q_{bb}(s) \quad (1)$$

The transfer function of the servo motor, where  $Q_s(s)$  is the transfer function of the servo motor, is given in Equation (2):

$$Q_s(s) = \frac{\theta_i(s)}{V(s)} \quad (2)$$

The transfer function from Equation (2) can also be written as shown in Equation (3):

$$Q_s(s) = \frac{K}{s(\tau s + 1)} = \frac{1.53}{s(0.0254s + 1)} \quad (3)$$

$Q_{bb}(s)$ , the transfer function of the ball-and-beam apparatus, is shown in Equation (4):

$$Q_{bb}(s) = \frac{X(s)}{\theta_i(s)} \quad (4)$$

Newton's second law describes how the force of an object is related to its mass multiplied by acceleration. This allows us to come up with Equation (5), which represents the forces acting on the ball. A diagram of the ball-and-beam apparatus is shown in Figure 2.

$$\Sigma F = m_b \left( \frac{d^2}{dt^2} x(t) \right) \quad (5)$$

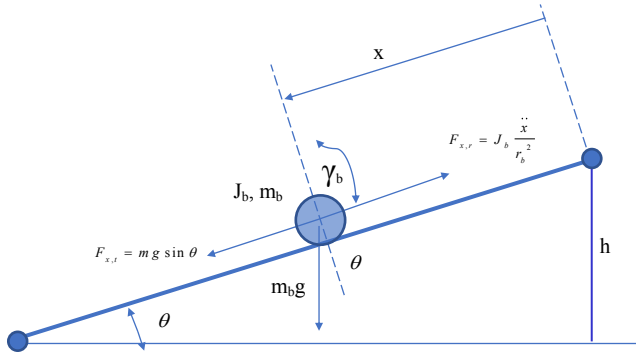


Figure 2. Block Diagram of the Ball-and-Beam Apparatus

After taking all forces into account, Equation (6) is obtained:

$$\frac{d^2}{dt^2} x(t) = \frac{m_b g \sin \theta(t) r_b^2}{m_b r_b^2 + J_b} = f_{x,t} - f_{x,r} \quad (6)$$

It is also important to obtain the relationship between the angle of the beam and the angle of the servo motor. The sine of the beam angle is determined using Equation (7):

$$\sin \theta(t) = \frac{h}{X_{beam}} \quad (7)$$

where,  $h$  is the height of the beam.

The sine of the servo angle is given by Equation (8):

$$\sin \theta_i(t) = \frac{h}{r_{arm}} \quad (8)$$

The relationship between Equations (7) and (8) is shown in Equation (9):

$$\sin \theta(t) = \frac{\sin \theta_i(t) r_{arm}}{X_{beam}} \quad (9)$$

In order to find the equation that relates the motion of the ball to the angle of the servo, the equation must be linearized, as shown in Equation (10):

$$\frac{d^2}{dt^2} x(t) = \frac{m_b g \sin \theta_i(t) r_{arm} r_b^2}{X_{beam} (m_b r_b^2 + J_b)} \quad (10)$$

The next step is to figure out the transfer function that relates the voltage of the motor to the position of the ball. This step is started by taking the Laplace transform of Equation (10), which yields Equations (11) and (12):

$$s^2 X(s) = \theta_i(s) K_{bb} \quad (11)$$

$$Q_{bb}(s) = \frac{K_{bb}}{s^2} \quad (12)$$

According to the Quanser manual [1],

$$\begin{aligned} X_{beam} &= 42.55 \text{ cm} \\ r_{arm} &= 2.54 \text{ cm} \\ r_b &= 1.27 \text{ cm} \\ m_b &= 0.064 \text{ kg} \end{aligned}$$

Using this information, the unknown variables can be obtained using algebra. Equation (13) shows how the gain is calculated:

$$J_b = \frac{2m_b r_b^2}{5} = 4.129 * 10^{-6} \text{ kg} * \text{m}^2 \quad (13)$$

$$K_{bb} = 0.4183$$

Finally, by multiplying Equations (2) and (4), the open-loop transfer function, which relates voltage to ball displacement, of Equation (14) is obtained:

$$\begin{aligned} \left( \frac{\theta_i(s)}{V(s)} \right) \left( \frac{X(s)}{\theta_i(s)} \right) &= \left( \frac{K}{s(\tau s + 1)} \right) \left( \frac{K_{bb}}{s^2} \right) \\ \frac{X(s)}{V(s)} &= \frac{K * K_{bb}}{s^3 (\tau s + 1)} \\ &= \frac{0.64}{s^3 (0.0254s + 1)} \end{aligned} \quad (14)$$



Additional details on the dynamic ball-and-beam system can be obtained directly from Quanser Inc. [10].

## Controller Design

The zeta variable is determined based on the desired amount of overshoot. Zeta can be determined using Equation (15):

$$\zeta = \text{Cos}^{-1} \left\{ \tan^{-1} \left( \frac{-\pi}{\ln(\text{PercentOvershoot} / 100)} \right) \right\} \quad (15)$$

The next step requires the calculation of the phase margin (PM). This calculation is performed using Equation (16):

$$PM = \tan^{-1} \left( \frac{2\zeta}{\sqrt{-2\zeta^2 + \sqrt{1 + 4\zeta^4}}} \right) \quad (16)$$

Next is the determination of the gain crossover frequency. This is accomplished using Equation (17):

$$\omega_{gc} = \frac{8}{T_s \tan(PM)} \quad (17)$$

where,  $T_s$  is the desired settling time.

Equation (18) can now be used to calculate the system's phase of the transfer function:

$$\theta_c = \angle G_c(j\omega_{gc}) = \pm 180^\circ + PM - \angle G_{sys}(j\omega_{gc}) \quad (18)$$

And, Equation (19) gives us the compensator zero location:

$$Z = \frac{\omega_{gc}}{\tan(\theta_c)} \quad (19)$$

In this experiment, the design point,  $s_d$ , was continuous in time and is shown by Equation (20):

$$s_d = j\omega_{gc} \quad (20)$$

The final step is to solve for the magnitude of the control gain,  $K_c$ , determined by Equation (21):

$$K_c = \left( \frac{1}{|G_c(s_d)G_{sys}(s_d)|} \right) \quad (21)$$

Table 1 summarizes all of these steps.

**Table 1. Bode Design Process**

Steps	Description
1	Determine the desired settling time ( $T_s$ ) and percent overshoot (%OS)
2	Calculate the phase margin (PM) and gain crossover frequency ( $\omega_{gc}$ )
3	Calculate the compensator angle ( $\theta_c$ )
4	Evaluate the compensator zero location (Z)
5	Calculate the magnitude of controller gain ( $K_c$ )

In general, Equation (22) defines the PD compensator:

$$PD =: G_c(s) = K_c(s + Z) = K_{p+} K_d s \quad (22)$$

From Equation (22), it is easy to determine the proportional ( $K_p = K_c Z$ ) and proportional derivative ( $K_d = K_c$ ) coefficients for the PD controller.

## Results

Figure 3 shows the block diagram of the overall ball-and-beam system. The goal of this study was to use a Bode PD compensator technique to design a controller for the DC servo motor and the cascade of the closed loop of this ball-and-beam system. The closed-loop design specifications for the ball and bean and the compensated servo system are required to have a settling time of less than 60 seconds and a percent overshoot less than twenty-five.

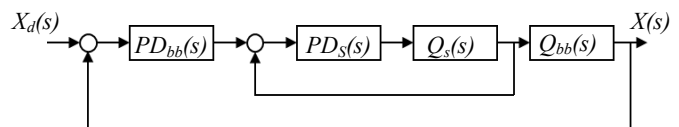


**Figure 3. Block Diagram of PD Compensator**

Figure 4 shows the compensated servo step response. Table 2 shows the results of the PD compensator designed for the servo, based on the calculations from Equation (22) and its validation by applying it to the real system. Figure 4 shows that the settling time was 0.246 seconds, which was extremely fast. There was also only 0.01 percent overshoot for the compensated servo response. Figure 5 shows the uncompensated Bode response of the ball-and-beam system and the desing point that corresponded to the specifications of 2% overshoot and a settling time of 12 seconds. These specifications also corresponded to a phase margin of  $PM = 60^\circ$  and a gain crossover frequency of  $\omega_{gc} = 0.256$

rad/sec, while the uncompensated frequency response of the ball-and-beam system had a phase margin of  $PM = -3.31^\circ$  and a gain crossover frequency of  $\omega_{gc} = 0.647$  rad/sec. Figure 5 shows that the system was unstable.

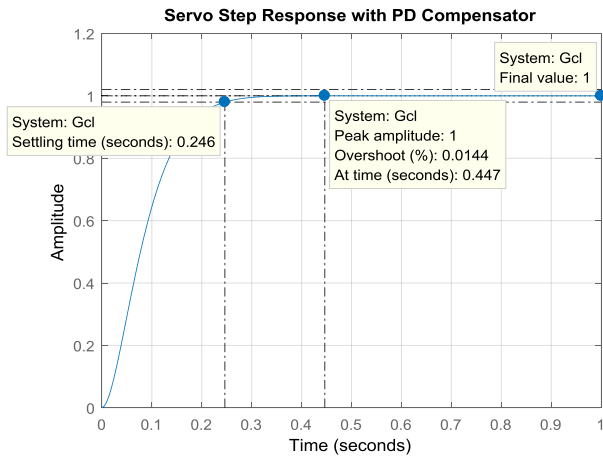


Figure 4. Servo Step Response w/PD Compensator

Table 2. Bode Design PD Gains

Proportional and Derivative (PD) Gain Values		
Parameter	Calculated	Applied to Real System
$K_p$ (servo)	7.3043	7.0
$K_d$ (servo)	0.0027	0
$K_p$ (Ball and Beam)	0.0528	0.1
$K_d$ (Ball and Beam)	0.5761	0.5

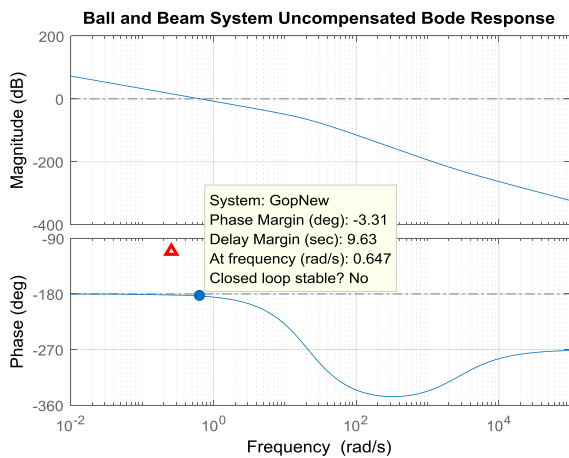


Figure 5. Uncompensated Bode Response of the Ball-and-Beam System

Figure 6 shows the frequency response of a compensated ball-and-beam system. This figure shows how the graph of the frequency response of the system was shifted toward the design point. This tells the reader that the specifications were met and that the closed-loop system was stable.

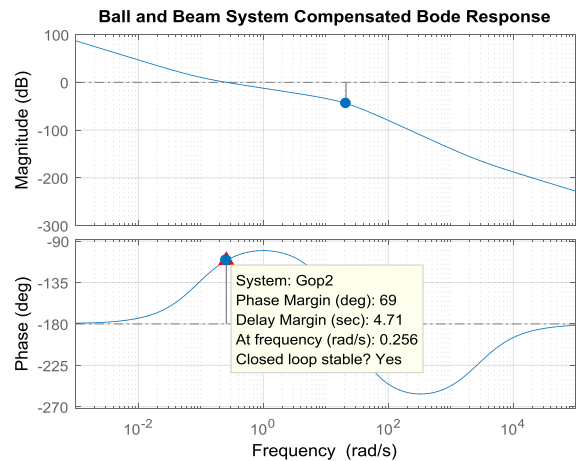


Figure 6. Compensated Bode Response of the Ball-and-Beam System

Figure 7 shows the overall ball-and-beam unit step response after the two PD compensators from Table 2 were applied. There was an 18 percent overshoot. A settling time of 33.9 seconds was able to be achieved. The calculated PD compensator coefficients for these responses are summarized in Table 2.

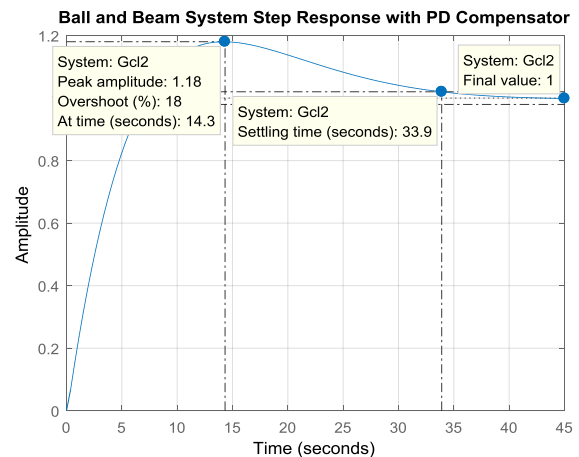


Figure 7. Step Response w/PD Compensator for the Ball-and-Beam System

Figure 8 depicts the result of real-time testing on the actual ball-and-beam control system. It is important to note that the settling time of the actual system was 6.34 seconds. All

so, the real-time response of the system showed that there was no overshoot for the ball on the beam.

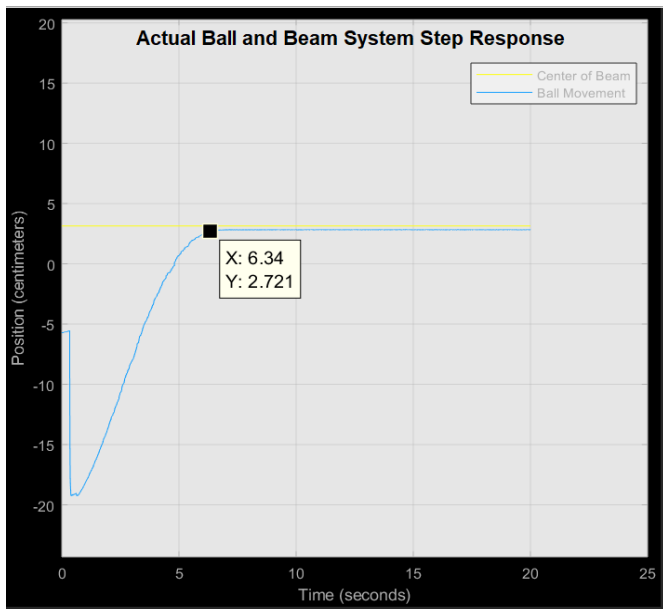


Figure 8. Actual Ball-and-Beam System Step Response

Figures 9 and 10 show us that it is important to take note of the values of proportional gain and derivative gain. These values were determined using the Bode technique.

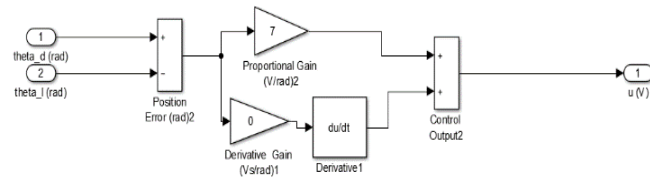


Figure 9. Diagram of the Servo PD Controller in Simulink

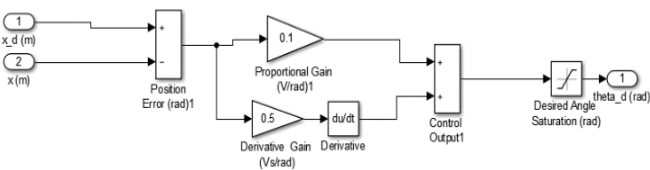


Figure 10. Diagram of the Ball-and-Beam PD Controller in Simulink

The values presented in Table 2 show that the PD gain values were slightly different from the values that were actually used for the real-world simulink experiment. This was due to trial and error. The gain values that were hand calculated, served mostly as a starting point. From there, they were then fine-tuned in order to produce the best response. This explains why the settling time was much faster than the system was originally designed for.

## Conclusions

Two PD compensators were designed using the Bode method for a specific percent overshoot and settling time that also can be associated with a specific phase margin and gain crossover frequency of a ball on a beam. The open-loop frequency magnitude and phase responses of the ball-and-beam system and the overall closed-loop step responses of the system were analyzed to fine-tune the compensator gains. The closed-loop step response performance of the real system was also analyzed. After some fine-tuning, the real-time ball-and-beam system actually performed better than expected.

## Disclaimer

The views expressed in this paper are the personal views of the authors and do not necessarily represent the views of the United States Department of Homeland Security or the United States Coast Guard.

## References

- [1] Quanser Inc. User Manual. (2011). Ball and Beam Experiment Setup and Configuration. Retrieved from [https://my.nps.edu/documents/105873337/0/B01\\_User\\_Manual.pdf/a5687818-5ebf-4d1d-a4ea-f3b96c8516ea](https://my.nps.edu/documents/105873337/0/B01_User_Manual.pdf/a5687818-5ebf-4d1d-a4ea-f3b96c8516ea)
- [2] O'Brien Jr, R. T., & Watkins, J. M. (2003). A Unified Approach for Teaching Root Locus and Bode Compensator Design. *Proceedings of the American Control Conference*, 1, 645-649
- [3] Nise, N. S. (2015). *Control Systems Engineering*. (7th ed.). Wiley.
- [4] United States Coast Guard, Commandant. (2010). Astern Fueling At Sea (AFAS) Procedures Manual. Astern Fueling At Sea (AFAS) M3120.8 ed.
- [5] IMO Takes First Steps to Address Autonomous Ships." Edited by Lee Adamson, International Maritime Organization. Retrieved from [www.imo.org/en/mediacentre/pressbriefings/pages/08-msc-99-mass-scoping.aspx](http://www.imo.org/en/mediacentre/pressbriefings/pages/08-msc-99-mass-scoping.aspx)
- [6] Zhu, C., Li, J., Wang, F., Yang, X., Zhao, Y., & Shi, X. (2016). Design and implementation of Ball and Beam control system based on iterative learning control. *2016 IEEE Advanced Information Management, Communicates, Electronic and Automation Control Conference (IMCEC)*, pp. 128-129). Xi'an.
- [7] Rana, M. A., Usman, Z., & Shareef, Z. (2011). Automatic control of ball and beam system using Particle Swarm Optimization. *12th IEEE International Symposium on Computational Intelligence and Informatics (CINTI)*, (pp. 529-534). Budapest .

- [8] Tun, H. M., Nwe, M. S., & Naing, Z. M. (2008). Design analysis of phase lead compensation for typical laser guided missile control system using MATLAB bode plots. *2008 10th International Conference on Control, Automation, Robotics and Vision*, (pp. 2332-2336) Hanoi.
- [9] Ford, J. K., & Emami, T. (2018). Implementation of a Ball and Beam Control System Using PD Bode Design. *Proceedings of the 2018 ASEE Northeast Section Conference*, Hartford, CT.
- [10] Quanser Inc. Student Workbook. (2011). Ball and Beam Experiment for MATLAB/Simulink Users. Retrieved from [https://my.nps.edu/documents/105873337/0/BB01\\_User\\_Manual.pdf/a5687818-5ebf-4d1d-a4ea-f3b96c8516ea](https://my.nps.edu/documents/105873337/0/BB01_User_Manual.pdf/a5687818-5ebf-4d1d-a4ea-f3b96c8516ea)

## Biographies

**JORDAN FORD** is a marine engineer working in the San Francisco Bay area. He graduated from the U.S. Coast Guard Academy in 2018 with a Bachelor of Science degree in electrical engineering. He is certified by the South Carolina State Board for Professional Engineers and Surveyors as an Engineer in Training. In addition, he holds a Master, 100-Ton Merchant Mariner Credential. Jordan enjoys film making and video editing during his free time, and has accumulated over 1.3 million views on the popular streaming platform YouTube because of this hobby. Ford, a member of the Institute of Electrical and Electronics Engineers, has published two undergraduate research papers on the respective topics of control systems and autonomous swarm robotics. The former of these two papers won him a third place finish out of 30 undergraduate students in the 2018 ASEE Northeast Annual Conference in Hartford, Connecticut. While it is true that Jordan has a wide range of interests that he continues to pursue, he will always be drawn to the field of control systems. Mr. Ford may be reached at [jordankford@gmail.com](mailto:jordankford@gmail.com)

**TOORAN EMAMI** is associate professor of electrical engineering in the Department of Engineering at the U.S. Coast Guard Academy (USCGA). She received her MS and PhD degrees in electrical engineering from Wichita State University (WSU). She taught undergraduate and graduate courses in linear circuits, computer control systems, electric circuits and machines, electrical circuits, applied digital control, introductory control system concepts, and digital control systems at USCGA and WSU. Her research interests include control systems, proportional integral derivative (PID) controllers, robust control, time delay, compensator design for continuous-time and discrete-time systems, and analog or digital filter design. Dr. Emami may be reached at [Tooran.Emami@uscga.edu](mailto:Tooran.Emami@uscga.edu)

## Appendix

**Table 3. Variables and Definitions**

Variables	Definition
$Q(s)$	Combined transfer function of the servo and the ball and beam
$Q_s(s)$	Transfer function of the servo
$Q_{bb}(s)$	Transfer function of the ball and beam
$\theta_f(s)$	Load angle of the servo
$V(s)$	Input voltage of the servo
$K$	Gain of the servo
$\tau$	Time constant of the servo
$X(s)$	Linear displacement of the ball
$m_b$	Mass of the ball
$\Sigma F$	Sum of the forces acting on the ball
$x(t)$	Displacement of the ball
$g$	Gravity
$r_b$	Radius of the ball
$J_b$	Mass moment inertia of the ball
$f_{x,t}$	Translational gravity force
$f_{x,r}$	Force from the ball's inertia
$h$	Height of the beam
$X_{beam}$	Length of the beam
$\theta(t)$	Angle of the beam
$r_{arm}$	Radius of the arm
$K_{bb}$	Gain of the ball and beam
$\zeta$	Damping ratio
$\omega_{gc}$	Gain crossover frequency
$T_s$	Settling time
$PM$	Phase margin
$G_c$	Open-loop transfer function
$G_{sys}$	Closed-loop transfer function
$Z$	Compensator zero location
$sd$	Design point
$\gamma_b$	Angle of the ball
$PD=G_c(s)$	Proportional-derivative compensator

\*Some variables were used in the written MATLAB code.



# OPTIMIZATION OF THE QUICK AND AUTOMATIC SEGMENTATION OF MEDICAL IMAGES BY USING A FUZZY COMBINED METHOD

Shahin Karimi

## Abstract

Today, one of the topics playing a major role in image processing issues, analyzing images, and visualization of a machine is zoning midrange processing. Image zoning plays an essential role in various applications, such as pattern recognition, geographic imaging, remote sensing, and medical imaging. In image segmentation, images are split into discrete regions with homogeneous features. The most important feature used in image segmentation is the color property. In this study, in an analytic-applied field using MATLAB simulations, the author used clustering, fuzzy analysis algorithms, and k-means clustering in two programs on an MRI sample of the human brain and then integrated them into a program. It is worth noting that the images differed according to the coding instruction for ks. The segmentation of an image implies the separation of the image into areas with a specific pixel in each region.

## Introduction

Today, one of the topics playing a major role in image processing issues, analyzing images, and visualization of a machine is zoning midrange processing. Image zoning plays an essential role in various applications, such as pattern recognition, geographic imaging, remote sensing, and medical imaging. In image segmentation, images are split into discrete regions with homogeneous features [1]. Image segmentation refers to the grouping of pixels of an image so that they have similar properties to each other and different properties with the pixels of adjacent pieces. The most important feature used in image segmentation is the color property. In single-color images, the gray level is considered as a feature; but, in color images, different color spaces are used as a color property [2]. Color image segmentation has received more attention lately, as more computing power is available for processing color the images [3]. Among the various characteristics of an image—color, shape, texture, etc.—texture is the most distinctive feature both visually and in terms of image processing. The texture of an image depends on the spatial distribution of the gray-matter values and includes information on contrast, folding, ordering, and the like. Texture analysis offers interesting possibilities for identifying the structural heterogeneity of the

classes. The heterogeneous texture allows for the calculation of the value of pixels within a defined region in the image [4]. Therefore, the use of image texture has become an important aspect in the analysis of high-resolution remote-sensing information.

In medical imaging, zoning is an important stage in medical research and clinical applications. For example, one can imagine and analyze the structures of anatomy, multifocal fusion and recording, pathologic discovery, and surgical planning. The zoning of medical images is difficult, due to tissue heterogeneity, the effects of minor volume, noise, artifacts, and the diversity of various diseases in patients. To solve these problems, the method of formable models was proposed. Extensible models are curves that are defined in the image area and move in the direction of minimizing internal energy functions (causing curve smoothing) and external energy functions (leading the curve toward the desired object's boundary). Despite the significant advances in overlocking models in recent years and the presentation of the versions developed for it, it is still not possible to introduce an active model that inherently has the characteristics of resistance to noise, high speed, the reconstruction of border breaks, and the extraction of weak boundaries. In most medical applications, for solving these problems, area information or previous information has been used in active borderline formulation. But these algorithms are relatively timely and their efficiency is dependent on the initial curves, and the algorithm can fail when the initial curves are chosen inappropriately; user interaction, then, is needed in order to determine the initial areas [5].

Imaging organs in the body helps to diagnose a disease and helps physicians succeed in determining the type of treatment for the patient. The quality of the image taken, the number and dimensions of the images, the speed of transferring images to the doctor, and the type of archiving of images for immediate and subsequent access are all important factors that are considered in medical imaging. With the advent of digital and advanced medical equipment, as well as the trend of the medical sciences to the software movement, many of these problems are diminished and many digital imaging techniques are available, including radiography, ultrasound, and CT scans [6]. Imaging systems, such as magnetic resonance imaging (MRI) and computed to-

mography scanning, have a special place in the detection of tissue abnormalities. Extracting information from these images is an important stage in the processing of medical images, and this stage is the basis for diagnosis and treatment [7]. Processing medical images, especially brain MRI images, often has many complexities, and usually the classic image processing methods alone do not have the required performance in this regard [8]. The use of physician experiences or anatomical information about different tissues of the body can be used as a basis for image processing operations and improve the results of these methods [9]. In this regard, this current study was conducted to investigate the rapid and automatic regionalization of medical images using the SKFCM method.

## Materials and Methods

The segmentation of the image is a very important task in the processing of image and vision. In this current study, a fuzzy clustering method (FCM) is presented. The result of the clustering process is the total membership function, given by Equation (1):

$$\sum_{i=1}^c \mu_{i,k} = 1 \quad (1)$$

where,  $k$  is the number of data.

The sum of the values of the membership functions can be found using Equation (2):

$$\sum_{k=1}^n \mu_{i,k} > 0 \quad (2)$$

## FCM Methods

The standard fuzzy C method is a non-supervised algorithm initially represented by Equation (3) by the FCM target function for image partitioning. Then,  $\{X_k\}_{k=1}^N$ , with  $N$  pixels or voxels in cluster  $c$ , is represented by Equation (4). In this equation, the formula  $\{v_i\}_i^c = 1$  represents clusters  $D_{ik} = \|x_k - v_i\|^2$ , the square of the space between  $v_i$ , the intensity of the pixel  $k(x_k)$ , and the matrix  $[u_{ik}] = U$  denotes the partition matrix  $c \times N$  with  $u \in \mu$ .

$$J_{FCM} = \sum_{i=1}^c \sum_{k=1}^N u_{ik}^m D_{ik} \quad (3)$$

$$\mu = \left\{ u_{ik} \in [0,1] \mid \sum_{i=1}^c u_{ik} = 1 \forall k \wedge 0 < \sum_{K=1}^N U_{ik} < N \forall i \right\} \quad (4)$$

One can interpret the inputs  $u_{ik}$  as the probability that the  $x_k$ , pixel is connected to the  $i$  cluster. This point is referred to as the fuzzy membership. Subscriptions are replicated according to the distance  $D_{ik}$  and according to Equation (5):

$$u_{ik} = \left( \sum_{j=1}^c \left( \frac{D_{ik}}{D_{jk}} \right)^{\frac{2}{m-1}} \right)^{-1} \quad (5)$$

The display of clusters is updated using Equation (6):

$$v_i = \frac{\sum_{k=1}^n u_{ik}^m x_k}{\sum_{k=1}^n u_{ik}^m} \quad (6)$$

The  $m$ -parameter of the rationale is on every fuzzy membership and determines the fuzzy volume of the resulting classification. The algorithm starts with some  $v_i$  views for each cluster and members are updated to reduce the target function of the formula. The modified FCM algorithm was proposed and the modified  $D_{ik}K$  was calculated using Equation (7):

$$D_{ik} = D_{ik} \left( 1 - \alpha \frac{\sum_{j \in neighbors} u_{ij} \cdot p_{kj}}{\sum_j p_{kj}} \right) \quad (7)$$

In this equation,  $\alpha$  is a constant that fulfills the conditions of  $\leq 1 \leq \alpha$ . The formula for pixel approximation  $k$  measures its neighbor pixel  $j$ . Here the approximation is measured by taking into account the relative positions between the two pixels:  $p_{kj} = \|k-j\|_2$ . The change in FCM  $U_{ij}$  is considered as the pixel resistance  $X_K$  against clustering with the  $i$ -handle. Consider  $u_{ij}$  membership numbers for tolerance [see Equation (8)]:

$$J_M = \sum_{I=1}^c \sum_{k=1}^N u_{ik}^m \|x_k - u_i\|^2 + \frac{\infty}{|N_k|} \sum_{i=1}^c \sum_{k=1}^N u_{ik}^m \left( \sum_{x_r \in N_k} \|x_r - v_i\|^2 \right) \quad (8)$$

The two variables FCMS1 and FCMS2 are intend to simplify the calculation of  $J_m$  by replacing the terms

$$\frac{1}{|N_k|} \sum_{x_r \in N_k} \|x_r - v_i\|^2 \quad \text{and} \quad \|x_r - v_i\|^2$$

where, the middle term,  $x'_k$ , for FCMS1 and the mean for FCMS2 are the neighboring pixels in the window surrounding  $x_k$ , as indicated by Equation (9):

$$J_{fcms} = \sum_{i=1}^c \sum_{k=1}^N u_{ik}^m \|x_k - v_i\|^2 \alpha \sum_{i=1}^c \sum_{K=1}^N U_{ik}^M \|x_k - u_i\|^2 \quad (9)$$

## K-Means Method

The k-means method is data clustering in data mining. For this algorithm, there are different shapes, but all of them have a repetitive process. In the k-means algorithm, the k-means ( $k$  is the number of clusters) was randomly selected from  $n$  members as cluster centers. Then, the  $n-k$  remainder is assigned to the nearest cluster. After assigning all members, the cluster centers are recalculated and continuously allocated to the clusters according to the new centers until the cluster centers remain constant. In order to select the best cluster, based on expert opinions and previous studies, a suggested range for the number of clusters was initially identified. Then, the value of  $\rho(k)$  was calculated for each  $k$  value. The value of  $k$ , where  $\rho(k)$  is maximized, was selected as the optimal number of clusters. In this way, the number of clusters was chosen and maximized for the distance between cluster centers and the similarity of cluster centers, when compared to members within each cluster.

## Modeling Results

Figures 1-3 show the output of each of the algorithms, after executing the commands and processing the image. Figure 4 shows the results of the image taken from the output of the k-means algorithm in the FCM algorithm in order to evaluate the more precise clustering operation.

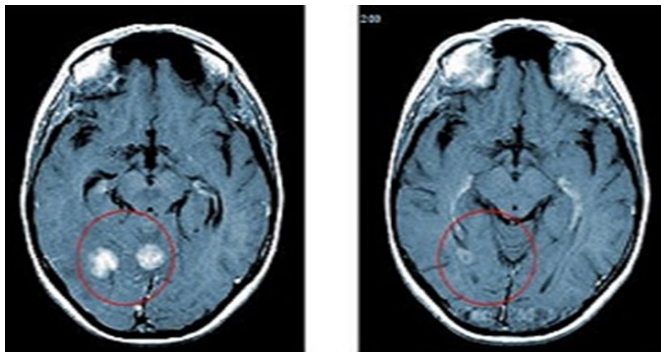


Figure 1. The First Sample of MRI Examined

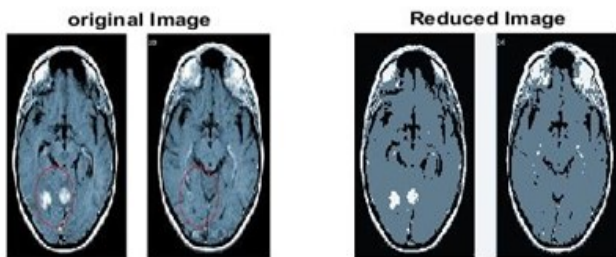


Figure 2. MRI after Processing with the K-Means Algorithm

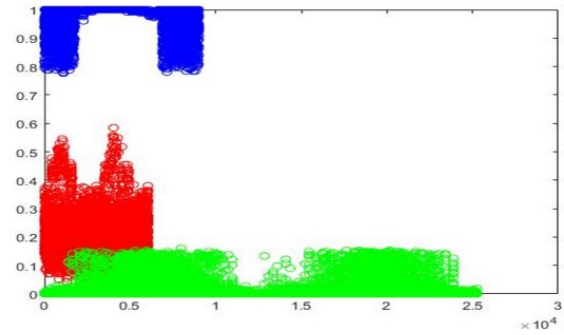


Figure 3. The Output from Processing the First Instance with the FCM Algorithm

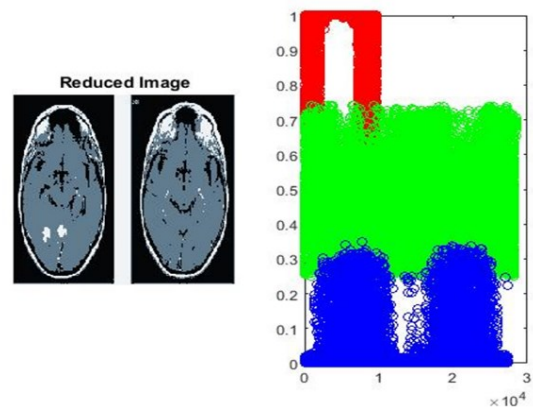


Figure 4. The Sample of the First Image by Both Algorithms

Figure 5 shows the key points of the samples were extracted using the k-means algorithm. Figure 6 indicates the points that can be addressed after processing the probability of occurrence of medical problems.

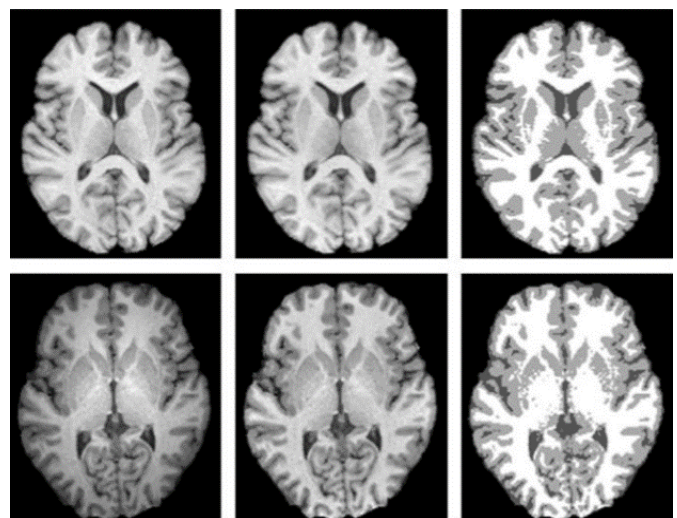
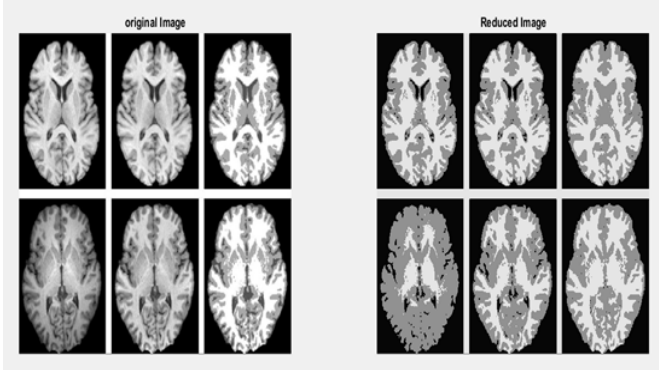
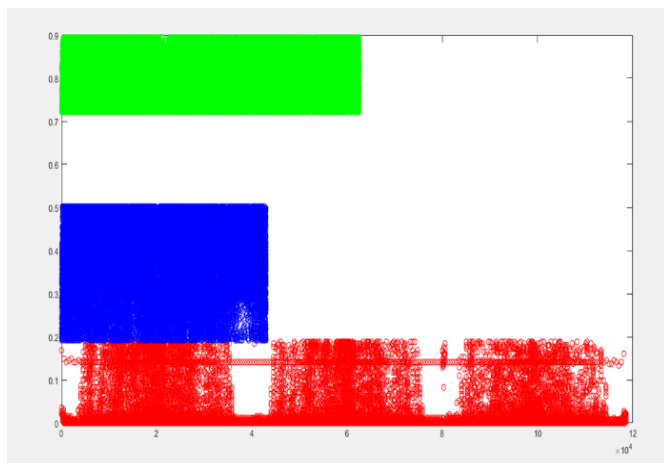


Figure 5. Sample II MRI



**Figure 6. Second Sample MRI after Processing with the K-Means Algorithm**

Figure 7 gives the results of processing the second sample with the FCM and shows that this algorithm yielded more dispersion than other points of the image that were clearly identifiable and detected. Finally, Figure 8 shows how the image taken from the output of the k-means algorithm in the FCM algorithm was also placed on the second sample to evaluate the more precise clustering operations.



**Figure 7. The Output of the Second Sample Resulting from Processing with the FCM Algorithm**

## Discussion and Conclusions

In this study, image processing was used for clustering, and fuzzy analysis algorithms and k-means clustering were initially studied in two separate programs on a human brain MRI sample and then integrated into one program. The most important feature in the segmentation of a single image, the brightness of the image, and the segmentation of a color image, is its color components. Also, the edges of the image and its texture are useful features for segmentation. The results showed that the current approach to different

types of noise and their mixture was stronger and reduced the probability of failure in several cases. Therefore, the convergence criterion, which is always used by the FCM algorithm, does not seem to be sufficient for guaranteeing improvement of the final results in comparison with the initial or medium results.

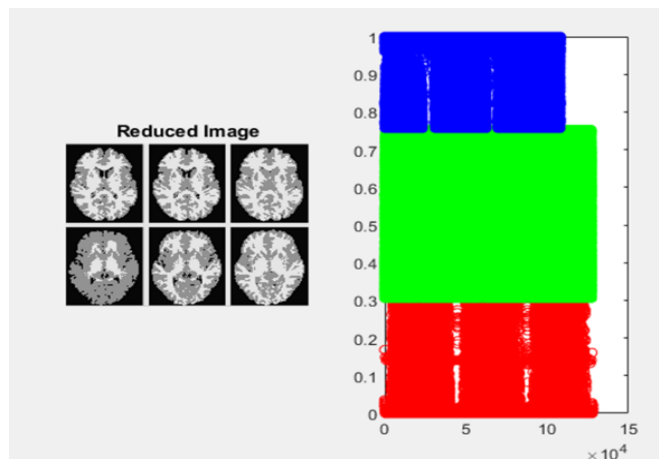


**Figure 8. Sample Image Evaluation of the Second Image by Both Algorithms**

The results of the proposed approach show that even repetition for the first time is enough to make the right decision with high probability. Clustering the input data for a classification algorithm can significantly improve the computational complexity. In this study, the author tried to provide a high-speed, precision clustering algorithm for pre-processing the input data of a classification algorithm. This algorithm also has the ability to deal with uncertainty. In this method, using the combination of k-means and FCM algorithms, image processing was performed. In this case, the k-means algorithm was first implemented on the input data and was able to normalize the distance from each data point to the obtained centers. The same image was then processed as input data were evaluated more precisely by the fuzzy algorithm. This structure may seem simple at first glance, but because its k-means algorithm is one of the suitable algorithms for clustering, it can create a more appropriate membership degree than the random fuzzy algorithm method. This improves FCM speed and ultimately makes this a high-accuracy algorithm for suitable fuzzy clustering algorithms, which increases the speed of the fuzzy clustering algorithm. The results showed that the algorithms were: 1) in the form of extraction of the key points and 2) able to plot the dispersion of the points, where there may be problems and illnesses at the outset. The first picture was displayed in the same way and, with a closer look, it was shown in the second picture that these commands and algorithms yielded the most appropriate output.



---

## References

- [1] Ahmed, M. M., & Mohamad D. B. (2008). Segmentation of Brain MR Images for Tumor Extraction by Combining Kmeans Clustering and Perona-Malik Anisotropic Diffusion Model. *International Journal of Image Processing*, 2(1), 27-34.
- [2] Memaarbashi, E., & Derakhshan, F. (1995). An overview of multifunctional systems-based image segmentation procedures. *First International Conference on the New Achievements of Research in Electrical and Computer Engineering*, Tehran, International Federation of Inventors of the World (IFIA), University of Applied Science and Technology.
- [3] Tabasi, S., & Abdollah Zadeh, F. (2013). The study of effective techniques in medical images segmentation. *First National Conference on Modern Approaches in Computer Engineering and Information Marketing*, Rudsar, Islamic Azad University.
- [4] Jamshidi, O., & Pilevar, A. H. (2013). Automatic Segmentation of Medical Images Using Fuzzy c-Means and the Genetic Algorithm. *Journal of Computational Medicine*, 2013.
- [5] Al-Taie, F., Werner, H. (2015). Structure-preserving model reduction for spatially interconnected systems with experimental validation on an actuated beam. *International Journal of Control*, 89(6), 1248-1268.
- [6] Alizadeh, A., Eshaghi, A., & Abaie, G. (2016). Division of brain lesions in MRI images using watershed algorithms, FCM, K-means and their comparison. *International Conference on Computer and Technology Information Engineering*, Tehran.
- [7] Viergever, J. B., Antoine Maintz, J. B., Klein, S., Murphy, K., Staring, M., & Pluim, P. W. (2016). A survey of medical image registration. *Medical Image Analysis*, 33, 140-144.
- [8] Moroni, S., & Lorini, G. (2017). Graphic rules in planning: A critical exploration of normative drawings starting from zoning maps and form-based codes. *Planning Theory*, 16(3), 318-338.
- [9] Rustaie, S., Bagherzadeh Ajami, N., Ali Dost, H., & Ghaffari, H. N. (1994). A new method for accelerating of medical images segmentation. *International Conference on Applied Researches in Information Technology, Computer and Telecommunications*, Torbat Heydarieh, Khorasan Razavi Province Telecommunication Company.

## Biography

SHAHIN KARIMI may be reached at [karimishahin38@gmail.com](mailto:karimishahin38@gmail.com)

# HYDRATION AND SETTING BEHAVIOR OF CEMENT PASTES MODIFIED WITH SWINE-WASTE BIOCHAR

Andrea Nana Ofori-Boadu, North Carolina Agricultural and Technical State University;  
Frederick Aryeetey, North Carolina Agricultural and Technical State University;  
Zerihun Assefa, North Carolina Agricultural and Technical State University;  
Elham Fini, North Carolina Agricultural and Technical State University

## Abstract

The purpose of this study was to investigate the effect of swine-waste biochar (SB) on the hydration and setting behavior of cement pastes using real-time Fourier Transform Infrared Spectroscopy—Attenuated Total Reflectance (FTIR-ATR) and Raman spectroscopic techniques, as well as the Vicat needle test. Results indicated that SB is not an inert material in cement pastes, as the gradual shifts in the frequencies as well as the intensity changes of characteristic peaks in the Raman and FTIR spectra indicated accelerated polymerization as a result of hydration reactions. In addition to typical cement hydration products (calcium-silicate-hydrate, calcium hydroxide, and calcium-aluminate-sulfate-hydrate), characteristic peaks for calcium-carboxylate-salts (C-C-S) were detected. In all of the SB modified pastes, C-C-S was observed before C-S-H in the FTIR spectra; this explained the lower setting times obtained for SB-modified cement pastes. As early as 15 minutes after water was added to the dry binder mix of ordinary Portland cement with a 20% SB replacement by mass, C-C-S was observed and accelerated the setting of the cement pastes. The shorter setting times of the modified pastes was a result of chemical reactions between the calcium cations from Portland cement and carboxylate anions from SB, leading to the development of C-C-S. The presence of C-C-S also created additional nucleation sites, which accelerated the development of the typical calcium-silicate-hydrates (C-S-H). For acceptable setting times, the highest SB replacement percentage in this research study was 15% at a water/binder ratio of 0.28. Shifts to lower Raman wavelengths for C-S-H in SB-modified pastes provided an indication that C-C-S may have interfered with C-S-H polymerization during the setting period.

## Introduction

The hydration and setting behavior of fresh cement pastes, particularly cement pastes modified with partial cement replacement materials (PCRM), are critical in the development of sustainable structural concrete. The hydration of cement is a complex phenomenon that occurs when water is added to cement. Through dispersion, dissolution, ag-

glomeration, and chemical reactions, the cement pastes transition from a fluid state to a solid state. During early age hydration of ordinary Portland cement (OPC), its four major phases (tricalcium silicate, dicalcium silicates, tricalcium aluminates, and tetracalcium aluminoferrites) move and react with water to form cement paste. Cement paste is a multi-phase product of cement and water. Its complex structure, composition, and morphology vary with time.

Cement pastes consist primarily of calcium hydroxide crystals, aluminates, and unreacted cement particles, all of which are embedded into a product matrix of amorphous nanostructured hydration called calcium-silicate-hydrate (C-S-H) gel [1]. The chemical changes that take place during cement paste hydration often affect the progressive setting of the paste. Setting is the process that occurs and results in a change from an initial semifluid mixture to a solid composite [2]. With the pursuit of more sustainable PCRM, it is widely accepted that the setting and hydration behavior of a PCRM-modified cement paste system should be investigated as part of feasibility studies for PCRM [3]. Consequently, the hydration and setting behavior of cement pastes with biochar obtained from swine-waste was investigated in this study.

The increasing production of swine (hog or pig) in the U.S. has generated environmental concerns, due to disposal challenges associated with swine waste [4-6]. As the environmental consequences of swine waste rise, the pressure to explore methods for processing swine waste for useful applications in the agricultural and construction industry has grown [7]. Bio-binder from swine manure was used in the partial replacement of petroleum-asphalt binder [7]. SB was used to enhance the flow and aging susceptibility of asphalt for more sustainable pavements [8]. Sustainability advocates constantly demand investigations into the use of waste materials in cement to reduce the environmental degradation commonly associated with the production of cement [9]. Considering that raw swine waste has a rather high composition of water and labile elements, using pyrolysis methods to reduce its moisture content and increase its aromatic, stable, and fixed carbons is recommended for cement production processes [10].

Pyrolysis is a key thermochemical conversion process that has been used by several researchers to convert animal waste into three product phases: gases, liquids (bio-oils), and solids (biochar). Biochar production is maximized at temperatures between 350°C and 700°C. Several researchers have focused on biochar sources, pyrolysis temperatures, particle size, density, pH, surface charge, surface function, porosity, water adsorption, cation exchange capacity, and aromatic properties of biochars [11-20]. While biochar has been investigated significantly for soil modification and contamination removal applications, few studies have investigated the use of biochar in cement or concrete applications. Hardwood biochar had water retention benefits, but reduced the compressive strengths of mortars [21]. Swine-waste biochar influenced the flow and setting characteristics of cement pastes with up to 10% SB [20]. No other research studies were found to have conducted investigations on SB-modified cement pastes.

The dominant presence of reactive carboxylic acids, esters, and ethers in biochars present opportunities for chemical interactions to occur between SB and cement [18-20]. Cement research, such as for glass-ionomer cement (GIC), a water-based dental restorative, revealed acid-base reactions between calcium and/or aluminum cations released from reactive glass and carboxyl anions [22-24]. The hypothesis of this research study is that when water is added to a dry blended mix of SB and cement, chemical reactions between the functional surface groups of SB and Portland cement would influence the hydration and setting behavior of cement pastes. Hydration reactions that take place during the early age setting and hardening of cement pastes influence the performance and durability of concrete. As such, the effect of SB on the hydration and setting processes of cement pastes is the focus of this research study as part of the overall assessment of SB's potential as a partial cement replacement material.

The goal of this present study was to monitor, in real-time, the hydration and setting behavior of cement pastes that have been modified with SB as a PCRM. FTIR-ATR, Raman spectroscopy (RS), and Vicat needle tests were used to gain an understanding of the molecular interactions that occur during the early age hydration and setting of cement pastes modified with SB. FTIR and Raman have a history of being used for examining the changes in chemical structures during setting, and the changes to setting chemistry due to the use of additives [24]. Unlike scanning electron microscopy (SEM) and X-ray diffraction (XRD) methods, FTIR-ATR and Raman do not require sophisticated sample preparation, such as drying, vacuuming, and grinding, which destroys the microstructure of the cement paste in the process [2, 24]. In addition, these methods allow continuous and in-

situ observation of the hydration of wet, fresh cement paste [2, 24].

## Experimental Materials and Methods

Type 1/1A Portland cement was obtained from a Home Depot store located in the southeast region of the U.S. Following American Society for Testing Materials (ASTM) guidelines, the cement met the standard composition requirements specified in ASTM-C150. Potable water was from the sink in the Soils Laboratory located on the campus of North Carolina Agriculture and Technical State University (NCA & TSU). SB was produced at the Sustainable Infrastructure Materials (SIM) laboratory located on the campus of NCA & TSU. SB is a black, carbonaceous residue from a thermochemical process (340°C for 80 minutes with nitrogen gas) used to extract bio-oil from raw swine waste through a pyrolysis process [7, 8]. SB was the residue obtained after filter paper was used to separate SB from bio-oil. Table 1 presents the elemental composition of SB [20]. Zetasizer Nano-S (Malvern instrument) dynamic light scattering (DLS) showed that SB's mean particle size was 509.6 nm and SB had negatively charged surfaces.

**Table 1. Elemental Composition of SB**

Element	Percent	Element	Percent
Carbon	54.02	Phosphorus	4.87
Oxygen	30.60	Silicon	0.95
Calcium	5.00	Iron	0.90
Magnesium	1.95	Aluminum	0.34

Following the mix proportions for the SB-modified cement pastes listed in Table 2, cement and SB were manually dry mixed for about five minutes to obtain a uniform binder mix. Potable water was placed in the mixing bowl of a 4.73 liter ELE mechanical mortar mixer (ASTM C305 compliant). The dry cement/SB binder mix was then added and allowed to sit for 30 seconds for water absorption. The mechanical mixer was started at a slow speed (139 rpm) and then mixed for 30 seconds. The mixer was then stopped for 15 seconds and the sides of the mixing bowl were scrapped. The mixer was re-started and the paste was mixed at medium speed (285 rpm) for 60 seconds. The specimens were then immediately extracted for the Vicat setting tests.

For the FTIR and Raman spectroscopic analysis, cement and SB were manually dry mixed in a small plastic dish using the mix proportions listed in Table 2. Mixing water was then added to the dry ordinary Portland cement / SB binder mix and allowed to soak for 30 seconds for water

absorption. It was then manually mixed for another 60 seconds. The specimens were then extracted for FTIR and Raman tests. Shifts in characteristic peaks in the FTIR and Raman spectra were used to gain insight into ongoing hydration reactions that were in progress during the setting of cement pastes.

**Table 2. Mix Proportions for SB-Modified Cement Pastes**

Design Mix	Cement (%)	SB (%)	Water /Binder Ratio
CP-SB00	100.00	0.00	0.28
CP-SB10	90.00	10.00	0.28
CP-SB15	85.00	15.00	0.28
CP-SB20	80.00	20.00	0.28

FTIR was used to obtain useful information regarding the development of key hydration products in SB-modified cement pastes. FTIR has been used extensively as a semi-quantitative method to investigate cement, biochar, and composites [1, 25-36]. FTIR analysis was conducted with a Varian 670 FTIR spectrometer using a Pike “miracle” Attenuated Total Reflectance (ATR) accessory for an attenuated total internal reflection FTIR. In an ambient atmosphere, the background spectrum was collected before sample analysis. Sixteen scans were recorded over the measurement range between  $400\text{ cm}^{-1}$  and  $4000\text{ cm}^{-1}$ , with a spectral resolution of  $4\text{ cm}^{-1}$ . The obtained spectra were corrected with a linear baseline.

Raman spectroscopy (RS) has been used to obtain useful information regarding SB, cement, and the development of hydration products in SB-modified cement pastes [2, 37-50]. The Horiba XploRA One Raman Confocal microscope system allowed the generation of Raman spectra for cement, SB, and all cement pastes. The instrument used a laser, which interacted with sample molecules and resulted in energy of laser photons being shifted up or down. This Raman shift was measured in wavelengths and unique energy shifts of each molecule enhanced its detection. During each test, scanning was carried out from  $150\text{ cm}^{-1}$  to  $3500\text{ cm}^{-1}$ . Samples were illuminated with a 532-nm laser. The exposure time for each scan was 10 seconds, and about one minute was used to acquire each spectrum.

The spectra were corrected using a linear baseline. Given the continual shifts in frequencies and change in intensity of characteristic peaks in the FTIR and Raman spectra, the cement pastes were used to track and gain insight into ongoing hydration reactions that occurred during the setting of the cement pastes. American Society for Testing and Materials (ASTM C191) guidelines for the time of setting of hy-

draulic cement by the Vicat needle were followed to determine the initial setting times as well as the final setting times of all cement pastes. The initial time of setting was recorded when a needle penetration of 25 mm was attained. Final setting was achieved when there was no complete circular penetration on the cement paste.

## Early Hydration Products Detected by the FTIR-ATR

In agreement with previous studies, research results showed FTIR characteristics peaks (see Figure 1), which confirmed the presence of O-H ( $3200\text{--}3600$ ), C-H ( $2915\text{ cm}^{-1}$ ,  $2850\text{ cm}^{-1}$ ), C=C and C=O ( $1500\text{--}1750\text{ cm}^{-1}$ ), and C-O ( $1000\text{--}1300\text{ cm}^{-1}$ ) surface functional groups for reactive carboxylic acids, esters, and ethers in SB-modified cement pastes [18-20]. NMR studies yielded similar results and found similar functional groups in SB [11]. Also, the characteristic peaks for silicates ( $916\text{ cm}^{-1}$ ,  $875\text{ cm}^{-1}$ ), sulfates ( $1124\text{ cm}^{-1}$ ), and carbonates ( $1405\text{ cm}^{-1}$ ) from Portland cement were observed [1, 20, 26-28].

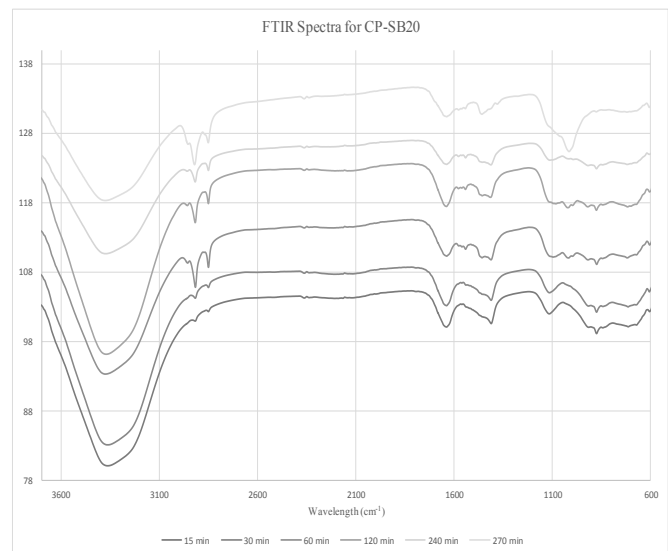


**Figure 1. FTIR Spectra for CP-SB20 at Varying Ages**

**Capillary water:** While the dry cement and SB had limited water bands at  $3360\text{ cm}^{-1}$ , the 15-minute spectra in Figure 1 showed that the most dominant feature in the FTIR spectra for CP-SB20 was the strong O-H stretch ( $3360\text{ cm}^{-1}$ ). This corresponded to capillary water as the mixing water had been added only 15 minutes previously to the binder mix and had not fully participated in the hydration process. The negligible differences in the stretches during the first hour of hydration of CP-SB20 were a result of  $\text{-OH}$  groups participating in hydrogen bonding, indicating the incorporation of more water molecules in the system [1]. The capillary

water facilitates the hydration process by dissolving the cement minerals and contributing hydroxyl ions for the formation of hydroxyl groups. With the addition of water, the cement dissolves and calcium ions from calcium silicates leach quickly from the cement into the mixing water. Deprotonation of carboxylic acid groups also occurred. As hydration proceeded, the water was consumed in various hydration reactions, as observed in a reduction in the intensity of the O-H stretch in the 270-minute spectra for CP-SB20. The stretch maximizing at  $1633\text{ cm}^{-1}$  for CP-SB20 was also assigned to the stretching and bending modes of water in sulfates, particularly gypsum [27, 30]. As hydration progressed, this broad feature was caused by the bending vibration of irregularly bound water [25]. Also, the  $1633\text{ cm}^{-1}$  stretch in the SB modified pastes was associated with C=O and C=C bonds for carboxylic acids and aromatic alkenes from SB [20, 30-33].

**Calcium-aluminate-sulfate-hydrate:** Prior to the addition of water, the bend at  $1124\text{ cm}^{-1}$  in the spectra for dry cement was assigned to S-O stretching for sulfates in cement [25, 47]. In Figure 1, the 15-minute spectra for CP-SB20 shows that, with the addition of water, there was a shift to a lower peak ( $1105\text{ cm}^{-1}$ ). This was assigned to S-O stretching of  $\text{SO}_4^{2-}$  in the development of calcium-aluminate-sulfate-hydrate (ettringite), which is known to form early in the cement hydration process [1, 27, 47]. With the addition of water, the rapid dissolution of sulfates was followed by crystallization [25]. Changes occurring within this sulfate area are not uncommon, as intermediate phases are formed and ettringite subsequently changes to monosulfate as the hydration progresses [1, 25].

**Calcium-carboxylate-salts (C-C-S):** The earliest appearance of C-C-S was observed as weak bends on the FTIR spectra ( $1459\text{ cm}^{-1}$  and  $1538\text{ cm}^{-1}$ ) as early as 15 minutes after water was added to CP-SB20. The weak bends became more distinct and strengthened with time as hydration progressed. Therefore, the more developed bends, as shown in the 60-minute spectra for CP-SB20, are typically for the salts of carboxylic acids [34, 35]. The weak peaks observed at  $1538\text{ cm}^{-1}$  and  $1575\text{ cm}^{-1}$  in the 60-minute spectra were assigned to carboxylate groups at multi-layer coverage in precipitated C-C-S. [51]. Figure 1 shows how this doublet became more distinct with time, as hydration progressed and the stretches for capillary water ( $3360\text{ cm}^{-1}$ ) and carboxyl groups ( $1633\text{ cm}^{-1}$ ) appeared to decrease in intensity.

This is because, with the addition of mixing water to the dry cement/SB mix, the carboxylic acids (-COOH) found in SB readily dissociated into carboxylate anions with the release of hydrogen ions (deprotonation). This resulted in the increased dominance of carboxylate anions (COO-) in the

pastes. Concurrently, there was a release of calcium cations from cement, and these made capillary water become an aqueous mix with a variety of ions. Calcium cations from cement replaced the hydrogen deprotonated from the carboxylic acids and resulted in the development of calcium-carboxylate-salts (C-C-S). The emergence of more distinctive peaks at  $1459\text{ cm}^{-1}$ ,  $1538\text{ cm}^{-1}$ , and  $1575\text{ cm}^{-1}$  in the 270-minute spectra for CP-SB20 confirmed that these acid-base reactions continued to make significant progress within the SB-modified cement pastes. The small changes in the shape of these bands are associated with the structural and conformation changes that occur as the calcium cations replace hydrogen ions in the polymer chain. The FTIR doublet at  $1540\text{ cm}^{-1}$  and  $1575\text{ cm}^{-1}$  are correlated to the coordinated structure of carboxylate groups with calcium ions [51]. The presence of C-C-S was further validated with the emergence of weak stretches at  $1031\text{ cm}^{-1}$  in the 60-minute spectra for CP-SB20 and this was assigned to C-O bonds in C-C-S.

This bend for C-O bonds in C-C-S intensified as hydration progressed, as shown in the 270-minute spectra. Furthermore, the stretches for C-H bonds ( $2915\text{ cm}^{-1}$  and  $2850\text{ cm}^{-1}$ ) for alkyl groups in CP-SB20 became more dominant as hydration progressed, being most dominant in the 270-minute spectra for CP-SB20. This was attributed to the fact that the mixing water was continuously consumed during the cement paste hydration reactions, and so the decrease in capillary water permitted easier detection of the C-H bonds by the FTIR equipment. Notably, Figure 2 shows that the stretches ( $2915\text{ cm}^{-1}$ ,  $2850\text{ cm}^{-1}$ ,  $1575\text{ cm}^{-1}$ ,  $1538\text{ cm}^{-1}$ ,  $1454\text{ cm}^{-1}$ , and  $1031\text{ cm}^{-1}$ ) for C-C-S in CP-SB20 were absent in the control cement paste (CP-SB00), because it had no SB and, as such, no functional organic surface groups. C-C-S bands were most intense in CP-SB20 because it had the highest SB content.

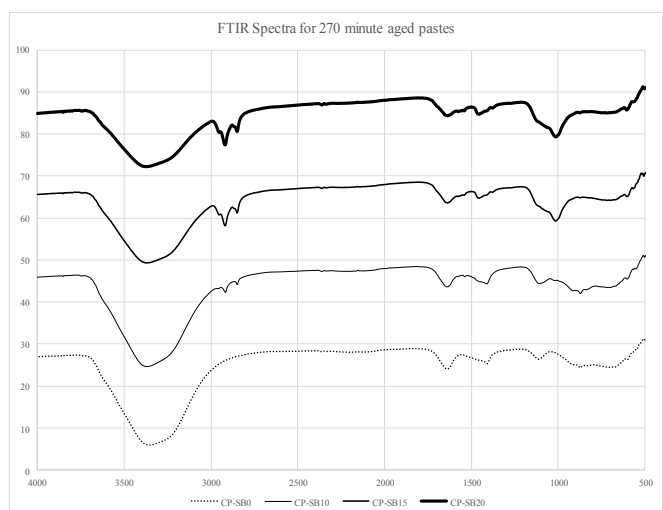


**Figure 2. FTIR Spectra for 270-Minute Aged Pastes**



**Calcium-silicate-hydrate:** The typical key hydrate responsible for strength development, C-S-H, was not detected early but emerged later in the 270-minute spectra for CP-SB20 (see Figure 1). The appearance of a slight shoulder ( $995\text{ cm}^{-1}$ ) as a result of the shift from the undissolved cement peak ( $916\text{ cm}^{-1}$ ) was attributed to the polymerization of silicate units ( $\text{SiO}_4^{4-}$ ) with formation of the C-S-H phase [1]. It is not uncommon for C-S-H to be detected three hours after hydration when the outer product of the C-S-H gel has surrounded the cement grains [52]. Figure 2 shows that even after 270 minutes of hydration, the shift for C-S-H polymerization had not yet occurred in the control paste (CP-SB00), nor in the paste with the least amount of SB (CP-SB10).

Rather, the Si-O asymmetric stretching vibration of undissolved calcium silicates ( $910\text{ cm}^{-1}$ ) in Portland cement were still present in CP-SB00 and CP-SB10 [1]. Clinker (undissolved calcium silicates in cement) dissolution has been correlated with C-S-H formation [25]. Notably, these clinker bands almost completely disappeared in the 270-minute spectra for CP-SB15 and CP-SB20, suggesting that perhaps clinker consumption progressed at a much higher rate in SB-modified cement pastes. This observation suggests that SB may also have created additional nucleation sites for the development of C-S-H, thus accelerating the polymerization of C-S-H in SB-modified cement pastes. Predictably, C-S-H developed and matured on the calcium silicate particles, while calcium hydroxide crystals grew in the pore space [53]. With the presence of SB in the pore space, C-S-H is likely to also grow and SB and further accelerate the polymerization of C-S-H.

**Calcium hydroxide:** FTIR stretches for calcium hydroxide (CH) were not observed in any of the 270-minute spectra in this study. However, CH was observed at  $3637\text{ cm}^{-1}$  in all of the 7-day pastes (see Figure 3). During the dissolution of the calcium silicate phases in cement, chemical reactions between OH- and calcium cations from cement resulted in the precipitation of CH. [27, 28].

### Early Hydration Products Detected by Raman

In agreement with the FTIR results, Figure 4 for the Raman spectra indicates the presence of C-C ( $955\text{ cm}^{-1}$ ,  $770\text{ cm}^{-1}$ ), C-COO ( $1574\text{ cm}^{-1}$ ,  $875\text{ cm}^{-1}$ ), and C-H ( $1474\text{ cm}^{-1}$ ,  $1353\text{ cm}^{-1}$ ) functional surface groups [44-46]. Peaks for aluminates ( $761\text{ cm}^{-1}$ ,  $525\text{ cm}^{-1}$ ), calcium silicates ( $849\text{ cm}^{-1}$ ), gypsum ( $1016\text{ cm}^{-1}$ ), and carbonates ( $1098\text{ cm}^{-1}$ ) were observed in the Raman spectra for ordinary Portland cement [2, 37, 38, 42, 43].

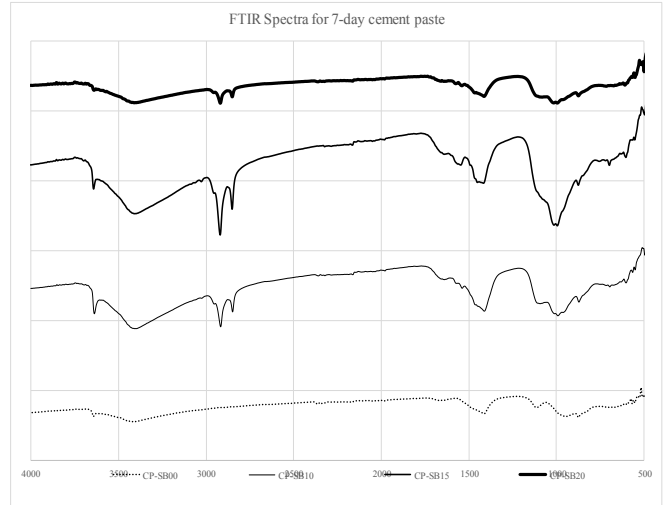


Figure 3. FTIR Spectra for 7-Day Aged Pastes

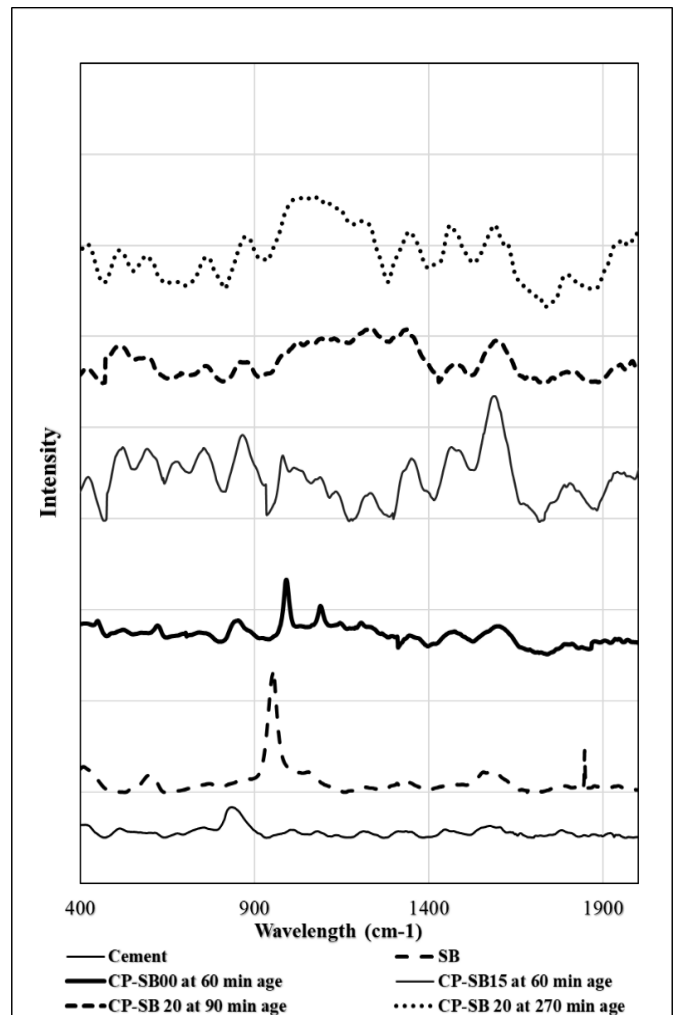


Figure 4. RAMAN Spectra for Cement, SB, and Pastes

In agreement with the results from the FTIR, the Raman spectra (see Figure 4) confirmed that SB is not inert, and that chemical reactions occur when water is added to SB-modified cement. The spectra obtained support the fact that four key hydration products are formed with the addition of water: calcium-carboxylate salts, calcium-silicate-hydrate, calcium-aluminate-sulfate-hydrate, and calcium hydroxide.

**Calcium-carboxylate-salts (C-C-S):** After 60 minutes, the most dominant peaks during the setting of cement pastes modified with SB were for C-H ( $1469\text{ cm}^{-1}$ ,  $1357\text{ cm}^{-1}$  and  $1089\text{ cm}^{-1}$ ) and  $\text{COO}^-$  ( $1598\text{ cm}^{-1}$  and  $880\text{ cm}^{-1}$ ) in C-C-S in CP-SB15 and CP-SB20 (see Figure 4). An increase in the intensities of the CP-SB20 peaks ( $1338\text{ cm}^{-1}$ ,  $1455\text{ cm}^{-1}$ , and  $1582\text{ cm}^{-1}$ ) corresponding to progressive increments in C-C-S was noted when the 90-minute spectra for CP-SB20 were compared with the 270-minute spectra. Furthermore, on the 270-minute spectra, a peak emerged at  $1629\text{ cm}^{-1}$ . This peak was possibly due to aluminum-carboxylate-salts (A-C-S) [45]. Aluminum cations from the dissolution of tricalcium aluminates in cement may have reacted with the carboxylate anions from SB to form A-C-S.

**Calcium-silicate-hydrate (C-S-H):** The peaks observed at  $460\text{ cm}^{-1}$  and  $625\text{ cm}^{-1}$  in CP-SB00 were assigned to polymerized C-S-H from the hydration of calcium silicates in cement; while in CP-SB15 and CP-SB20, the peaks at  $430\text{ cm}^{-1}$  and  $600\text{ cm}^{-1}$  were assigned to polymerized C-S-H [2, 39, 41, 43]. This shift to a lower Raman frequency for C-S-H was consistently observed in all of the other SB-modified cement pastes. The lower C-S-H peaks in the SB-modified pastes may be attributed to changes in the bond length and strength of C-S-H, as a result of the earlier development of C-C-S in the SB-modified cement pastes [50]. These findings provided strong evidence that indicated that C-C-S from SB had intruded in the growth and maturation of C-S-H, and perhaps weakened the linkages and microstructural development of C-S-H in the cement pastes modified with SB. Additional research should be conducted to assess the extent to which such interference in the development of C-S-H would hinder strength development in concrete. Furthermore, the C-S-H peaks in the SB-modified pastes appear to be more intense, suggesting that perhaps C-S-H had developed much faster in the SB-modified pastes compared to the control paste. This may be explained by the additional nucleation sites created by SC that allowed C-S-H to develop much faster in the SB-modified cement pastes [54].

**Calcium-aluminate-sulfate-hydrate:** The peaks at  $987\text{ cm}^{-1}$  in SB-modified pastes and  $995\text{ cm}^{-1}$  in CP-SB00 were assigned to ettringite [47]. Once again, the lower Raman shifts for the hydrates in the SB-modified cement pastes was at-

tributed to the interference from C-C-S. Unhydrated calcium silicates were also observed by the peaks at  $519\text{ cm}^{-1}$  and  $854\text{ cm}^{-1}$  in both pastes.

**Calcium hydroxide:** Two peaks ( $1483\text{ cm}^{-1}$  and  $1613\text{ cm}^{-1}$ ) were assigned to calcium hydroxide in the control pastes [2]. These Raman peaks were masked by the C-C-S peaks in the cement pastes modified with SB.

## Setting Times of Cement Pastes by the Vicat Needle Test

Concurrent with results from the spectroscopic techniques, results from the Vicat needle time-of-setting test (see Figure 5) showed that the replacement of 20% of ordinary Portland cement with SB in CP-SB20 resulted in an 88% reduction in the initial setting time. Considering that the ASTM standard requires initial setting times to be at least 45 minutes, the results obtained for CP-SB20 do not satisfactorily meet performance prescriptions, as the SB-modified cement paste set too quickly [55]. It is important that chemical reactions occur sufficiently slowly initially to allow adequate mixing and working time for the pouring, working and finishing of concrete. Consequently, at a 0.28 water/binder ratio, SB replacement percentage should not exceed 15%.

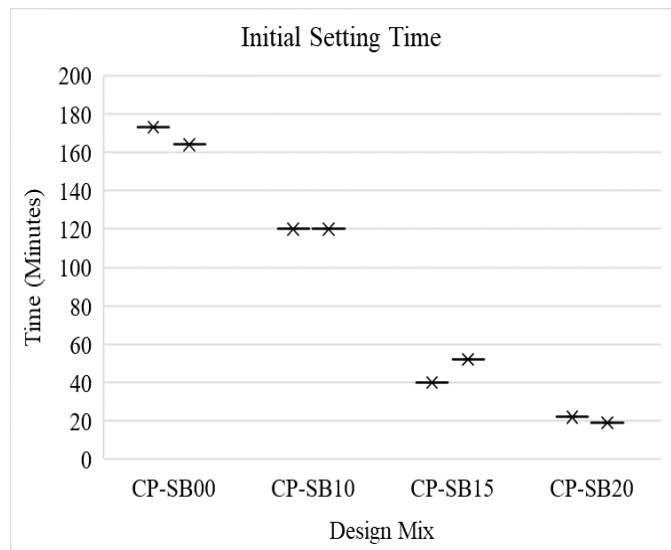


**Figure 5. Initial Setting Time for Cement Pastes**

Compared to CP-SB00, an 80% reduction in the final time of setting was obtained when 20% of ordinary Portland cement was replaced with SB in CP-SB20 (see Figure 6). Drawing from the FTIR and Raman results, the rapid setting of SB-modified cement pastes was primarily attributed to the early and rapid precipitation of C-C-S.

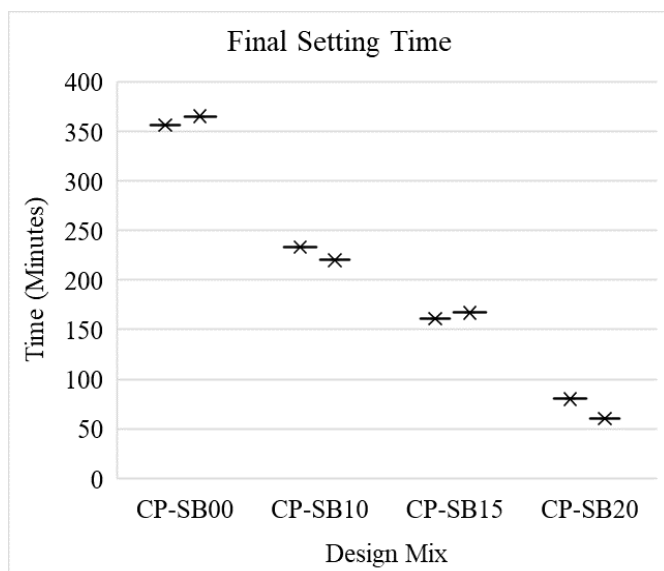


**Figure 6. Final Setting Time for Cement Pastes**

These results indicate that, during the typical inactive induction period of the control cement pastes (CP-SB00), C-C-S in cement pastes modified with SB continues to develop and mature. Furthermore, the presence of SB in pastes provides additional nucleation sites in the pore spaces, and this advances the accelerated development and setting of the hydration products. [49]. These additional nucleation sites resulted in faster interactions and linkages among the different hydrated products, thus accelerating the setting of SB-modified cement pastes.

The influence of SB on the hydration and setting of cement pastes cannot be overlooked. SB first disperses non-uniformly in the cement paste. After that, reactive carboxylic acid functional surface groups from the swine diets present in SB react with calcium ions from cement through acid-base reactions to form C-C-S [20, 56-59]. Concurrently, other key Portland cement hydration products were developed. As hydration proceeds and the capillary water is consumed, C-C-S and these other key Portland cement hydrated products coalesce to form a solid paste.

## Conclusions

In this research study, real-time spectroscopic techniques and ASTM Vicat needle setting-time tests were used to investigate the effect of swine-waste biochar on the hydration and setting behavior of cement pastes. The following conclusions can be drawn from this study:

1. Swine-waste biochar is not a passive material, as reactive negatively charged carboxylic acid functional surface groups are present in SB. When mixing

water was added to the dry cement/SB binder mix, chemical reactions occurred between the calcium silicates of ordinary Portland cement and the carboxylic functional surface groups of SB. Consequently, in addition to the typical cement hydration products (calcium-silicate-hydrate, calcium-aluminate-sulfate-hydrate, calcium hydroxide), calcium-carboxylate-salts (C-C-S) were observed in SB-modified pastes.

2. Compared to the much later detection of calcium-silicate-hydrate (C-S-H) and calcium hydroxide (CH), C-C-S was observed as early as 15 minutes in SB-modified paste with 20% SB. The spectroscopic shift for polymerizing silica for C-S-H was 270 minutes after the addition of water to the dry cement/SB binder mix for cement pastes with 20% SB.
3. The shorter initial and final times of setting obtained for SB-modified cement pastes corroborated the early observation of C-C-S in the FTIR spectra. This provided strong logical evidence to confirm that C-C-S had accelerated the setting and development of cement pastes modified with SB. Furthermore, it is suspected that SB also contributed additional seeding sites within the cement pastes to support the growth of hydrated products, and this also contributed to the accelerated setting of the SB pastes.
4. SB interfered in C-S-H development in SB-modified cement pastes, as was indicated by the lower Raman shifts that were obtained for C-S-H in all SB-modified cement pastes. Considering that C-C-S precipitated and polymerized much earlier than C-S-H in SB-modified pastes, it is plausible that C-C-S structures may have been formed prior to the delayed emergence of C-S-H, and this could have negatively impacted the microstructural development and polymerization of C-S-H.
5. Under the experimental conditions in this study, the cement pastes that had been modified with 20% SB had unacceptably short initial setting times. Consequently, the maximum SB replacement percentage with acceptable setting times was 15%.

## References

- [1] Bhat, P. A., & Debnath, N. C. (2011). Theoretical and experimental study of structures and properties of cement paste: The nanostructural aspects of C-S-H. *Journal of Physics and Chemistry of Solids*, 72, 920-933.
- [2] Liu, F., Sun Z., & Qi, C. (2015). Raman spectroscopy study on the hydration behaviors of Portland cement pastes during setting. *Journal of Materials in Civil Engineering*, 27(8). 04014223-1- 04014223-9.

- [3] Pacewska, B., & Wilińska, I. (2013). Hydration of Cement Composites Containing Large Amount of Waste Materials. *Procedia Engineering*, 57, 53-62.
- [4] U.S. Department of Agriculture. (2017a). Estimated Weekly Meat Production under Federal Inspection. Retrieved from [https://www.ams.usda.gov/mnreports/sj\\_ls712.txt](https://www.ams.usda.gov/mnreports/sj_ls712.txt)
- [5] U.S. Department of Agriculture. (2017b). National Agricultural Statistics Service Meat Animals–Production by year (Hogs). Retrieved from <https://quickstats.nass.usda.gov/results/9218C92C-F6BC-39DB-94DF-C6DE05E2BDA0>
- [6] U.S. Government Accountability Office. (2008). Concentrated Animal Feeding Operations: EPA Needs More Information and a Clearly Defined Strategy to Protect Air and Water Quality from Pollutants of Concern. GAO-08-944 (September 2008).
- [7] Fini, E. H., Kalberer, E. W., Shahbazi, A., Basti, M., You, Z., Ozer, H., et al. (2011). Chemical characterization of biobinder from swine manure: sustainable modifier for asphalt binder. *Journal of Materials in Civil Engineering*, 23(11), 1506-1513.
- [8] Walters, R. C., Fini, E. H., & Abu-Lebdeh, T. (2014). Enhancing asphalt rheological behavior and aging susceptibility using biochar and nano-clay. *American Journal of Engineering and Applied Sciences*, 7(1), 66-76.
- [9] World Business Council for Sustainable Development. (2009). The cement sustainability initiative. Retrieved from <http://www.wbcscement.org/pdf/CSI-RecyclingConcrete-FullReport.pdf>
- [10] Brewer, C. E. (2012). *Biochar characterization and engineering*. PhD dissertation for Iowa State University, Ames, IA.
- [11] Cao, X., Ro, K. S., Chappell, M. Li, Y., & Mao, J. (2011). Chemical structures of swine-manure chars produced under different carbonization conditions investigated by advanced solid-state C Nuclear Magnetic Resonance (NMR) spectroscopy. *Energy Fuels*, 25, 388-397.
- [12] Cantrell, K. B. P., Hunt, G., Uchimiya, M., Novak, J. M., & Ro, K. S. (2012). Impact of pyrolysis temperature and manure source on physiochemical characteristics of biochar. *Bioresource Technology*, 107, 419-428.
- [13] Mukherjee, A., Zimmerman, A. R., & Harris, W. (2011). Surface chemistry variations among a series of laboratory-produced biochars. *Geoderma*, 163, 247-255.
- [14] Gray, M., Johnson, M. G., Dragila, M. I., & Kleber, M. (2014). Water uptake in biochars: The roles of porosity and hydrophobicity. *Biomass and Bioenergy*, 61, 196-205.
- [15] Jindo, K., Mizumoto, H., Sawada, Y., Sanchez-Monedero, M. A., & Sonoki, T. (2014). Physical and chemical characterization of biochars derived from different agricultural residues. *Biogeosciences*, 11, 6613-6621.
- [16] Herbert, L., Hosek, I., & Kripalani, R. (2012). The characterization and comparison of biochar produced from a decentralized reactor using forced air and natural draft pyrolysis. Retrieved from [digitalcommons.calpoly.edu/cgi/viewcontent.cgi?article=1047&context=matesp](http://digitalcommons.calpoly.edu/cgi/viewcontent.cgi?article=1047&context=matesp)
- [17] Tsai, W.-T., Liu, S.-C., Chen, H.-R., Chang, Y.-M., & Tsai, Y.-L. (2012). Textural and chemical properties of swine-manure-derived biochar pertinent to its potential use as a soil amendment. *Chemosphere*, 89, 198-203.
- [18] Yakout, S. M. (2015). Monitoring the Changes of Chemical Properties of Rice Straw–Derived Biochars Modified by Different Oxidizing Agents and Their Adsorptive Performance for Organics. *Bioremediation Journal*, 19(2), 171-182.
- [19] Ghidotti, M., Fabbri, D., Mašek, O., Mackay, C. L., Montalti, M., & Hornung, A. (2017). Source and Biological Response of Biochar Organic Compounds Released into Water; Relationships with Bio-Oil Composition and Carbonization Degree. *Environmental Science & Technology*, 51(11), 6580-6589.
- [20] Ofori-Boadu, A. N., Kelley, R., Aryeetey, F., Abutalib, N., Fini, E., & Akangah, P. (2017). The Influence of Swine-waste Biochar on the Early-age Characteristics of Cement Pastes. *International Journal of Engineering Research and Applications*, 7(6), 1-7.
- [21] Choi, W. C., Yun, H. D., & Lee, J. Y. (2012). Mechanical properties of mortar containing bio-char from pyrolysis. *Journal of the Korea Institute for Structural Maintenance and Inspection*, 16(3), 67-74.
- [22] Tu, X.-M., Sun, B.-H., & Ran, J.-G. (2016). Preparation of sol-gel method and evaluation of lanthanum-containing filling glass ionomer cement powder. *Materials Letters*, 183, 236-239.
- [23] Weng, Y., Howard, L., & Xie, D. (2014). A novel star-shaped poly(carboxylic acid) for resin-modified glass-ionomer restoratives. *Journal of Biomaterials Science, Polymer Edition*, 25(10), 1076-1090.
- [24] Valliant, E. M., Dickey, B. T., Price, R., Boyd, D., & Filiaggi, M. J. (2016). Fourier transform infrared spectroscopy as a tool to study the setting reaction in glass-ionomer cements. *Materials Letters*, 185, 256-259.
- [25] Ylmen, R., Jaglid, U., Brit-Marie, S., & Panas, I. (2009). Early hydration and setting of Portland cement monitored by IR, SEM and Vicat techniques. *Cement and Concrete Research*, 39, 433-439.

- [26] Ylmen, E. R. (2013). Early hydration of Portland Cement. PhD dissertation, Chalmers University of Technology, Gothenburg, Sweden.
- [27] Horgnies, M., Chen, J. J., & Bouillon, C. (2013). Overview of the use of Fourier Transform Infrared Spectroscopy to study cementitious materials. *WIT Transactions on Engineering Sciences*, 77, 251-262.
- [28] Govindarajan, D., & Gopalakrishnan, R. (2011). Spectroscopic studies on Indian Portland cement hydrated with distilled water and sea water. *Frontiers in Science*, 1(1), 21-27.
- [29] Fernández-Carrasco, L., Torrén-Martín, D., Morales, L. M., & Martínez-Ramírez, S. (2012). Infrared spectroscopy in the analysis of building and construction materials. Theophile Theophanides (Ed.), *Infrared Spectroscopy—Materials Science, Engineering and Technology*, INTECH, 369-382.
- [30] Chia, C. H., Gong, B., Josepha, S. D., Marjo, C. E., Munroea, P., & Rich, A. M. (2012). Imaging of mineral-enriched biochar by FTIR, Raman and SEM-EDX. *Vibrational Spectroscopy*, 62, 248-257.
- [31] Segneanu, A. E., Gozescu, I., Dabici, A., Sfirloaga, P., & Szabadaí, Z. (2012). Organic Compounds FT-IR Spectroscopy. *National Institute for Research and Development in Electrochemistry and Condensed Matter, Timisoara (INCEMC-Timisoara) Romania*.
- [32] Volland, W. (1999). Organic compound identification using infrared spectroscopy. Retrieved from <http://www.800mainstreet.com/irsp/eir.html>
- [33] University of California. (2014). Infrared Spectroscopy Absorption Table. Retrieved from [https://chem.libretexts.org/Reference/Reference\\_Tables/Spectroscopic\\_Parameters/Infrared\\_Spectroscopy\\_Absorption\\_Table](https://chem.libretexts.org/Reference/Reference_Tables/Spectroscopic_Parameters/Infrared_Spectroscopy_Absorption_Table)
- [34] Khashaba, R. M., Moussa, M., Koch, C., Jurgensen, A. R., Missimer, D. M., Rutherford, R. L., et al. (2011). Preparation, Physical-Chemical Characterization, and Cytocompatibility of Polymeric Calcium Phosphate Cements. *International Journal of Biomaterials*, 1-13.
- [35] Dickey, B., Price, R., & Boyd, D. (2016). Evidence of a complex species controlling the setting reaction of glass ionomer cements. *Dental Materials*, 32, 596-605.
- [36] Sidhu, S. K., & Nicholson, J. W. (2016). A review of glass-ionomer cements for clinical dentistry. *Journal of Functional Biomaterials*, 7(16), 1-15.
- [37] Potgieter-Vermaak, S. S., Potgieter, J. H., & Grieken, R. V. (2006). The application of Raman Spectrometry to investigate and characterize cement, Part I: A review. *Cement and Concrete Research*, 36, 656-662.
- [38] Bensted, H. (1976). Use of Raman spectroscopy in cement chemistry. *Journal of American Ceramics Society*, 59(3-4), 140-143.
- [39] Cholleta, M., & Horgnies, M. (2011). Analyses of the surfaces of concrete by Raman and FT-IR spectroscopies: comparative study of hardened samples after demolding and after organic post-treatment." *Surface and Interface Analysis*, 43, 714-725.
- [40] Torrén-Martín, D., Fernández-Carrasco, L., & Martínez-Ramírez, S. (2013). Hydration of calcium aluminates and calcium sulfoaluminate studied by Raman spectroscopy. *Cement and Concrete Research*, 47, 43-50.
- [41] Tarrida, M., Madon, M., Rolland, B. L., & Colombet, P. (1995). An in-situ Raman spectroscopy study of the hydration of tricalcium silicate. *Advanced Cement Based Materials*, 2(1), 15-20.
- [42] Gandolfi, M. G., Van Landuyt, K., Taddei, P., Modena, E., & Garg, N. (2012). *Raman spectroscopy for characterizing and determining the pozzolanic reactivity of fly ashes*. PhD dissertation for Iowa State University, Ames, Iowa.
- [43] Peskova, S., Machovic, V., & Prochazka, P. P. (2011). Raman spectroscopy structural study of fired concrete. *Ceramics – Silikaty*, 55, 410-417.
- [44] University of Toronto Scarborough. (2017). Raman band correlation table. Retrieved from <http://www.utoronto.ca/~traceslab/raman%20correlation%20table.pdf>
- [45] Young, A. M., Sherpa, A., Pearson, G., Schottlander, B., & Waters, D. N. (2000). Use of Raman spectroscopy in the characterization of the acid base reaction in glass-ionomer cement. *Biomaterials*, 21, 1971-1979.
- [46] Baran'skaa, M., Chruszcza, K., Boduszekb, B., & Proniewiczza, L. W. (2003). FT-IR and FT-Raman study of selected pyridinephosphonocarboxylic acids. *Vibrational Spectroscopy*, 31, 295-311.
- [47] Renaudin, G., Segni, R., Mentel, D., Nedelec, J.-M., Leroux, F., & Taviot-Gueho, C. (2007). A Raman study of the sulfated cement hydrates: Ettringite and Monosulfoaluminate. *Journal of Advanced Concrete Technology*, 5(3), 299-312.
- [48] Van Meerbeek, B., & Prati, C. (2010). Environmental scanning electron microscopy connected with energy dispersive x-ray analysis and Raman techniques to study ProRoot mineral trioxide aggregate and calcium silicate cements in wet conditions and in real time. *Journal of Endodontics*, 36(5), 851-857.
- [49] Martínez-Ramírez, S., & Fernández-Carrasco, L. (2011). Raman Spectroscopy: Application to cementitious systems. *Construction and Building: Design, Materials, and Techniques*. Retrieved from



<https://upcommons.upc.edu/bitstream/handle/2117/11758/Construction%20building%20design%20materials%20and%20techniques.pdf>

- [50] Hardcastle, F. D., & Wachs, I. E. (1991). Determination of niobium-oxygen bond distances and bond orders by Raman spectroscopy. *Solid State Ionics*, 45, 201-213.
- [51] Lu, Y., & Miller, J. D. (2002). Carboxyl stretching vibrations of spontaneously adsorbed and LB-transferred calcium carboxylates as determined by FTIR internal reflection spectroscopy. *Journal of Colloid and Interface Science*, 256, 41-52.
- [52] Taylor, H. F. W. (1997). *Cement chemistry*. (2nd Ed.). Thomas Telford Publishers, London.
- [53] Pignat, C., Navi, P., & Scrivener, K. (2005). Simulation of cement paste microstructure hydration, pore space characterization, and permeability determination. *Materials and Structures*, 38, 459-466.
- [54] Thomas, J. J., Jennings, H. M., & Chen, J. J. (2009). Influence of Nucleation Seeding on the Hydration Mechanisms of Tricalcium Silicate and Cement. *J. Phys. Chem*, 113(11), 4327-4334.
- [55] ASTM (2013a). ASTM C150/C150M-17 Standard Specification for Portland Cement. ASTM International, West Conshohocken, PA. Retrieved from [www.astm.org](http://www.astm.org)
- [56] Shannon, M. C., & Alee, G. L. (2005). Protein and amino acid sources for swine diets. National Swine Nutrition Guide. Retrieved from <http://porkgateway.org/wpcontent/uploads/2015/07/protien-and-amino-acid-sources-for-swine1.pdf>
- [57] Wang, R., Li, J., Zhang, T., & Czarnecki, L. (2016). Chemical Interaction between Polymer and Cement in Polymer-Cement Concrete. *Bulletin of the Polish Academy of Sciences-Technical Sciences*, 64(4), 785-791.
- [58] Tian, Y., Jin, X., Jin, Y., Zhou, R., Li, Z., & Ma, H. (2013). Research on the microstructure formation of polyacrylate latex modified mortars, *Journal of Construction and Building Materials*, 47, 1381-1394.
- [59] Ofori-Boadu, A. N., Abrokwah, R., Gbewonyo, S., & Fini, E. (2018). Effect of Swine-waste Bio-Char Treatment Temperatures on Water Absorption Characteristics of Cement Pastes. *International Journal of Building Pathology and Adaptation*, 36(2). [IN-PRESS]

## Biographies

**ANDREA N. OFORI-BOADU** is an assistant professor with the Department of Built Environment, North Carolina Agricultural and Technical State University (NCATSU). She earned her BS degree from the University of Science

and Technology, Ghana (Building Technology, 1997). In 2004, she earned her MS (Industrial Technology) degree from North Carolina Agricultural and Technical State University. Her PhD (Technology Management, 2012) was from Indiana State University. Dr. Ofori-Boadu's research interests include bio-modified cements, quality management of sustainable buildings, and STEM education. Overall, Dr. Ofori-Boadu's research work has resulted in one book, 12 publications in peer-reviewed journals, five conference proceedings, and 29 presentations at national conferences. Dr. Ofori-Boadu is the Director of the STEM ACTIVATED! program for middle-school girls of STEM promise. She has received several grants to support her research work. In 2017, Andrea received the Rookie Research Excellence Award for North Carolina A&T State University. Dr. Ofori-Boadu is affiliated with ATMAE, NAWIC, ASC, ASEE, and NAHB. Dr. Ofori-Boadu may be reached at [andrea@ncat.edu](mailto:andrea@ncat.edu)

**FREDERICK ARYEETEEY** is a PhD student at the Joint School of Nanoscience and Nanoengineering, North Carolina Agricultural and Technical State University (NCATSU). He earned his bachelor's degree from the University of Ghana, Legon (Computer Science and Physics, 2009). In 2012, he earned his MS (Physics) degree from North Carolina Central University. In 2015, he earned another MS (Applied Physics) degree from the University of Massachusetts, Lowell. Frederick Aryeetey's research interests include characterization techniques such as SEM, TEM, AFM, PHOTOLUMINESCENCE, EFM (electrical force microscopy), HIM (helium ion microscope) and X-ray photoelectron spectroscopy. He is experienced in cleanroom fabrication and thin-film deposition techniques such as dry etching, photolithography, alpha step meter, rapid thermo annealer, chemical vapor deposition, and physical vapor deposition. Mr. Aryeetey may be reached at [farveete@aggies.ncat.edu](mailto:farveete@aggies.ncat.edu)

**ZERIHUN ASSEFA** is a professor of chemistry at North Carolina Agricultural and Technical State University. He earned his BSc degree (chemistry) from Addis Ababa University in Ethiopia and his PhD (inorganic chemistry) in 1992 from the University of Maine. After post-doctoral experiences at Texas A&M and Auburn Universities, Dr. Assefa joined the Oak Ridge National Laboratory and worked as a staff scientist for ten years before moving to his current institution. Dr. Assefa is actively pursuing fundamental research on materials for luminescent sensors, white-light emitting materials, gold-based compounds for possible medicinal applications, as well as STEM education. Dr. Assefa has over 75 peer-reviewed publications and three book chapters. Dr. Assefa may be reached at [zassefa@ncat.edu](mailto:zassefa@ncat.edu)

---

**ELHAM H. FINI** is an associate professor with the Department of Civil, Architectural, and Environmental Engineering, North Carolina Agricultural and Technical State University (NCATSU). She earned her BS degree from the Isfahan University of Technology, Isfahan, Iran (Civil Engineering, 2000). In 2003, she earned her MS (Civil Engineering) degree from Sharif University of Technology, Tehran, Iran. Her PhD (Civil Engineering, 2008) was from the University of Illinois at Urbana-Champaign. Dr. Fini is co-founder of Bio-Adhesive Alliance Inc., and director of the sustainable infrastructure materials lab, and a Fulbright Scholar from North Carolina A&T State University. She has been a research affiliate at MIT's Center for Materials Science and Engineering since 2011. Dr. Fini may be reached at [efini@ncat.edu](mailto:efini@ncat.edu)

# DESIGN AND FABRICATION OF A SAMARIUM SELECTIVE POTENTIOMETRIC SENSOR USING KRYPTOFIX 22DD IN A POLYMER MATRIX MEMBRANE

Neshat Majd, Islamic Azad University, Iran; Arezoo Ghaemi, Ferdowsi University of Mashhad, Iran

## Abstract

In this study, the authors designed and fabricated a coated graphite ion-selective electrode sensitive to samarium cation based on the neutral ion of Kryptofix 22DD in a membrane made of polyvinyl chloride (PVC) in tetrahydrofuran (THF). The best function was achieved with a membrane containing 0.05 mg of Kryptofix 22DD, 0.2 mg sodium tetraphenyl borate (NaTPB), 0.63 mg nitrobenzene (NB), and 30.0 mg PVC. This electrode, with a high selectivity compared to  $\text{Sm}^{3+}$  cation, had a Nernst slope of  $91.7 \pm 0.1$  mV/decade in the linear range of  $1.0 \times 10^{-1}$  M to  $1.0 \times 10^{-7}$  M, and a detection limit of  $9.3 \times 10^{-8}$  M. The proposed sensor had a fast response time of 10 seconds and good repeatability, and was used for a 50-day period without significant potential changes. The electrode was used within the pH range of 2-10 and the effect of possible interaction ions on it was investigated. This electrode was used as a detector electrode for potentiometric titration of samarium using NaI and EDTA solutions, and a sharp defect was observed in the titration curves around the equivalence point. This sensor was successfully used to determine  $\text{Sm}^{3+}$  in samples of double-distilled water with different concentrations of samarium. The sensor was also used to determine the samarium in real samples of water.

## Introduction

The focus on crown ether compounds since 1967 was begun by Pedersen with the synthesis of the first crown ether (Dibenzo-18-crown-6). Crown ethers are the large cyclic compounds in which there are heteroatoms such as oxygen, nitrogen, or sulfur. These ligands are also sometimes called multidentate macrocyclic or macroheterocycles [1]. Crown compounds are neutral; heteroatoms in the ring play the role of electron donor and create strong crown-cation and crown-anion complexes. One of the most prominent features of the crown compounds is their complexity with metal cations, especially alkali metal cations and alkaline earth metals, which gives particular importance to these compounds [2]. Crown ethers are the unladen molecules that are often separated from the oxygen donor atoms in the ring by methylene groups, usually two methylene groups ( $-\text{CH}_2-\text{CH}_2-$ ). The ability to form a stable complex, espe-

cially alkaline and alkaline earth metals cations, is one of the most important characteristics of the crown compounds, especially the crown ethers [3]. Generally, the formation of the complex between the crown ether and cation is due to dipolar ionic electrostatic interactions of the C-O bond and the cation. The stronger the interactions, the more sustained complexes naturally occur. Figure 1 shows the complex formation reaction between cations  $\text{K}^+$  and 21-crown-7.

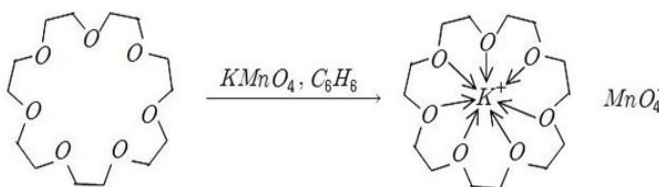


Figure 1. Complex Formation Reaction between Cations  $\text{K}^+$  and 21-crown-7

In the structure of the crowns, the pair of free electrons of the oxygen atoms orientates to the interior, so strong interactions between the cation and the ligand are established, which results in the creation of a coordination space, either partially or completely in the ring. On the other hand, Methylene is directed to the outside of the ring; this behavior gives the lipophilicity property to the complex and solves the complex in non-polar solvents (see Figure 2) [4].

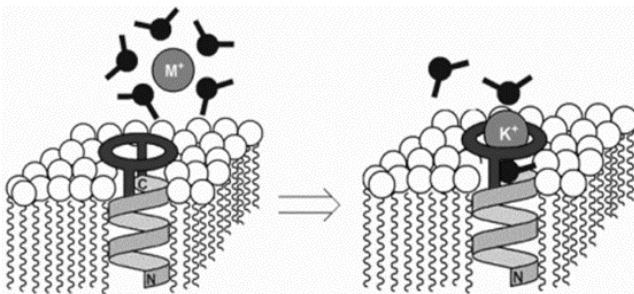


Figure 2. Strong Interactions between Cations and Ligands

The relative size of the cation and ligand cavity, the effect of the solvent, the effect of anion, the number of donor atoms and the spatial arrangement of crown ether, the type of donor atoms in the crown ring, the cation load, the effect of fraction groups in the crown ring, and the strength of the ligand play, are factors that affect the stability of crown

---

ether complexes [5]. Selection and detection of ions, increasing the dissolution capacity of mineral salts in organic solvents as a stationary phase in HPLC, preparation of ion-selective electrodes, and transfer of ions from biological membranes and as phase transfer catalysts are the most important applications of crown ether; therefore, it is necessary to study each of them. Samarium was discovered in 1879 in France by Paul Emil. The name of this element was taken from the word samarskite (a mineral material). Its applications include [6]:

- Concentration of  $\text{CaF}_2$  crystals for use in Excimer lasers
- Use as a neutron absorber in nuclear reactors
- Used in alloys and headphones
- Samarium-cobalt alloys for permanent high-strength magnets
- Samarium oxide in optical glass for absorbing infrared radiation
- Certain compounds of samarium as phosphorus sensitizer
- Samarium oxide as a catalyst for reducing water and dehydrogenation of ethanol

The presence of samarium in the workplace is dangerous, because when its gas is inhaled with air causes lung blockage, especially if it is inhaled over an extended time period. In addition, samarium causes cancer in humans and inhaling it increases the risk of cancer [7]. Of course, it should be noted that polymer membrane-based sensors are used as an efficient analytical tool with many advantages to measure various ions in biological and environmental samples [8]. Contamination with heavy metals is one of the major environmental problems in human societies that endanger the health of people in the community. Manufacturing sensors using a simple process, and creating sensors that have a high lifecycle, low cost, and high sensitivity and selectivity is important for measuring the small amounts of analyte. In this project, the large ligand of the Kryptofix 22DD (1, 10-didecyl-1, 10-diaza-18-crown-6) was used in the production of graphite-coated electrodes, which are sensitive to samarium, in order to measure this metal in aqueous solutions.

## Methodology

### Method for Preparing the Solutions

The solutions used in this study were prepared from solutions in the range of  $1.0 \times 10^{-8}$  to  $1.0 \times 10^{-1}$  molar from samarium nitrate. In order to prepare 0.1 molar of nitrate samarium solution, 2223.2g of six high-purity samarium nitrate salt was poured into a 50-ml volumetric flask with distilled water. To prepare a 0.01-molar solution of samarium nitrate,

5 ml of the 0.1 molar nitrate samarium solution was poured into a 50-ml volumetric flask with distilled water. In the way, other solutions were prepared from the initial solution. For preparation of a 0.13-molar EDTA solution, according to the calculations, 0.930g of high-purity EDTA- $\text{Na}_2$  salt were weighed and placed in a 25 ml volumetric flask and with distilled water. To prepare a 0.01M NaI solution, according to the calculations, 0.750g of sodium iodide salt with high purity was poured into a 50 ml volumetric flask and with distilled water. Prior to the preparation of 4 ppm and 8 ppm mixtures of samarium, a solution of 1000 ppm samarium was prepared. For this purpose, 29.556g of high-purity samarium nitrate was poured into a 100 ml volumetric flask and with distilled water. A 100 ppm solution was prepared from this 1000 ppm solution. To prepare 4 ppm solutions and 2 ppm solutions, 2 and 4 ml of solution of 100 ppm samarium were poured into a 50 ml volumetric flask and with distilled water, respectively.

The preparation method of an ion-selective electrode for measuring samarium began with graphite rods having a diameter of 4 mm. The rods were first placed in a concentrated nitric acid solution for 24 hours to remove their impurities. Next, the bars were washed with THF and water. Then they were washed with soft sandpaper to form a perfectly uniform surface, and then washed again with distilled water and acetone and dried at room temperature. To prepare the membrane, proper amounts of polyvinyl chloride (PVC), ion-selective Kryptofix 22DD, softener (DBP, DOP, DOS and NB), and additive (NaTPB) were placed in dried Bécher 10 ml, then about 2 ml of THF was added to this mixture and quickly mixed with a manual whisk until a completely uniform solution was obtained. This solution was then mixed with a magnetic stirrer to create a viscous solution (thick and oily) suitable for coating on a graphite rod. The next step was to use dip the tip of the graphite rod into the above solution for several seconds and up to a certain height to form a uniform membrane on the rod. The prepared electrode was placed at room temperature for 24 hours to evaporate the solvent and dry the membrane.

After the construction of the electrode, and in order to condition and use it in the potentiometric measurements, the electrode was first placed in a solution of 0.02 molar measured ions for a specific time to place the cation in the ion-selective pores and the membrane in the coating layer. The ion-selective pores were then gradually saturated with the ions in the solution. Next, the electrode was washed with distilled water and used for dissolution measuring. After connecting the ion-selective electrodes by copper wire along with the silver chloride reference electrode to the potentiometer in the Bécher containing the measured solution, the potential difference between the two electrodes was meas-

ured. To measure the potential, a series of solutions containing the desired ion was prepared for a concentration range of  $1.0 \times 10^{-8}$  to  $1.0 \times 10^{-1}$  molar. To measure the potential of each solution, they were given a certain period of time to allow the membrane covering the surface of the electrode to be balanced with the measured solution and then the potential was read. Finally, the E (mV) diagram was drawn in accordance with  $-\text{Log} [\text{Sm}^{3+}]$  of the electrodes and their response (slope and domain of linear concentration) were investigated.

## Results and Discussion

Table 1 shows the results of the investigation into the composition of membrane components on the response of ion-selective electrode sensitivity to samarium cation. Sensitivity, selectivity, linear concentration range, and stability of an ion-selective electrode depend not only on the nature of the ion-selective electrode used, but also on the nature and amount of softener and lipophilic material [9]. Four different types of softeners (DOP, DBP, DOS, and NB)

were used to study the effect of the softener on the response of the coated samarium-selective electrode.

The results show that the electrodes, using NB as a softener in membranes, had a wider range of linear concentrations. Lipophilic additives have numerous effects on the membrane of ion-selective electrodes, which reduces the membrane's resistance and improves the Nernst response and selectivity of the electrode [10, 11]. Sodium tetra phenyl borate (NaTPB) was used to study the effect of the additive on the response of the coated electrode sensitivity to samarium. The results showed that, in the absence of NaTPB, the slope of the electrode differed from the Nernst slope; but, as NaTPB increased, the electrode response got nearer to the Nernst response. The amount of ion selectivity in the membrane also played a key role in the performance of the electrode, because the amount of these particles affects the amount of available space for the formation of the complex between the cation of samarium and ion selectivity. Table 1 shows that the absence of ion selectivity causes an undesirable response in the electrode; but, with its increase, the electrode response is desirable.

**Table 1. Optimization of Membrane Components in Creation of a Samarium-Selective Electrode**

No.	Composition of the membrane components (mg)					Linear concentration range (M)
	PVC	Ion selective (Kryptofix22DD)	Additive (NaTPB)	Softener	Slope (mV / decade)	
1	30	7.0	-	(NB) 0.63	61.2±7.0	$10^{-7}$ to $10^{-2}$
2	30	-	7.0	(NB) 0.63	1.2±0.3	$10^{-7}$ to $10^{-2}$
3	30	5.0	2.0	(DOP)0.63	32.6±0.5	$10^{-5}$ to $10^{-1}$
4	30	6.0	3.0	(DOP) 0.61	81.8±0.3	$10^{-5}$ to $10^{-1}$
5	30	5.0	2.0	(NB)0.63	91.7±0.1	$10^{-7}$ to $10^{-1}$
6	30	4.0	4.0	(DOP) 0.62	62.4±0.6	$10^{-4}$ to $10^{-1}$
7	30	5.0	2.0	(DBP)0.63	71.2±0.1	$10^{-6}$ to $10^{-2}$
8	30	4.0	4.0	(DBP) 0.61	61.8±0.8	$10^{-5}$ to $10^{-1}$
9	30	3.5	2.5	(DBP) 0.64	51.8±0.5	$10^{-4}$ to $10^{-2}$
10	30	5.5	2.5	(DBP)0.62	71.5±0.2	$10^{-8}$ to $10^{-5}$
11	30	6.0	2.0	(DOS) 0.62	11.8±0.5	$10^{-7}$ to $10^{-4}$
12	30	5.0	2.0	(DOS) 0.63	41.9±0.6	$10^{-5}$ to $10^{-2}$
13	30	5.0	4.0	(DOS) 0.61	71.6±0.4	$10^{-5}$ to $10^{-2}$
14	30	3.0	2.0	(NB)0.65	12.2±0.7	$10^{-6}$ to $10^{-1}$
15	30	5.0	3.0	(NB) 0.62	31.9±0.2	$10^{-6}$ to $10^{-2}$
16	30	6.0	4.0	(DBP) 0.60	51.9±0.5	$10^{-4}$ to $10^{-1}$



## Response Curve of the Samarium-Selective Electrode Combined with the Optimal Components of the Membrane

The results of the study showed that the linear concentration range was equal to  $1.0 \times 10^{-7}$  to  $1.0 \times 10^{-1}$  M. Figure 3 shows that the slope of the calibration curve in this concentration region was 19.7 mV/decade (the equation of line  $R^2=0.926$ ,  $y=19.714x+240.71$ ). The slope of the curve was closer to the Nernst slope, indicating better response and sensitivity of electrode. The detection limit in the ion-selective electrons (see Figure 4), according to IUPAC recommendations, was obtained from the intersection of the two extrapolated lines from the calibration curve [12]. According to this method, the detection limit of the coated graphite samarium-selective electrodes was obtained at  $9.3 \times 10^{-8}$  M.

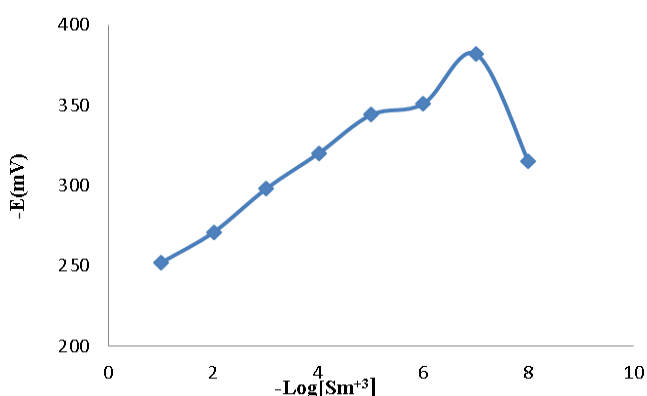


**Figure 3. Optimal Response Curve of the Samarium-Selective Electrode**

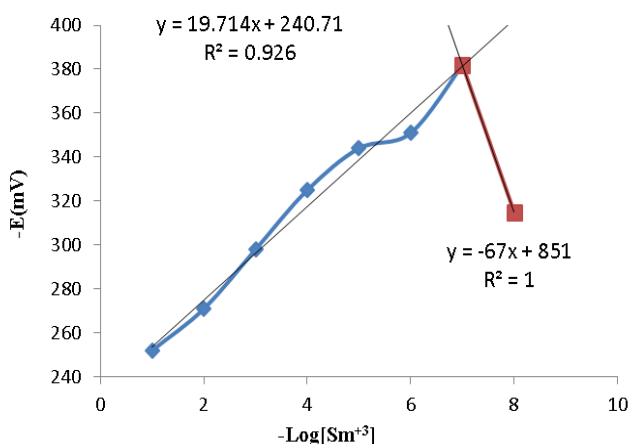


**Figure 4. Calculation of the Detection Limit of the Two Extrapolated Lines from the Calibration Curve of the Optimum Samarium-Selective Electrode**

The static response time of the optimized electrode for solutions of samarium nitrate with concentrations of  $1.0 \times 10^{-2}$  M,  $1.0 \times 10^{-3}$  M, and  $1.0 \times 10^{-4}$  M was investigated. Figure 5 shows that the response time of the electrode was in equilibrium in a short period of time, 10 seconds, and that it remained constant for 145 seconds. Evaluating the dynamic response of the optimal sensor was done by rapidly changing the concentration of samarium from diluted to concentrated concentrations in the range of  $1.0 \times 10^{-7}$  M to  $1.0 \times 10^{-1}$  M and then measuring time and potential; the results were obtained by changing the concentration of analyte such that the response time of the electrode reached equilibrium after only a short time. Figure 6 shows that the reason for this result can be related to the rapid exchange of complexation-decomplexation of the samarium ions with the ion selectivity of the membrane-solution boundary.

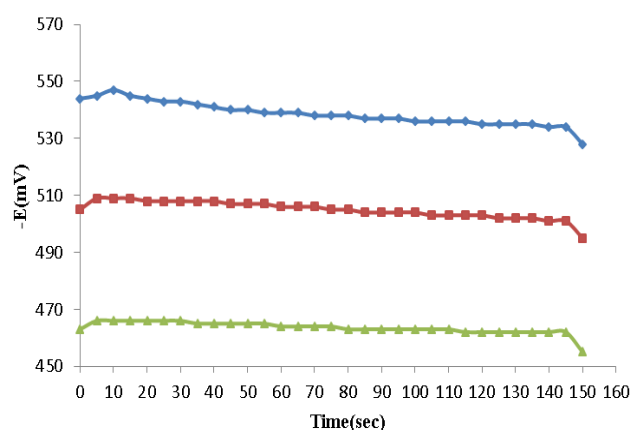


**Figure 5. Static Response Time of the Optimized Electrode ( $1.0 \times 10^{-3}$  M ■,  $1.0 \times 10^{-2}$  M ▲)**

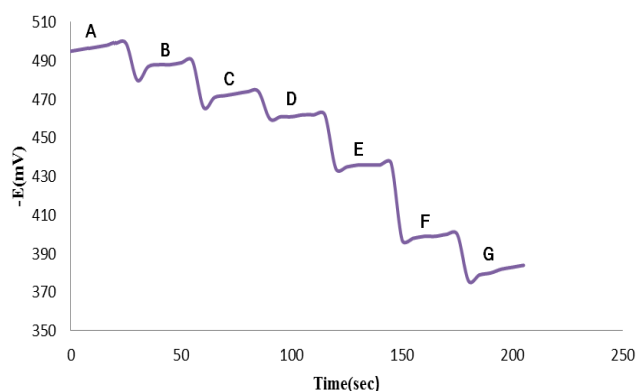


**Figure 6. Dynamic Response Time of the Optimized Electrode (G:  $1.0 \times 10^{-1}$  M, F:  $1.0 \times 10^{-2}$ , E:  $1.0 \times 10^{-3}$ , D:  $1.0 \times 10^{-4}$ , C:  $1.0 \times 10^{-5}$ , B:  $1.0 \times 10^{-6}$ , A:  $1.0 \times 10^{-7}$ )**

In order to verify the repeatability or reversibility of the optimal samarium-selective electrode's response, similar sequential measurements were made for solutions with concentrations of  $1.0 \times 10^{-2} \text{M}$  and  $1.0 \times 10^{-3} \text{M}$  from samarium nitrate. The results showed that for 10 consecutive measurements, solutions with these two concentrations were found to have an optimal samarium-selective electrode with no significant changes observed in electrode potential (see Figure 7). This indicates that the potentiometric response of the desired electrode is reversible [5]. According to the results given in Table 2, the proposed electrode had a good Nernst slope until 50 days, after which there was no change in its response.

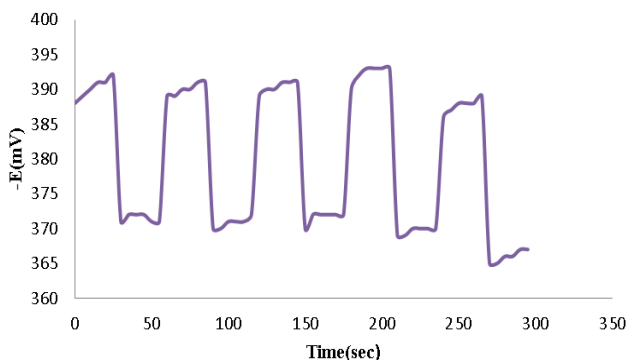


**Figure 7. Reversibility Curve of Optimum Samarium-Selective Electrode Response for Concentrations of  $1.0 \times 10^{-2} \text{M}$  and  $1.0 \times 10^{-3} \text{M}$  from Samarium Nitrate**

### Effect of pH

One of the most effective factors for determining electrode response is the pH of the solution. To investigate the effect of the pH of solution on electrode response, the potential of solutions with concentrations of  $1.0 \times 10^{-2} \text{M}$ ,  $1.0 \times 10^{-3} \text{M}$ , and  $1.0 \times 10^{-4} \text{M}$  from samarium nitrate in the pH range between 1 and 12 were measured. Based on the results obtained, the electrode's potential was constant in a pH range of 2 to 10, and the electrode's response in this region was independent on pH. As a result, this electrode can be

used to measure samarium in a wide range of actual samples without pH adjustment. At a pH below 2, due to the competition between  $\text{H}_3\text{O}^+$  and  $\text{Sm}^{3+}$  ions, electrode response was dependent on pH and the ion selectivity used can be partially protonated, which reduces the tendency of ion selectivity to form a complex with the samarium ions, resulting in inadequate function of the electrode. Figure 8 shows that, at pH values greater than 10, the potential becomes more negative, because of the formation of a samarium hydroxide deposit, and that the response of the electrode depends on pH.

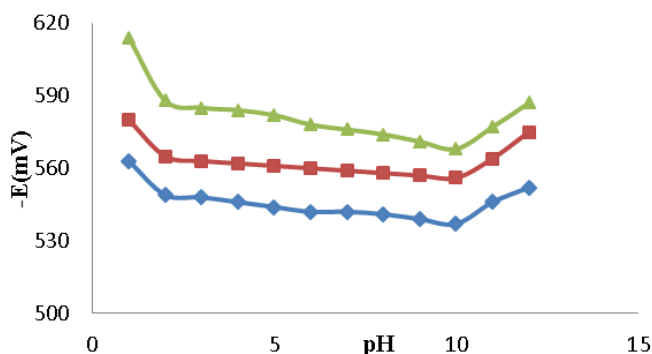


**Figure 8. Potential Changes in Terms of pH of Solution for an Optimum Samarium-Selective Electrode ( $1.0 \times 10^{-2} \text{M}$  ◆,  $1.0 \times 10^{-3} \text{M}$  ■,  $1.0 \times 10^{-4} \text{M}$  ▲)**

### Selectivity of the Optimal Electrode and a Study of its Disturbances

In this study, the separate solution method (SSM) was used to investigate the effect of intrusive ions. In this method, the potential of a solute containing the ion-selective electrode and a reference electrode was measured for two separate solutions with identical concentrations (0.01M)—one containing the original ion (*i*) without an interfering ion, and the other containing an interferent ion (*j*) without the presence of the original ion. Table 3 provides the calculated selectivity coefficients of the samarium-selective electrode.

**Table 2. Slope of the Optimum Samarium-Selective Electrode over Time**

Time	1 day	7 days	14 days	21 days	28 days	35 days	43 days	50 days	57 days	60 days	71 days
Slope (mV/decade)	19.7	19.8	20.0	20.5	19.5	21.0	20.3	20.6	21.7	22.1	22.6

According to the results, cations do not disturb the measurement of the samarium, and it can be said that the proposed sensor has a high sensitivity to the  $\text{Sm}^{3+}$  cation among other cations.

**Table 3. Selectivity Coefficients of the Samarium-Selective Electrode**

$M^{n+}$	$K_{ij}$
$\text{Ce}^{3+}$	$<10^{-6}$
$\text{Ag}^+$	$<10^{-6}$
$\text{Sr}^{2+}$	$<10^{-6}$
$\text{K}^+$	$<10^{-6}$
$\text{Cu}^{2+}$	$<10^{-6}$
$\text{Cr}^{3+}$	$<10^{-6}$
$\text{Pb}^{2+}$	$<10^{-6}$
$\text{Co}^{2+}$	$1.5 \times 10^{-5}$
$\text{Fe}^{3+}$	$<10^{-6}$
$\text{Cd}^{2+}$	$<10^{-6}$
$\text{Ni}^{2+}$	$<10^{-6}$

In order to evaluate the efficiency of the electrode under laboratory conditions, a series of potentiometric titrations with the electrode was performed. The results showed that high deflection near the equivalence point indicates the efficiency of the electrode in the potentiometric titration measurements (see Figures 9 and 10).

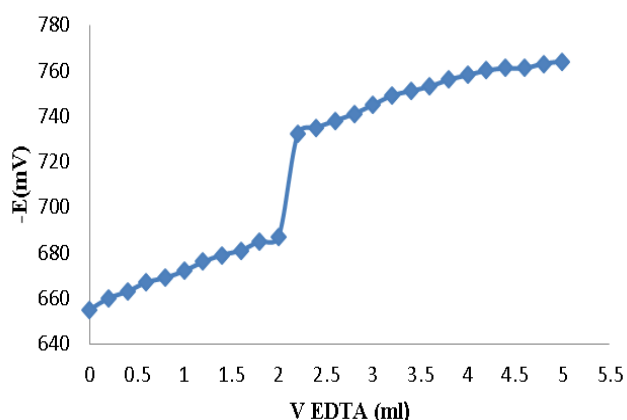


**Figure 9. Potentiometric Titration Curve of the Samarium Nitrate Solution ( $10^{-3}\text{M}$ ) with the EDTA Solution ( $10^{-2}\text{M}$ )**

This samarium-selective electrode was used to determine the amount of  $\text{Sm}^{3+}$  cation in samples of twice-distilled wa-

ter, which was added to 4 ppm and 8 ppm ion samarium. The results showed that this sensor was able to measure very low concentrations of samarium with highly accuracy and can replace expensive methods such as atomic absorption spectrometers for measuring these cations in solutions. In evaluation of the efficiency of the sensor, it was used to measure the  $\text{Sm}^{3+}$  ion in water samples from the Ahvaz, Karun, and Dez rivers, as well as the water of the Persian Gulf. First, a specific concentration of samarium cation was injected into these specimens and then the amount of samarium was determined using the method of standard addition. The results shown in Table 4 indicate that the proposed sensor was able to measure the samarium in real samples with very high efficiency. Table 5 shows the comparison between behaviors of the electrode in this project with some samarium-selective electrodes previously reported. As can be seen, the designed electrode had very good performance compared to other electrodes.

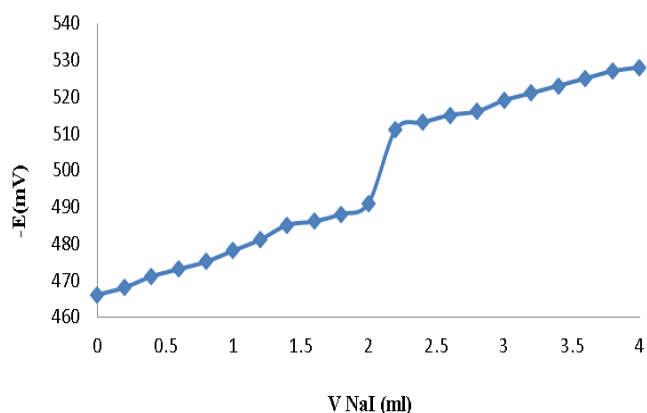


**Figure 10. Potentiometric Titration Curve of the Samarium Nitrate Solution ( $10^{-3}\text{M}$ ) with the NaI Solution ( $10^{-2}\text{M}$ )**

**Table 4. Samarium Measurements in Real Water Samples Using the Optimal Samarium-Selective Electrode**

Samples	Injected Concentration of $\text{Sm}^{3+}$	Measured Concentration of $\text{Sm}^{3+}$	Efficiency (%)
Water of Ahvaz	$3.0 \times 10^{-4}\text{M}$	$2.9 \times 10^{-4}\text{M}$	96.6
Water of Karun	$3.0 \times 10^{-4}\text{M}$	$2.7 \times 10^{-4}\text{M}$	90.0
Water of Dez	$3.0 \times 10^{-4}\text{M}$	$2.8 \times 10^{-4}\text{M}$	93.3
Waters of the Persian Gulf	$3.0 \times 10^{-4}\text{M}$	$2.8 \times 10^{-4}\text{M}$	93.3

## Conclusions

In this study, the optimization of membrane components and an analysis of the effects of how different softeners and lipophilic ion additives can play a significant role in the sensitivity and selectivity of an electrode were evaluated. The electrode was a samarium-selective electrode with the domain of linear concentration of between  $1.0 \times 10^{-7} \text{M}$  and  $1.0 \times 10^{-1} \text{M}$ , a Nernst slope of  $19.7 \pm 0.1 \text{ mV/decade}$ , and a detection limit of  $9.3 \times 10^{-8} \text{M}$ . The membrane of this electrode contained 63% NB, 30% PVC, 5% ion-selective Kryptofix 22DD, and 2% NaTPB. The effect of time on the electrode's response showed that the response was fast, about 10 seconds, and remained constant for 145 seconds without its potential changing. The electrode also showed excellent reversibility for two consecutive concentrations of samarium nitrate solutions. In addition, the lifetime of the electrode was determined using a working electrode for 50 days during the project.

The study of the effect of pH on the coating of the electrode showed that the potential in the pH range of 2-10 was constant and that the electrode was able to measure samarium in solutions within this pH range. Investigating the effect of intrusive ions with this electrode, it was concluded that the proposed electrode had very high selectivity compared to the cation of  $\text{Sm}^{3+}$  in solution and in the presence of other ions. Also, the presence of these ions in aqueous samples with samarium did not disturb the measurement. This electrode was used as a detector electrode for a potentiometric titration of a solution of samarium with solutions of EDTA and NaI. The deflection of the curves near the equivalence point indicated the efficiency of the electrode in the parametric measurements. Also, this optimal electrode was used to measure solutions of samarium with concentrations of 4 ppm and 8 ppm. The results showed that this electrode could be a suitable replacement for expensive methods, such

as atomic absorption spectrometers, in order to measure low concentrations of samarium in solutions. Finally, the electrode was used to measure the concentration of samarium in real water samples from the Ahvaz, Dez, and Karun rivers as well as the water of Persian Gulf. Again, the electrode was found to have a very high efficiency for measuring samarium in real samples. The results showed that Kryptofix 22DD is an ideal device for designing and manufacturing samarium-selective electrodes. The prepared electrode had high sensitivity when used to look for samarium cations, high linear concentration ranges, low detection limits, rapid response times, good reversibility, a wide range of pH, and high selectivity.

## References

- [1] Lai, M. T., & Shih J. S. (1986). Mercury(II) and silver(I) ion-selective electrodes based on dithia crown ethers. *Analyst*, *111*, 891-895.
- [2] Kamata, S., Yamasaki, K., Higo, M., Bhale, A., & Fukunaga Y. (1988). Copper(II)-selective electrodes based on macrocyclic polythiaethers. *Analyst*, *113*, 45-47.
- [3] Mohammad zadeh Kakhki, R., & Rounaghi, G. H. (2011). Selective uranyl cation detection by polymeric ion-selective electrode based on benzo-15-crown-5. *Material Science and Engineering C*, *16*, 1637-1642.
- [4] Motlagh, M. G., Taher, M. A., & Ahmadi, A. (2010). PVC membrane and coated graphite potentiometric sensors based on 1-phenyl-3-pyridin-2-yl-thiourea for selective determination of iron(III). *Electrochimica Acta*, *55*, 6724-6730.
- [5] Izatt, R. M. (1974). The Synthesis and Ion Bindings of Synthetic Multidentate Macrocyclic Compounds. *Chemical Reviews*, *74*, 351-385.

**Table 5. Comparison of the Behavioral Characteristics of the Optimized Electrode Prepared in This Project with Other Samarium-Selective Electrodes**

Reference	Ion-selective	Detection Limit (M)	Slope (mV/decade)	pH Range	Linear Concentration Range (M)	Lifetime	Response Time (Sec)
[13]	Glipizide	$8.0 \times 10^{-11}$	-	-	$-1.0 \times 10^{-3}$ $1.0 \times 10^{-10}$	70 days	< 15
[7]	Tin (IV) borate phosphate	-	-	-10.0 4.0	$-1.0 \times 10^{-1}$ $1.0 \times 10^{-5}$	180 days	< 10
[6]	2-thioxazolidin methylphenol	$8.0 \times 10^{-10}$	18.2	-8.0 3.0	$-1.0 \times 10^{-4}$ $1.0 \times 10^{-9}$	-	20 - 25
This current project	Kryptofix 22DD	$9.3 \times 10^{-8}$	19.7	-10.0 2.0	$-1.0 \times 10^{-1}$ $1.0 \times 10^{-7}$	50 days	10

- 
- [6] Ganjali, M. R., Memari, Z., Faridbod, F., & Norouzi, P. (2008). Samarium Microsensor: An Asymmetric Potentiometric Membrane Sensor. *International Journal of Electrochemical Science*, 3, 1169-1179.
- [7] Mittal, S. K., Sharma, H. K., & Kumar, A. S. K. (2004). Samarium (III) Selective Membrane Sensor Based on Tin (IV) Boratophosphate. *Sensors*, 4, 125-135.
- [8] Shamsipur, M., Hosseini, M., Alizadeh, K., Talebpour, Z., Mousavi, M. F., Ganjali, M. R., et al. (2003). PVC membrane and coated graphite potentiometric sensors based on Et4ttdit for selective determination of samarium (III). *Analytical Chemistry*, 75, 5680-5686.
- [9] Arada Perez, M. A., Perez Marin, L., Quintana, J. C., & Yazdani-Pedram, M. (2003). Influence of different plasticizers on the response of chemical sensors based on polymeric membranes for nitrate ion determination. *Sensors and Actuators B*, 89, 262-268.
- [10] Ammann, D., Pretsch, E., & Simon, W. (1985). Lipophilic salts as membrane additives and their influence on the properties of macro- and micro-electrodes based on neutral carriers. *Analytica Chimica Acta*, 171, 129-119
- [11] Schaller, U., Bakker, E., Spichiger, U. E., & Pretsch, E. (1994). Ionic additives for ion-selective electrodes based on electrically charged carriers. *Analytical Chemistry*, 66, 391-398.
- [12] Guilbault, G. G. (1981). Recommendations for publishing manuscripts on ion-selective electrodes. *Pure and Applied Chemistry*, 53, 1907-1912.
- [13] Ganjali, M. R., Pourjavid, M. R., Rezapour, M., & Haghgoo, S. (2004). PPT Level Detection of Samarium (III) with a coated Graphite sensor based on an antibiotic. *Analytical Science*, 20, 1007-1011.

## Biographies

**NESHAT MAJD** Islamic Azad University, Iran. Mr. Majd may be reached at [majd.neshat7@gmail.com](mailto:majd.neshat7@gmail.com)

**AREZOO GHAEMI** is a professor at the Ferdowsi University of Mashhad, Iran.



# INSTRUCTIONS FOR AUTHORS: MANUSCRIPT SUBMISSION REQUIREMENTS


The INTERNATIONAL JOURNAL OF MODERN ENGINEERING is an online/print publication. Articles appearing in IJME are centered around engineering-related research. All submissions to this journal, including manuscripts, peer-reviews of submitted documents, requests for editing changes, as well as notification of acceptance or rejection, will be handled electronically.

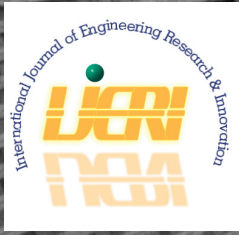
All manuscript submissions must be prepared in Microsoft Word (.doc or .docx) and contain all figures, images and/or pictures embedded where you want them and appropriately captioned. It is highly recommended that you print, in color, all images in your manuscript in order to determine their quality; the journal editors will be doing the same during the editorial review of your manuscript. If your manuscript is accepted for publication, you will receive instructions regarding all required revisions and the submission of higher-quality images. If you are able to provide such images, it's possible that you will be asked to remove them from the manuscript.

Tables must be created directly in Word, not imported as pictures, and be enclosed on all sides. If you have graphs or charts, they should also be created directly in Word, if possible. If that is not possible, the editor will discuss further options with you. Please be conscientious of the quality of your images and remember that all online and print copies of issues of IJME are in color.

The editorial staff of the International Journal of Modern Engineering reserves the right to format and edit any submitted document in order to meet publication standards of the journal. Included here is a summary of the formatting instructions. You should, however, review the "[sample Word document](#)" included on our website ([http://ijme.us/formatting\\_guidelines](http://ijme.us/formatting_guidelines)) for a detailed analysis of how to correctly format your manuscript.

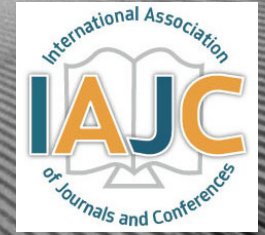
The references included in the References section of your manuscript must follow APA-formatting guidelines. In order to help you, the sample Word document also includes numerous examples of how to format a variety of sources. If you have a reference source for which you are not able to find the correct APA format, contact me for help anytime ([philipw@bgsu.edu](mailto:philipw@bgsu.edu)). Keep in mind that an incorrectly formatted manuscript will be returned to you, a delay that may cause it to be moved to a subsequent issue of the journal.

1. Word document page setup: Top = 1", Bottom = 1", Left = 1.25", Right = 1.25". This is the default setting for Microsoft Word.
2. Page breaks, tabs, and indents: Do not use page breaks or tabs. Do not use spaces for paragraph indents; use the scroll markers, as shown here. 
3. Paper title: Centered at the top of the first page with a 22-point Times New Roman (Bold), Small-Caps font.
4. Body fonts: Use 10-point Times New Roman (TNR) for body text throughout (1/8" paragraph indentation); 9-point TNR for author names/affiliations under the paper title; 16-point TNR for major section titles; 14-point TNR for minor section titles; 9-point TNR BOLD for caption titles; other font sizes may be noted in the sample Word document.
5. Images: All images should be included in the body of the document. It's ok for images or tables to be centered on the page, and not confined to the 2-column format, if necessary. Irrespective of how Word moves any given image/table, be certain that all captions are located in the document where the images/tables should ultimately be placed. If you are required to submit additional high-quality images, they must be saved/sent as individual files (one image per file) and labeled using the following format, where the first portion of the title is your manuscript number:  
**M15-F-10 Figure 4**
6. In-text referencing: List and number each reference when referring to them in the body of the document (e.g., [1]). In-text references must be in numerical order and follow entries in the References section. Again, see the sample Word document on our website for specifics. Please do not use the End-Page Reference utility in Microsoft Word.
7. Tables and figures: Captions for tables must be above the table, while captions for figures are below; all captions are left-justified unless the table or figure is centered on the page, in which case the caption should also be centered.
8. Page limit: Manuscripts should not be more than 15 pages (single-spaced, 2-column format).
9. Page numbering: Do not use page numbers.



[www.ijeri.org](http://www.ijeri.org)

Print ISSN: 2152-4157  
Online ISSN: 2152-4165



[www.iajc.org](http://www.iajc.org)

## INTERNATIONAL JOURNAL OF ENGINEERING RESEARCH AND INNOVATION

### **ABOUT IJERI:**

- IJERI is the second official journal of the International Association of Journals and Conferences (IAJC).
- IJERI is a high-quality, independent journal steered by a distinguished board of directors and supported by an international review board representing many well-known universities, colleges, and corporations in the U.S. and abroad.
- IJERI has an impact factor of **1.58**, placing it among an elite group of most-cited engineering journals worldwide.

### **OTHER IAJC JOURNALS:**

- The International Journal of Modern Engineering (IJME)  
For more information visit [www.ijme.us](http://www.ijme.us)
- The Technology Interface International Journal (TIIJ)  
For more information visit [www.tiij.org](http://www.tiij.org)

### **IJERI SUBMISSIONS:**

- Manuscripts should be sent electronically to the manuscript editor, Dr. Philip Weinsier, at [philipw@bgsu.edu](mailto:philipw@bgsu.edu).

For submission guidelines visit  
[www.ijeri.org/submissions](http://www.ijeri.org/submissions)

### **TO JOIN THE REVIEW BOARD:**

- Contact the chair of the International Review Board, Dr. Philip Weinsier, at [philipw@bgsu.edu](mailto:philipw@bgsu.edu).

For more information visit  
[www.ijeri.org/editorial](http://www.ijeri.org/editorial)

### **INDEXING ORGANIZATIONS:**

- IJERI is currently indexed by 16 agencies. For a complete listing, please visit us at [www.ijeri.org](http://www.ijeri.org).

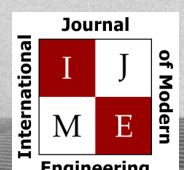
### **Contact us:**

**Mark Rajai, Ph.D.**

Editor-in-Chief  
California State University-Northridge  
College of Engineering and Computer Science  
Room: JD 4510  
Northridge, CA 91330  
Office: (818) 677-5003  
Email: [mrajai@csun.edu](mailto:mrajai@csun.edu)



[www.tiij.org](http://www.tiij.org)



[www.ijme.us](http://www.ijme.us)

# THE LEADING JOURNAL OF ENGINEERING, APPLIED SCIENCE AND TECHNOLOGY

**The latest impact factor (IF) calculation (Google Scholar method) for IJME of 3.0 moves it even higher in its march towards the top 10 engineering journals.**

**IJME IS THE OFFICAL AND FLAGSHIP JOURNAL OF THE  
INTERNATIONAL ASSOCIATION OF JOURNALS AND CONFERENCE (IAJC)**

[www.iajc.org](http://www.iajc.org)



The International Journal of Modern Engineering (IJME) is a highly-selective, peer-reviewed journal covering topics that appeal to a broad readership of various branches of engineering and related technologies. IJME is steered by the IAJC distinguished board of directors and is supported by an international review board consisting of prominent individuals representing many well-known universities, colleges, and corporations in the United States and abroad.

## **IJME Contact Information**

**General questions or inquiries about sponsorship of the journal should be directed to:**

**Mark Rajai, Ph.D.**

**Editor-in-Chief**

**Office: (818) 677-5003**

**Email: [editor@ijme.us](mailto:editor@ijme.us)**

**Department of Manufacturing Systems Engineering & Management**

**California State University-Northridge**

**1811 Nordhoff St.**

**Northridge, CA 91330**